GLOBAL OCEANIC RAINFALL ESTIMATION FROM AMSR-E DATA BASED ON A RADIATIVE TRANSFER MODEL

A Dissertation

by

KYOUNG-WOOK JIN

Submitted to the Office of Graduate Studies of
Texas A&M University
in partial fulfillment of the requirements for the degree of

DOCTOR OF PHILOSOPHY

December 2005

Major Subject: Atmospheric Sciences

GLOBAL OCEANIC RAINFALL ESTIMATION FROM AMSR-E DATA BASED ON A RADIATIVE TRANSFER MODEL

A Dissertation

by

KYOUNG-WOOK JIN

Submitted to the Office of Graduate Studies of
Texas A&M University
in partial fulfillment of the requirements for the degree of

DOCTOR OF PHILOSOPHY

Approved by:

Chair of Committee,	Thomas T. Wilheit
Committee Members,	Kenneth P. Bowman
	Ping Yang
	Robert Hetland
Head of Department,	Richard Orville

December 2005

Major Subject: Atmospheric Sciences

ABSTRACT

Global Oceanic Rainfall Estimation from AMSR-E Data

Based on a Radiative Transfer Model. (December 2005)

Kyoung-Wook Jin, B.S., Seoul National University;

M.S., Texas A&M University

Chair of Advisory Committee: Dr. Thomas T. Wilheit

An improved physically-based rainfall algorithm was developed using AMSR-E data based on a radiative transfer model. In addition, error models were designed and embedded in the algorithm to assess retrieval errors quantitatively and to reduce net retrieval uncertainties.

The algorithm uses six channels (dual polarizations at 36.5, 18.7 and 10.65GHz) and retrieves rain rates on a pixel-by-pixel basis. Monthly rain totals are estimated by summing average rain rates computed by merging six rain rates based on proper weights that are estimated from error models. Error models were constructed based upon the principal error sources of rainfall retrieval such as beam filling error, drop size distribution uncertainty and instrument calibration errors.

Several improved schemes that minimize uncertainties of the rainfall retrieval were developed in this study. In particular, improved offset correction that corrects the biases near zero rain plays a very important role for reducing uncertainties which are mainly driven by calibration uncertainty including the modeling errors. AMSR-E's larger calibration uncertainty was substantially absorbed by this offset correction as well as by the weighted average scheme to combine all six channels optimally. As a framework for

inter-comparison with the experimental algorithm, the current operational algorithm (NASA, level 3 algorithm) was also updated with respect to AMSR-E data.

The experimental algorithm was compared with the operational algorithm for both AMSR-E and TMI data and rainfall retrieval uncertainties were analyzed using error models. When the experimental algorithm was used, many limitations of the operational algorithm were overcome and uncertainties of rainfall retrieval were considerably eliminated.

ACKNOWLEDGEMENTS

Special thanks should first be given to my advisor, Dr. Thomas T. Wilheit. He guided me in the right direction and helped me to overcome many barriers throughout my research. He was also a good mentor and helped me not only with academic issues but also with personal matters during my graduate study here in the United States.

I would also like to thank my other committee members, Dr. Kenneth Bowman, Dr. Ping Yang, and Dr. Robert Hetland, for their helpful comments during this effort. Special thanks also go to Dr. Gerald North for his advice.

I would like to express my appreciation to the members of the microwave remote sensing group, who have helped me in so many ways throughout this research. Special thank goes to Kai Feng for his help with computer programming and very useful information about the Linux system and to Richard Weitz for his help with handling satellite data. I would also like to thank Sung-Wook Hong for his comments and discussion about my study.

Certainly I would like to thank my parents for their support from my home country Korea. Without their love, this work would not have been possible.
My gratitude is warmest to my wife, Yun-hi, who always encouraged me and followed me without complaint. Her deepest love has been instrumental in my study here in America. Special thanks also should be given to my adorable kids Jua and Juwon.

I also acknowledge financial support from the NASA AQUA program.

TABLE OF CONTENTS

Page

LIST OF FIGURES

FIGURE Page

FIGURE Page

FIGURE Page

FIGURE Page

FIGURE Page

FIGURE Page

LIST OF TABLES

CHAPTER I

INTRODUCTION

For the study of the global water cycle and its budget, rainfall estimation is very important. In addition, since the rainfall amount in the atmosphere is directly related to latent heat release, quantitative measurement of the rainfall is vital for computing atmospheric dynamics.

Direct measurements of precipitation over the oceans that cover almost three quarters of the earth are, however, extremely limited. As a result, remote sensing techniques which use space-borne measurements have been developed. In particular, an emission-based passive microwave technique that uses the direct relationship between observed radiances and the rainfall amount of the atmosphere has provided very promising results.

This technique began with the Nimbus-5 satellite carrying the ESMR (Electronically Scanned Microwave Radiometer)-5 which was launched in Dec 1972. A model (Wilheit et al., 1977) that simulates microwave radiative transfer of a raining atmosphere was designed to estimate the oceanic rainfall. As follow-on missions, ESMR-6 and SMMR (Scanning Multi-channel Microwave Radiometer) were carried on the Nimbus-6 and Numbus-7 satellites (launched in 1975 and 1978 respectively), were also used for oceanic rainfall retrieval study. Further, Wilheit et al. (1991) developed a physically-based rainfall algorithm using the SSM/I (Special Sensor Microwave Imager) data from DMSP (The Defense Meteorological Satellite Program). A refined version of this algorithm (NASA, Level 3 operational rainfall algorithm) has been improved for

---

This dissertation follows the style and format of the *Journal of Applied Meteorology*.

TMI (TRMM Microwave Imager) for TRMM (Tropical Rainfall Measuring Mission) and became a launch version for AMSR-E for the AQUA mission (Wilheit et al., 2003).

However, to estimate rainfall more accurately, the error sources of the rainfall retrieval should be more effectively handled in the algorithm. The current operational rainfall algorithm utilizes only the two channels (19 and 21GHz) that have limited dynamic ranges of rainfall retrieval, uses a mixed log-normal function of rain rate. This statistical approximation leads to an intrinsic discrepancy with observations. Also, the algorithm does not account for the spatial and temporal variability of freezing levels properly because it assumes one representative freezing level for entire month. In addition, AMSR-E data show larger calibration uncertainties compared to TMI and SSM/I data. Because these calibration uncertainties related with the warm calibration target were not fully accounted for in the operational algorithm, the calibration problem has become an important issue for AMSR-E data.

To overcome these problems, we developed an improved rainfall algorithm (so called experimental algorithm) that is more robust for handling many of uncertainties of the rainfall retrieval. This experimental algorithm, also based on a RTM, was originally designed for TMI (Huang, 2001) but it was not mature enough. Some adjustments were implemented and additional enhanced schemes were developed during this study. The main differences between the experimental algorithm and the operational algorithm are the use of three different frequencies (37, 19 and 10GHz) and a pixel-by-pixel freezing level retrieval scheme. A total of six rain rates are retrieved using dual polarized (vertical and horizontal) channels of each of the three frequencies and monthly rain totals are computed based on weighted averages of the rain rates with offset corrections.

The results were compared with those of the operational algorithm for both TMI and AMSR-E data and the improvements of the experimental algorithm, especially the quantitative error estimates were examined by constructing error models.

CHAPTER II

BACKGROUND

2.1 Radiative Transfer Equation

The intensity of radiation $B_\lambda(T)$ from a blackbody with a wavelength λ is described by the Planck function.

$$B_\lambda(T) = \frac{2hc^2}{\lambda^5} \cdot \frac{1}{\exp(\frac{hc}{\lambda kT}) - 1}$$

where *h* is the Planck constant, *k* is the Boltzman constant and *c* is the velocity of light. However, in the microwave regime ($\frac{hc}{\lambda kT} << 1$), the Planck function is simplified and leads to a linear approximation between the radiation and the blackbody temperature.

$$B_\lambda(T) \approx \frac{2hc^2}{\lambda^5} \cdot \frac{\lambda kT}{hc} = \frac{2ck}{\lambda^4} \cdot T$$

This equivalent blackbody temperature *T* is called a brightness temperature (T_B). The change of the brightness temperature over an infinitesimal distance ds in a direction by elevation angle θ and azimuth angle ϕ can be computed as follows (Chandrashekar,1960).

$$\frac{dT_B(\theta,\phi)}{ds} = L + G$$

where

$$L \equiv -(\gamma_{abs} + \gamma_{sca})T_B(\theta,\phi)$$

$$G \equiv \gamma_{abs}T(s) + \gamma_{sca}\oint P(\theta,\phi,\theta',\phi')T_B(\theta',\phi')d\Omega'$$

$T_B(\theta,\phi)$ is the brightness temperature in a given direction by polar angle (θ,ϕ), $T(s)$ is thermodynamic temperature of the medium, γ_{abs} is the absorption coefficient, γ_{sca} is the scattering coefficient, and $P(\theta,\phi,\theta',\phi')$ is the phase function for the probability of scattering from a direction specified by (θ',ϕ') to a direction (θ,ϕ). In the equation, the term *L* describes the microwave radiances lost by absorption and scattering during the propagation and the term *G* stands for the microwave radiance gained from the emission of the medium plus the contribution of scattered microwave radiances from the other directions into the propagating direction.

If only the absorption term is considered, the derivative form of the radiative transfer equation can be integrated as follows:

$$T_B(\lambda,\theta,p) = U1 + U2$$

where

$$U1 = \int_0^{\infty} \gamma_{abs}(z)T(z)e^{-\tau_\lambda(z,\infty)\mu}\mu dz + (1 - r\ (\lambda,\theta,p))T_s e^{-\tau_\lambda(0,\infty)\mu}$$

$$U2 = r\ (\lambda,\theta,p)e^{-\tau_\lambda(0,\infty)\mu} \cdot \left[T_{\cos mic} e^{-\tau_\lambda(0,\infty)\mu} + \int_0^{\infty} \gamma_{abs}(z)T(z)e^{-\tau_\lambda(0,z)\mu}\mu dz \right]$$

where $\tau_\lambda(z_1,z_2) = \int_{z_1}^{z_2} \gamma(z')\mu dz'$ is the optical thickness of the atmospheric layer between the height z_1 and z_2, μ is $1/\cos\theta$, $T_{\cos mic}$ is the 2.7 °K cosmic background brightness temperature, T_s is the surface temperature, $r\ (\lambda,\theta,p)$ is the surface emissivity at the wavelength λ, the incidence angle, θ, and the polarization, *p*, respectively. The term *U*1 represents upward radiation which consists of the emission by each incremental layer of the atmosphere and attenuated by the intervening layers plus the emission from the ocean

surface as attenuated by the atmosphere. The term $U2$ represents radiation reflected by the ocean surface which consists of the cosmic background as attenuated by the atmosphere through the whole path (from downward to upward) plus the downward emission attenuated by the portion of atmosphere between the emitting layer and the surface and attenuated during the upward propagation.

However, when the scattering term is included, the radiative transfer equation cannot be directly integrated because computing the radiation at any given direction requires knowledge of the radiance at all other angles. The Mie theory (1908), which provides the full spectrum of the scattering and absorption by dielectric spheres, is required to compute the extinction coefficients.

2.2 Rain Radiative Transfer Model

Based on the principles of microwave radiative transfer, a physical model was established for remote sensing of rainfall by Wilheit et al. (1977) and has been improved by Tesmer and Wilheit (1998) and Huang (2001). A brief description of the model is as follows.

To calculate brightness temperature, the atmosphere is divided into layers (a plane parallel atmosphere). Molecular oxygen, water vapor, non-raining clouds, and raining droplets are considered as major absorbing atmospheric constituents for microwave propagation. A simple two-phase description for the hydrometeors is applied in the model layers. An ice layer is assumed above the freezing level (FL) and a liquid layer below the FL. As a result, the hydrometeors above the FL are essentially transparent to most microwave frequencies (10, 19, 21 and 37GHz). However, as an approximate correction

to account for the increased absorption within the melting layer (bright-band), doubled extinction coefficients were employed for 250 meters below the FL based on Jin (2001).

The model consists of several fundamental atmospheric assumptions. It uses a modified Marshall-Palmer distribution (Marshall and Palmer, 1948) for the rain droplet distribution of the model atmosphere from the surface to the FL. As a standard thermodynamic assumption, it uses a 6.5°C/km lapse rate (However, it was updated in this study: Section 4.2c). The relative humidity is assumed as 80% at the surface and is increased linearly to 100% at the FL. To compute realistic scattering and absorption properties of the ensemble of rain droplets, the full Mie theory (Mie, 1908) was included. The extinction coefficient of a liquid water droplet was given by Gunn and East (1954). The sea surface emissivity which is computed by Fresnel equations was constructed based on the Lane and Saxton dielectric constant data (1952). The molecular oxygen absorption model was set up using Rosenkranz (1993). For the computation of water vapor absorption, the Staelin model (1966) was used and it was updated with the model of Rosenkranz (1998) with Thomas-Stahle's correction (2001) that accounts for the pressure broadening effect (it was also updated in this study: Section 4.2c).

2.3 Principles of Rainfall Retrieval

The extinction coefficient of raindrops (γ_{ext}) can be expressed as

$$\gamma_{ext} = \int N(r)\, \sigma_{ext}\, dr$$

where $N(r)$ is the number density of raindrops per unit volume between r and r+dr and σ_{ext} is the extinction cross section. The specific form of $N(r)$, Marshall-Palmer drop size distribution (Marshall and Palmer, 1948), is given by

$$N(r) = N_0 \exp(-\Lambda r)$$

where N_0 is 0.16 cm^{-4}, Λ is $81.56R^{-0.21}$, and R is the nominal rain rate in mm/h. In addition, the true rain rate R′ ignoring updrafts can be computed as

$$R'(r) = \frac{4\pi}{3}\int V(r)\cdot r^3 \cdot N(r)dr$$

where $V(r)$ is the speed of a rain drop with radius r (Beard,1977). From the above equations, it is straightforward that the computed rain rate is directly related to the extinction coefficient derived from the rain drop distribution via absorption and scattering. Based on the computed brightness temperatures as a function of rain rate from a radiative transfer model (RTM), the relationship of rain rate and brightness temperature, the R-T relationship (Fig. 2.1), is achieved. An analytical approximation to the R-T relationship can be expressed as

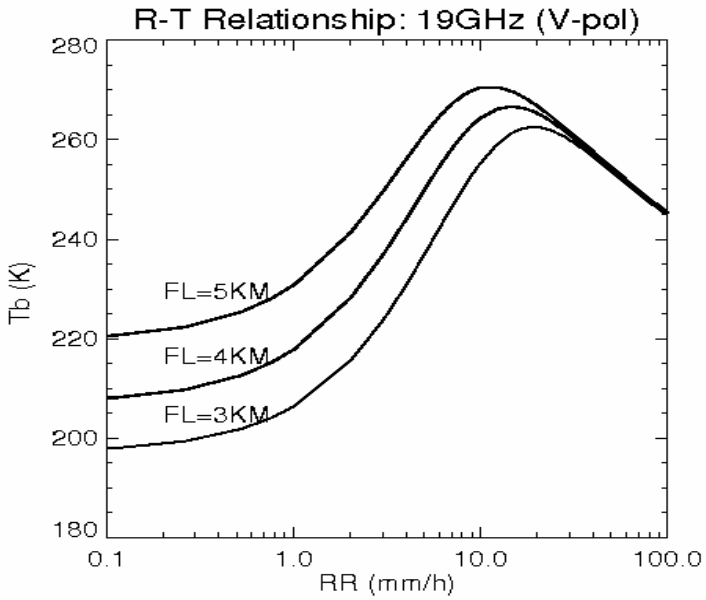

Figure 2.1 R-T relationship calculated by the radiative transfer model for the 19GHz vertical channel at an incidence angle of 52.8°(TMI incidence angle).

$$T(r) = T_0 + (T_1 - T_0)[1 - \exp(-\frac{r}{r_c})] - a\sqrt{r}$$

Where *T(r)* is the brightness temperature, r is the rain rate, r_c is the characteristic rain rate ($r_c = b/F^c$ where *F* is the freezing level) and T_0 is the background brightness temperature given by

$$T_0 = ta + tb \cdot F + tc \cdot F^2$$

The frequency dependent constants of the equations are listed in table 2.1 below. The four vertically polarized AMSR-E frequencies (10.65, 18.7, 23.8 and 36.5GHz vertical channels) were selected in this computation and the assumed incidence angle was 55.0° (of Aqua satellite).

Table 2.1 Constants in R-T relationship.

	10.65V	**18.7V**	**23.8V**	**36.5V**
ta	163.35	185.40	180.40	216.10
tb	1.15	-1.05	16.00	-3.50
tc	0.55	1.75	0.20	1.80
T1	**327**	**298**	**288**	**284**
a	5.58	6.31	6.53	9.89
b	47.60	20.83	28.25	8.87
c	0.69	1.05	1.86	1.50

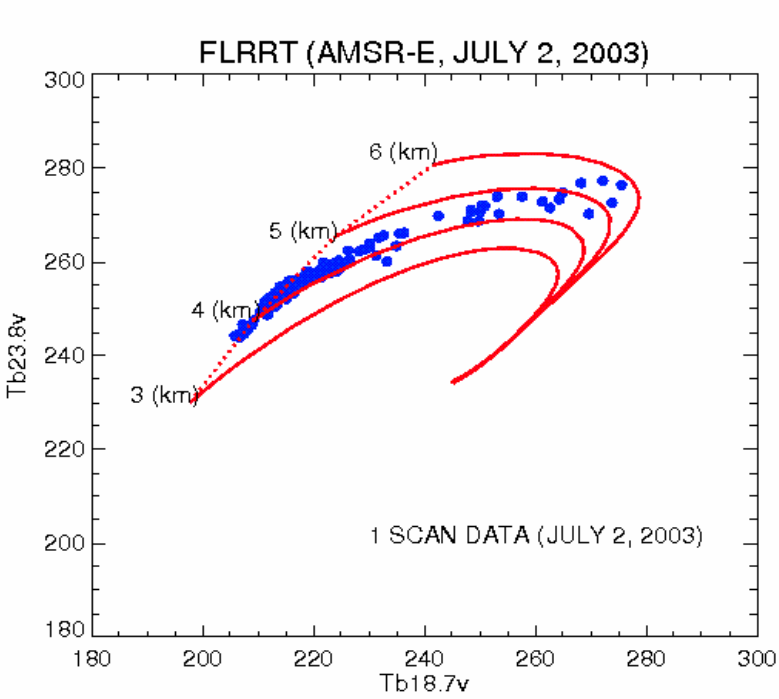

Figure 2.2 FLRRT chart for the 18.7 and 23.8GHz vertically polarized channels. The solid line indicates isolines of freezing level (3~6km). The dotted line indicates an isoline of zero rain rate. The solid circles denote the scatter-plot of observed 18.7 and 23.8GHz AMSR-E single scan data (July 2, 2003).

The R-T relationship is expressed as a function of freezing level because the brightness temperature depends on a given freezing level. Thus, when we compute rain rate using the R-T relationship, the freezing level must be determined first. To retrieve freezing levels physically, Wilheit et al. (1991) devised a FLRRT (freezing level and rain rate table) chart method using the combination of the 19 and 21GHz brightness temperatures. Because the freezing level is a proxy variable not only for the rain layer thickness but also for the amount of the water vapor content in the atmosphere, the freezing level table is computed from the integrated water vapor amount which is determined within the RTM.

Fig 2.2 shows an example of a FLRRT chart. Using the computed brightness temperatures of the 18.7 and 23.8GHz AMSR-E vertical channels, freezing level tables (solid lines) were generated. For illustration purpose, a single scan of the AMSR-E July 2, 2003 data was projected on the FLRRT. The scatter plot of the observed 18.7 and 23.8 GHz brightness temperatures shows that the estimated freezing levels are distributed mostly between 4km and 5km. Based on the retrieved freezing levels, rain rates are estimated using the R-T relationship. The rainfall retrieval algorithm, however, uses pre-generated freezing level and rain rate look-up tables for efficiency of computation.

2.4 Operational Monthly Rainfall Retrieval Algorithm

To retrieve rain rate over the oceans based upon the relationship between rain rate and brightness temperature, an algorithm was designed for SSM/I data by Wilheit et al. (1991) and has been improved throughout the lifetime of TRMM (Tropical Rainfall Measuring Mission). This algorithm uses a rain rate probability distribution function (p.d.f.) which is inferred from an observed brightness temperature histogram (Tb-Histogram) over 5° x 5° grid boxes for one month periods. The p.d.f. consists of two assumptions (mixed log-normal distribution): a normal distribution of brightness temperature for the non-raining part and a log-normal distribution of rain rates for the raining part. In particular, the normal distribution part absorbs the uncertainties near zero rain such as instrument calibration uncertainty. To reduce the impact of water vapor variability, a linear combination of the 19 and 21GHz channels was also devised.

The basic procedure of the monthly rainfall retrieval using the operational algorithm is as follows. One representative FL for entire month over a 5° x 5° box is

estimated from a combination of the 19 and 21GHz histograms. This value is used as a basis for retrieving the monthly rain rate for the box. Next, a computed Tb-Histogram of the 19-21GHz linear combination, 2xT19v-T21v, is adjusted iteratively to match the first three moments between the observed and the computed histogram. The probability of rain, the logarithmic mean rain rate and the standard deviation of the logarithm of rain rate, which are the parameters of the mixed log-normal distribution, are derived after satisfactory agreement is reached between the observed and computed histogram. During the iteration, the parameters of the non-raining part such as the mean and standard deviation of brightness temperatures of the non-raining peak are also adjusted. Lastly, those parameters are used for calculating the monthly rain total.

2.5 Experimental Monthly Rainfall Retrieval Algorithm

The operational algorithm described above has some limitations for accurate rainfall estimation. The use of a probability distribution function leads to potential discrepancies with the observed rainfall distribution. In particular, observed histograms of very rainy cases sometimes show large discrepancies from the log-normal distributions. Furthermore, the use of one representative FL for the entire month limits absorbing the variability of the freezing levels.

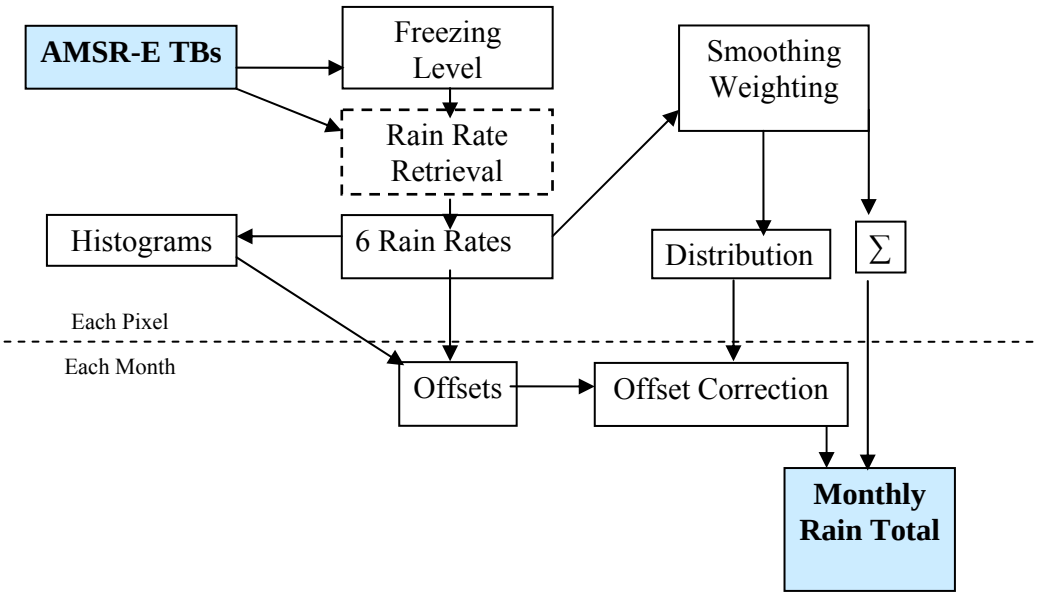

Figure 2.3 Flow chart of the AMSR-E Level-3 oceanic rainfall algorithm.

To overcome these limitations in the operational algorithm and to utilize additional frequencies (10 and 37GHz) which were not used in the operational algorithm, an algorithm (experimental algorithm) was developed in this study. This algorithm was originally designed by Huang (2001) and was tested on TMI data. It showed reasonable performance, however, was not yet fully mature. Based on this basic framework, we developed the algorithm with respect to AMSR-E data and designed several new schemes that are more robust for reducing uncertainties of rainfall retrieval. The detailed improvements are described in the chapter IV. The structure of the algorithm (Figure 2.3) can be summarized as follows.

First, the freezing levels are estimated from the 18.7(18) and 23.8(24) GHz channels on a pixel-by-pixel basis. Next, rain rates are retrieved from six channels (10, 18

and 37GHz with dual polarizations) using the retrieved freezing levels. These rain rates at their native resolution are merged into an average rain rate which is properly weighted based upon the contribution to uncertainties of the each channel. In principle, the highest weight is given by the channel which has the least rain rate uncertainty. However, to merge the three rain rates, the retrieved rain rates from their different native resolutions must be converted to the same resolution. The rain rates computed from the 37 and 19 GHz (higher resolution channels) are smoothed to that of the 10GHz resolution (lower resolution**)** to match same area. This is referred to the "smoothing" process.

Another important step in the algorithm is "offset correction". In general, a rain rate histogram over a specified area (e.g. 5 ° x 5° grid box) for a given month shows a small portion of negative rain rates and also the peaks of the histograms are not always found at the zero rain; that is, they show offsets. While this is physically nonsense, these biases can occur due to the data calibration uncertainties and modeling errors. However, because the most probable rain rate for a given month is zero even for a very rainy area, the offset correction (adjustment of the peak of rain rate histogram to zero-rain rate position) can be derived. As a result, many uncertainties near zero rain rate are effectively absorbed through this physical constraint. Since each channel has a different offset, the combined offsets which are properly weighted by the contribution of each channel's offset are required for the merged rain rates (weighted average rain rates). The level-3 product (monthly rain totals over 5 ° x 5° boxes) are computed by simply adding those weighted average rain rates which have offset correction along with the smoothing.

CHAPTER III

DATA

Two data sets were mainly used in this study; AMSR-E (Advanced Microwave Scanning Radiometer for EOS) data were primarily used for developing the experimental algorithm and TMI (TRMM Microwave Imager) data were used for comparison with AMSR-E data. The data sets were acquired from the following URLs.

1) TMI data (1B11)
http://lake.nascom.nasa.gov/data/dataset/TRMM/01_Data_Products/01_Orbital/index.html

2) AMSR-E data (L2A-beta)
http://nsidc.org/data/data_pool/index.html

3.1 AQUA Mission and AMSR-E

The AQUA satellite was launched in May 4, 2002 for multi-disciplinary studies such as the interrelated processes of the earth's atmosphere, ocean and land surface and their relationship to earth system. The AQUA mission is a part of the NASA-centered international Earth Observing System (EOS). AQUA was formerly named EOS PM, signifying its afternoon equatorial crossing time (1:30PM at ascending node). The Aqua satellite carries six instruments in a near-polar (98.2° inclination angle) low-Earth orbit (705km). It revolves about 15 times per day (98.8min period) with a sun-synchronous orbit.

AMSR-E, one of the Aqua instruments, was mainly intended to measure global precipitation and water vapor along with estimating other geophysical parameters. The AMSR-E is a conically scanning microwave radiometer which has six frequencies (6.925, 10.65, 18.7, 23.8, 36.5 and 89GHz). Each frequency has both horizontal and vertical polarizations. In this study, the lowest frequency (6GHz) and the highest frequency

(89GHz) were not used. The AMSR-E uses an offset parabolic reflector 1.6 meters in diameter to focus the radiation into an array of feed-horns. The instrument spins at 40 rpm (revolutions per minute) at 705km altitude and has a 1445km swath width.

3.2 Comparison of Characteristics between AMSR-E and TMI

While the satellites (AQUA and TRMM) differ from one another, the AMSR-E instrument is very similar to the TMI instrument. The characteristics of Aqua and TRMM satellites are summarized in Table 3.1 and the comparison between the AMSR-E and TMI instruments are listed in Table 3.2.

Table 3.1 Characteristics of AQUA and TRMM satellite.

	AQUA	TRMM
Orbit	Sun-Synchronous	Non Sun-Synchronous
Altitude	705km	350km (402.5km after reboost:8-24-01)
Inclination angle	98.2°	35°
Period	98.8min	91min (16orbits/day)
Local Sun Time (AQUA) Precession Rate (TRMM)	1:30pm (ascending node)	-0.52hr/day
Launch Date	May 4, 2002	Nov 27, 1997

Table 3.2 Comparison of AMSR-E and TMI instruments.

	AMSR-E	TMI
Observation Frequencies (GHz)	(6.925) (10.65) (18.7) (23.8) (36.5) (89.0)	(10.65) (19.35) (21.3) (37.0) (85.5)
IFOV (km x km)	(74x43) (51x30) (27x16) (31x18) (14x8) (6x4)	(60x36) (30x18) (27x17) (16x10) (7x4)
Incidence angle	55°	52.8° (53.4° after reboost:8-24-01)
Polarization	Vertical and Horizontal	Dual (except 21.3GHz : vertical only)
Swath width	1450km	759km (878km after reboost:8-24-01)
Spin Speed	40 rpm	31.5 rpm

CHAPTER IV

METHODS

4.1 Update of the Operational Algorithm

The operational algorithm, which was established for the SSM/I (Special Sensor Microwave Imager) and has been used for TMI data, was refined with respect to AMSR-E data as ground-work for comparison with the experimental algorithm. First, the change of frequencies and incidence angle were taken into account in the RTM. The AMSR-E frequencies are changed from 19.35 and 21.3GHz (TMI frequencies) to 18.7 and 23.8GHz respectively. The incidence angle of the AMSR-E was changed from 52.8° (of TMI) to 55°. Theses changes affect the brightness temperatures observed from the satellite because an increased incidence angle causes a longer path length for propagating microwaves and also the changes of incidence angle and frequencies lead to different sea surface reflectivity.

Second, we considered an appropriate adjustment for calibration uncertainty of the AMSR-E since AMSR-E data have larger calibration uncertainties associated with the warm calibration target than do TMI data. To assess the AMSR-E calibration uncertainties physically, the brightness temperature histograms of the two frequencies (19.35 and 21.35GHz for TMI, 18.7 and 23.8GHz for AMSR-E) plus linearly combined pseudo channels (2x19V-21V for TMI and 2x18V-24V for AMSR-E) were used. Figures 4.1a and 4.1b show the brightness temperature histograms using the unofficial AMSR-E Level 2 X1 Oct 2002 data and the official B (Beta) July 2003 data respectively.

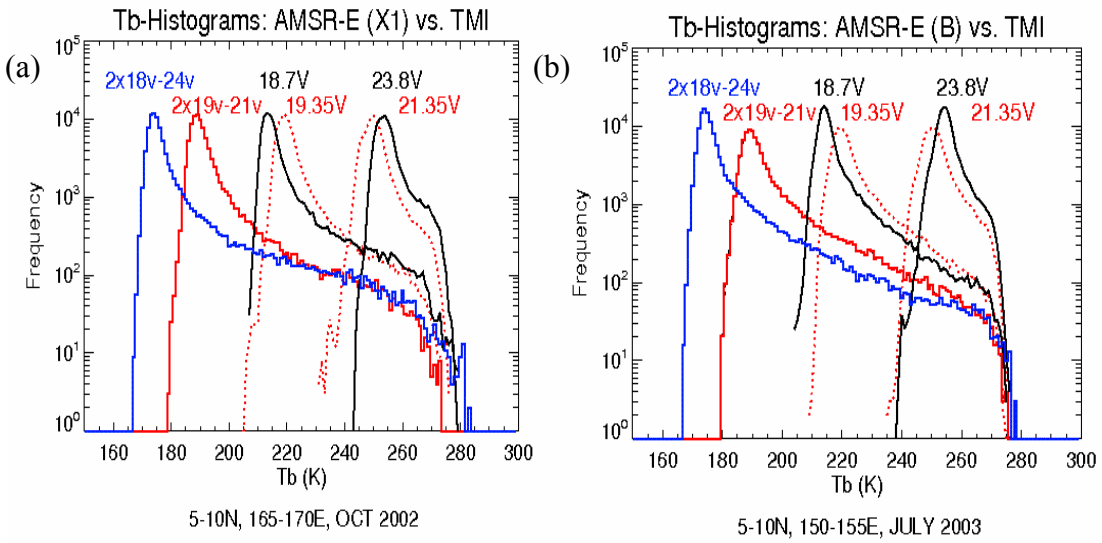

Figure 4.1 Brightness temperature histograms for 19 (18), 21(24) GHz and linearly combined two channels (Pseudo channel). Parenthesis stands for AMSR-E frequencies.
a) from X1 Oct 2002 data, b) from B July 2003 data.

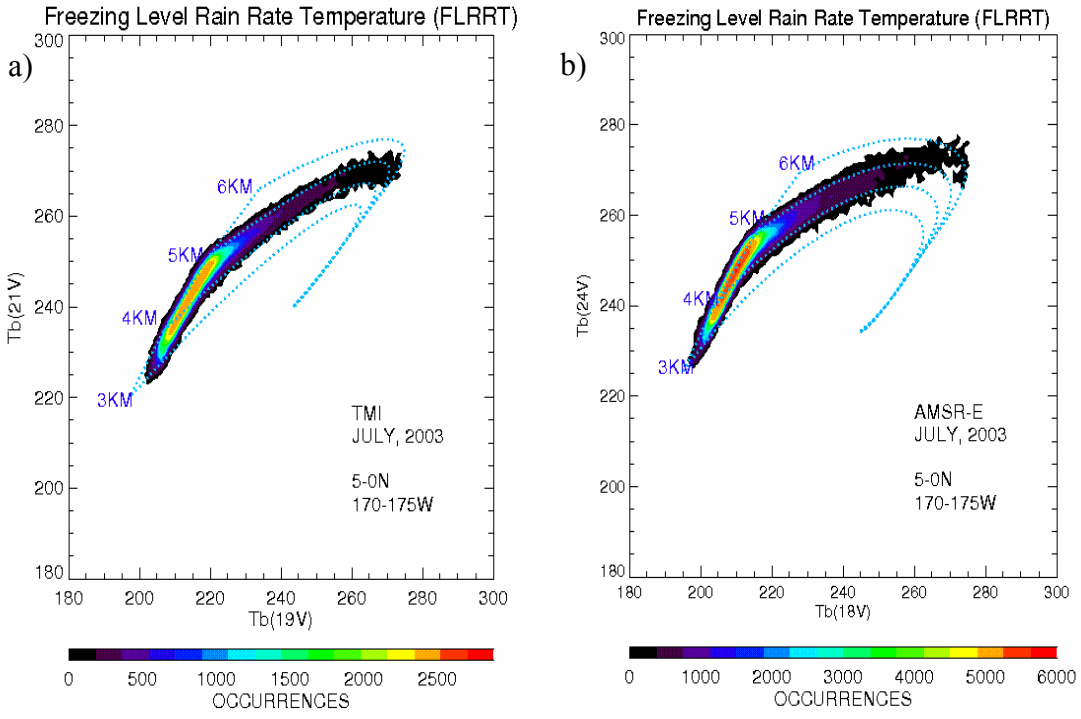

Figure 4.2 FLRRT chart using July 2003 data over 5-0N, 170-175W grid box. a) TMI FLRRT, b) AMSR-E FLRRT.

Except the pseudo channel of the AMSR-E, the brightness temperatures of all other channels are distributed in a reasonable range that is less than 280K. However, some very high brightness temperatures, over 280K, found in the AMSR-E pseudo channel, are considered physically unreasonable. Even though Fig. 4.2b, which was plotted using the official AMSR-E beta data, shows reduced warm calibration uncertainty, it still shows larger uncertainties than TMI data. Since both 18 and 24GHz brightness temperatures are distributed within the 280K, some cases of the very high brightness temperatures (over 280K) of the pseudo channel suggest that the calibration of either 18GHz or 24GHz is not consistent.

As a second approach for assessment of AMSR-E calibration uncertainties, FLRRT charts of the TMI and AMSR-E data were compared. The FLRRT chart represents two dimensional freezing level and rain rate tables and it is constructed based on a scatter plot of the computed brightness temperatures of two channels: the 19 and 21GHz of TMI (the 18 and 24GHz of AMSR-E). To plot these FLRRT charts, July 2003 data over 5-0N, 170-175W, 5° x 5° box were taken (Fig 4.2).

In spite of modeling errors driven mainly by sea surface wind speed and cloud liquid water uncertainties, most probable rain rate over entire month is located reasonably well near zero rain rate for both cases. However, in the high brightness temperature region, the AMSR-E data show much more uncertainty than the TMI data. The TMI FLRRT (Figure 4.2a) show that the projected data (the pair of 19 and 21GHz vertical channels) very closely follow the lines which represent simulated freezing levels (3~6 km) and they are distributed mostly at the range between the 3km and the 5km. On the other hand, the behavior of the AMSR-E data (Figure 4.2b) shows some discrepancies with the

modeled freezing levels at high brightness temperatures (over 250K of 18GHz vertical channel) and some of the high brightness temperatures show unreasonably high freezing levels (over 6km). As a result, to account for those larger uncertainties of AMSR-E data, mean (T_0) and standard deviation (σ_0) of non-raining peak which are affected from the calibration uncertainties were adjusted in the operational algorithm.

Finally, to validate the refined operational algorithm, the global monthly rainfall map, which was plotted using Jan 2004 AMSR-E data, was compared with the same month of the official TRMM product from NASA DAAC (Distributed Active Archive Center) in Fig 4.3. The two figures match well within the same coverage area (40N~40S). The scatter plot (Fig. 4.4) and the overlapped rain rate histogram (Fig. 4.5) both for each 5° x 5° grid box-based rain totals are in good agreement as well.

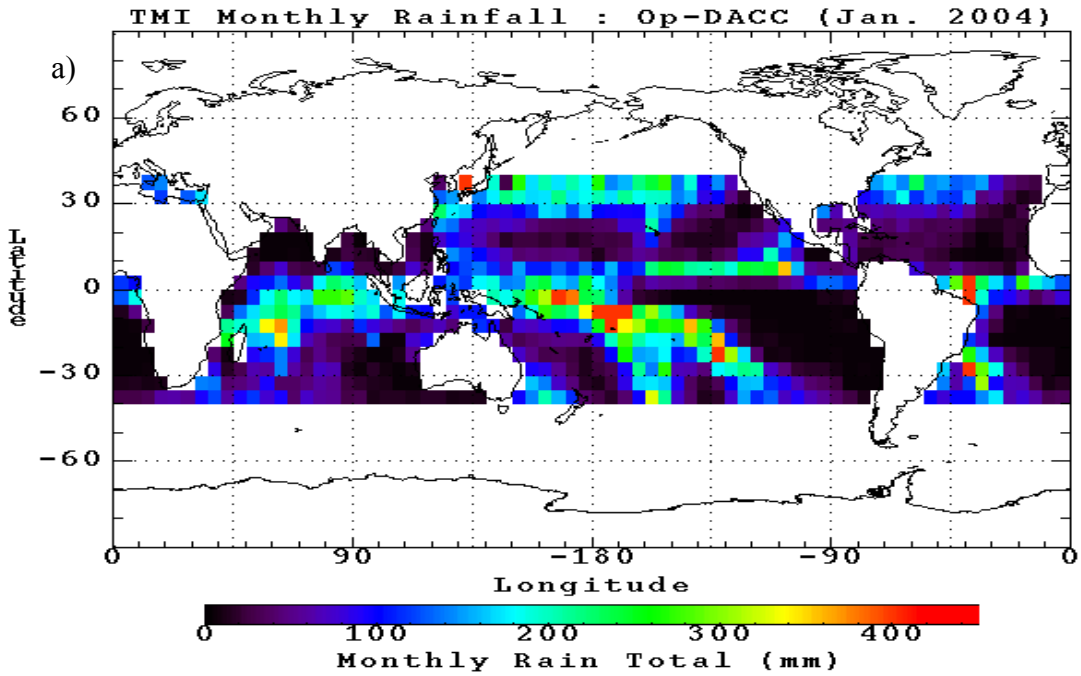

Figure 4.3 Monthly rainfall map of Jan 2004. a) from TMI data (official TRMM level 3 product), b) from AMSR-E data.

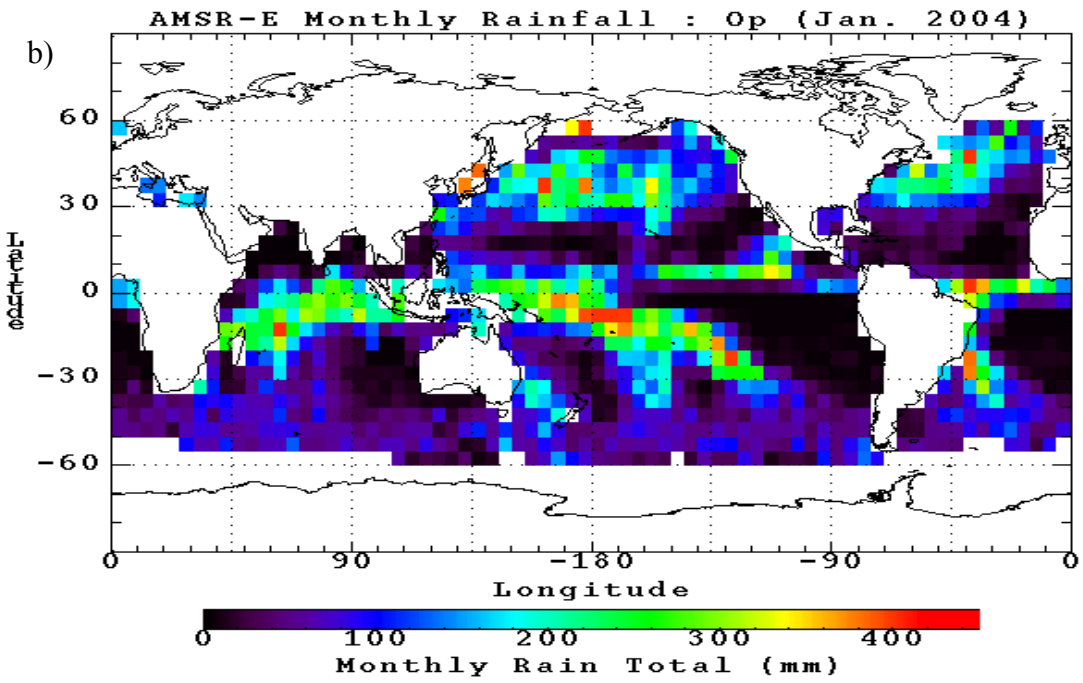

Figure 4.3, Continued.

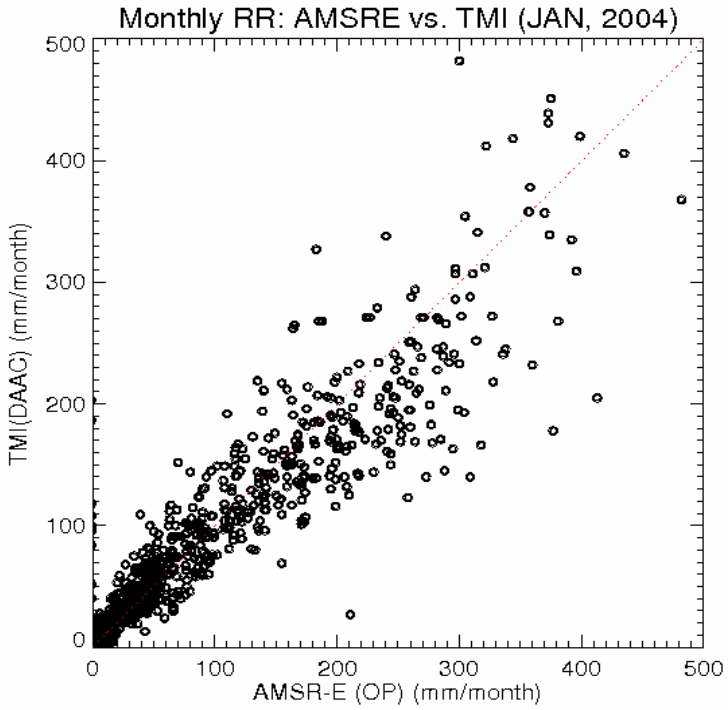

Figure 4.4 Scatter plot of monthly rainfall for AMSR-E and TMI over 5x5 grid boxes for Jan 2004 data.

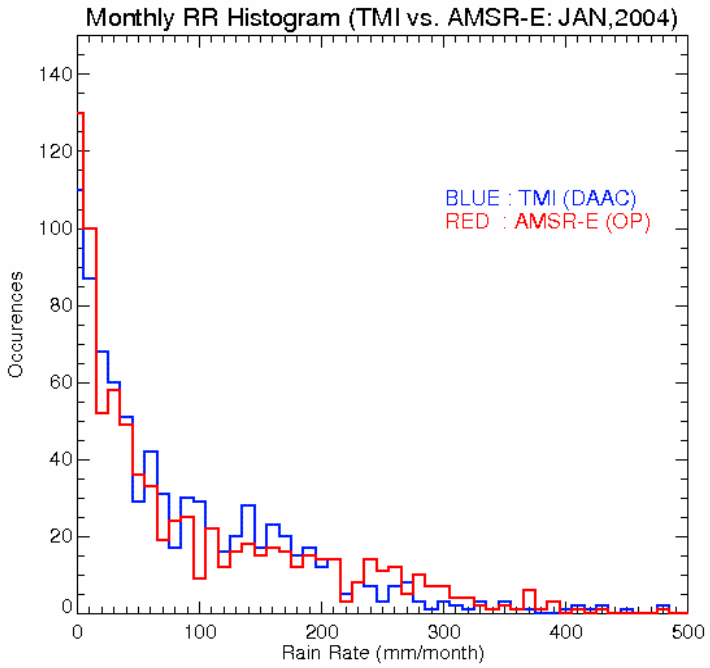

Figure 4.5 Comparison of monthly rain rate histograms: TMI vs. AMSR-E for Jan 2004.

4.2 Enhancement of the Experimental Algorithm

a. Improved offset correction scheme

To improve the experimental algorithm, we have developed additional schemes that can further minimize rainfall retrieval uncertainties. First, to achieve more precise offset corrections, we enhanced an offset correction scheme using the best rain rate resolution for the each channel instead of a fixed resolution for all channels. Specific values of each channel's resolution used in this study were 0.07, 0.039 and 0.018mm/h for 10, 18 and 37GHz respectively. Note that the highest resolution was applied for the 37GHz. Because most events for a month are small rain rate or zero rain cases and thus

most of these cases are covered by the 37GHz which has a small rain retrieval dynamic range, an accurate offset for the 37GHz channel is essential.

For an example, by applying the very high resolutions, rain rate histograms for three frequencies were generated over a 5°x5° grid box (5-10N, 150-155E) using July 2003 AMSR-E and TMI data and the offsets for both data sets were computed (Figure 4.6). In addition, to compute the random variability of the offsets, the rain rate histograms were separately generated for even and odd days of the month. The red line indicates odd day histogram and the blue line, even day. Figure 4.6 shows the estimated offsets for the three channels of vertical polarization. The measured offset values are dependent on their resolutions: the largest offsets for 10GHz and the smallest for 37GHz. The computed offset values for the particular box and month for the even days were 0.40 mm/h (10GHz), 0.081mm/h (18GHz) and -0.036mm/h (37GHz) for AMSR-E and 0.33 mm/h (10GHz), 0.237mm/h (19GHz) and -0.054mm/h (37GHz) for TMI respectively. Considering modeling errors driven mainly by the uncertainties of the sea surface wind speed and cloud liquid water content as well as calibration uncertainties, these extremely small biases observed in the 37GHz channels for both AMSR-E and TMI are quite striking.

The global maps of the computed offsets based on 5°x5° grid boxes were also plotted in Figure 4.7. This global distribution of the offsets over the ocean reveals the geographic dependence. It is assumed that this offset variability is due mainly to the geophysical biases driven by mean surface wind speed, non-precipitating cloud water as well as freezing level uncertainties and coastline or nearby land contamination effects. This means that many of those uncertainties can be absorbed by the offset corrections.

By dividing the data into even and odd days, the random variability in the offsets was also computed. The variability of the offsets (even –odd offsets) was plotted as a function of longitude (Figure 4.8) to detect any meridional dependency of offsets. The computed root mean square errors of the offsets for the horizontally polarized 37GHz (Figure 4.8) are about 0.09 and 0.07 mm/h for AMSR-E and TMI respectively. Overall, the variability of the offsets of AMSR-E data was larger than that of TMI data except 37GHz (vertical channel). The statistics of the random variability of the offsets for all three channels (10, 19 and 37GHz) which were computed by partitioning into even and odd days are summarized in Table 4.1.

a)

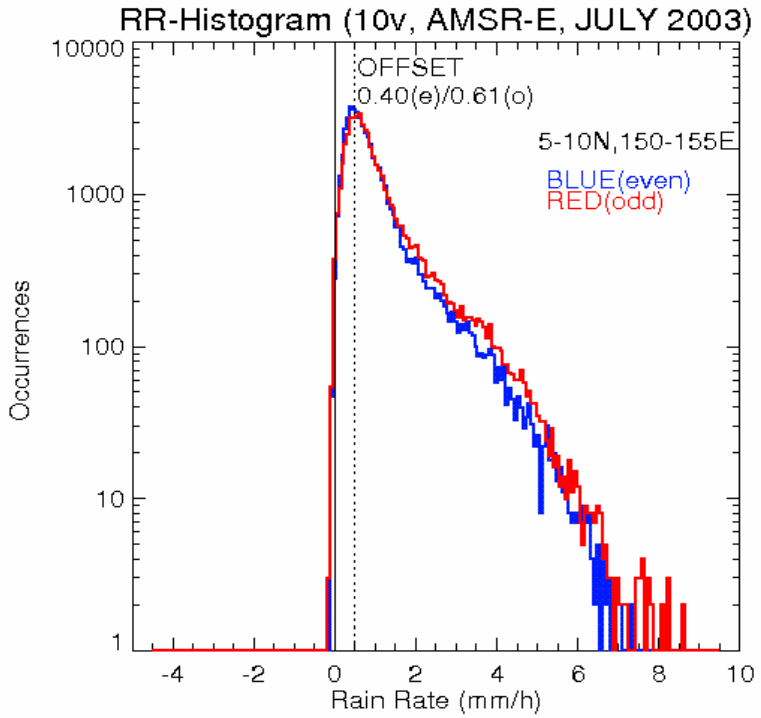

Figure 4.6 Estimated offsets from rain rate histograms over 5-10N, 150-155E 5°x5° box for July 2003 data. a) 10GHz (V-pol), AMSR-E, b) 10GHz (V-pol), TMI, c) 18GHz (V-pol), AMSR-E, d) 19GHz (V-pol), TMI, e) 37GHz (V-pol), AMSR-E, f) 37GHz (V-pol), TMI.

b)

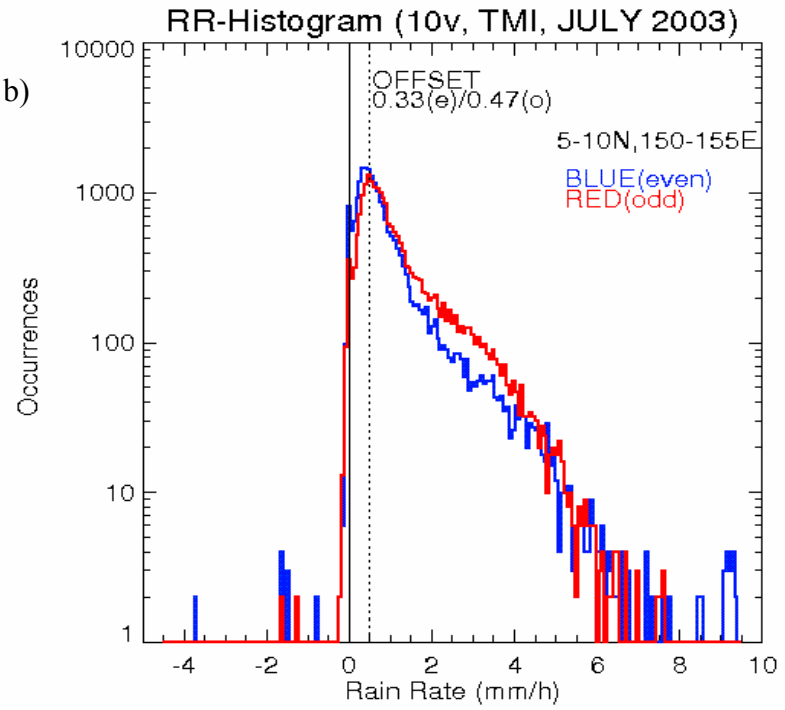

c)

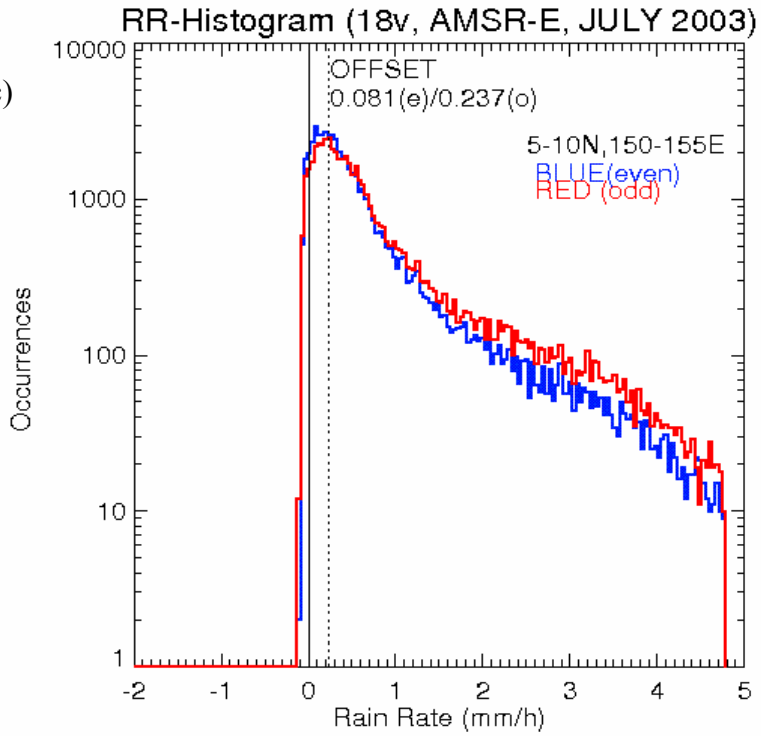

Figure 4.6, continued.

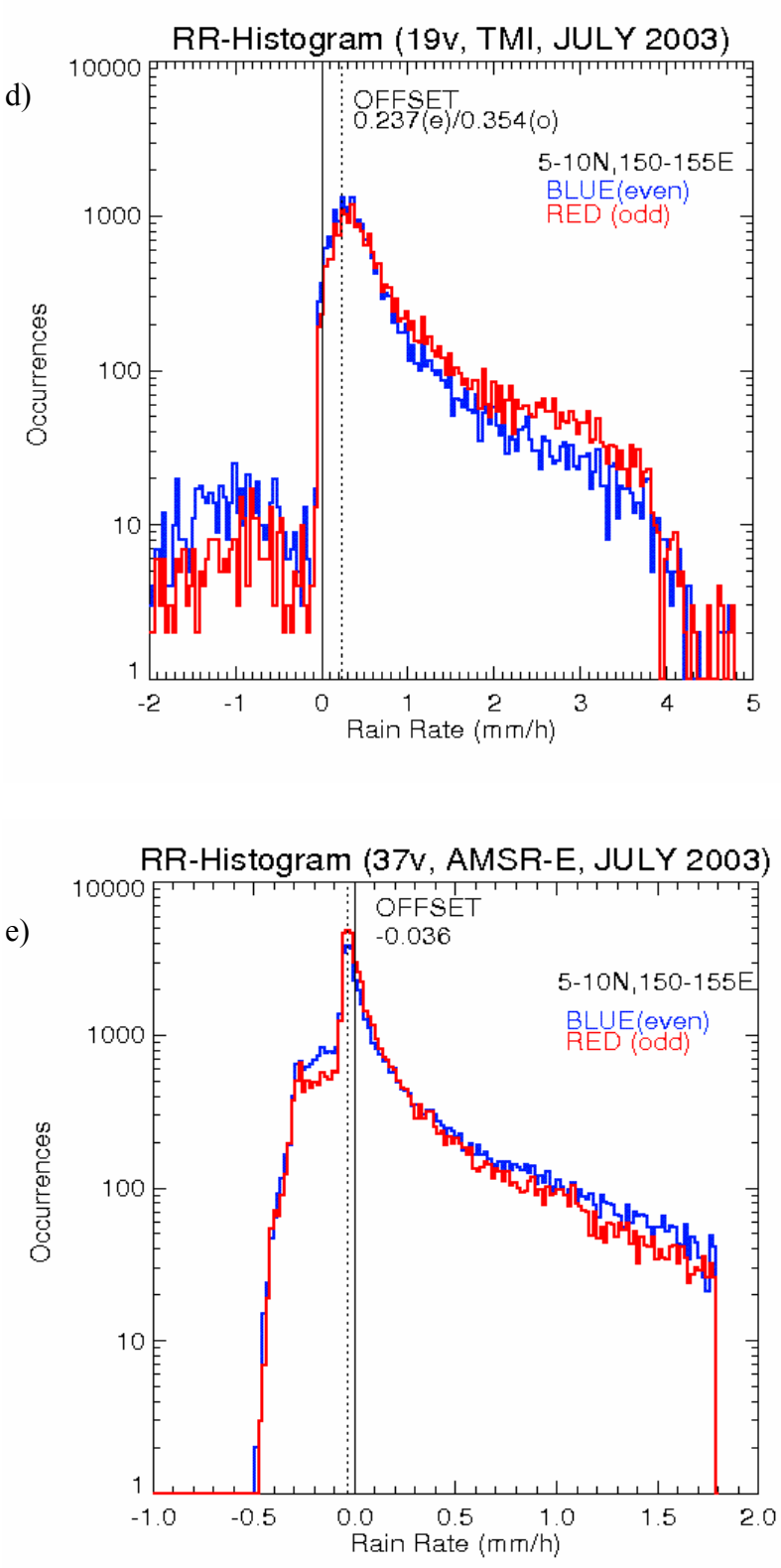

Figure 4.6, continued.

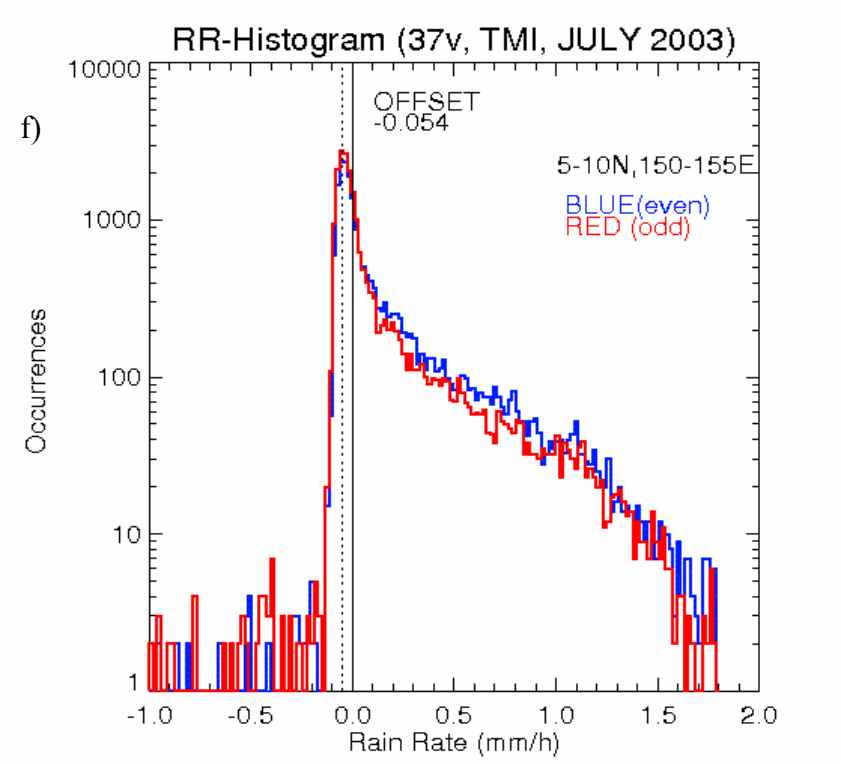

Figure 4.6, continued.

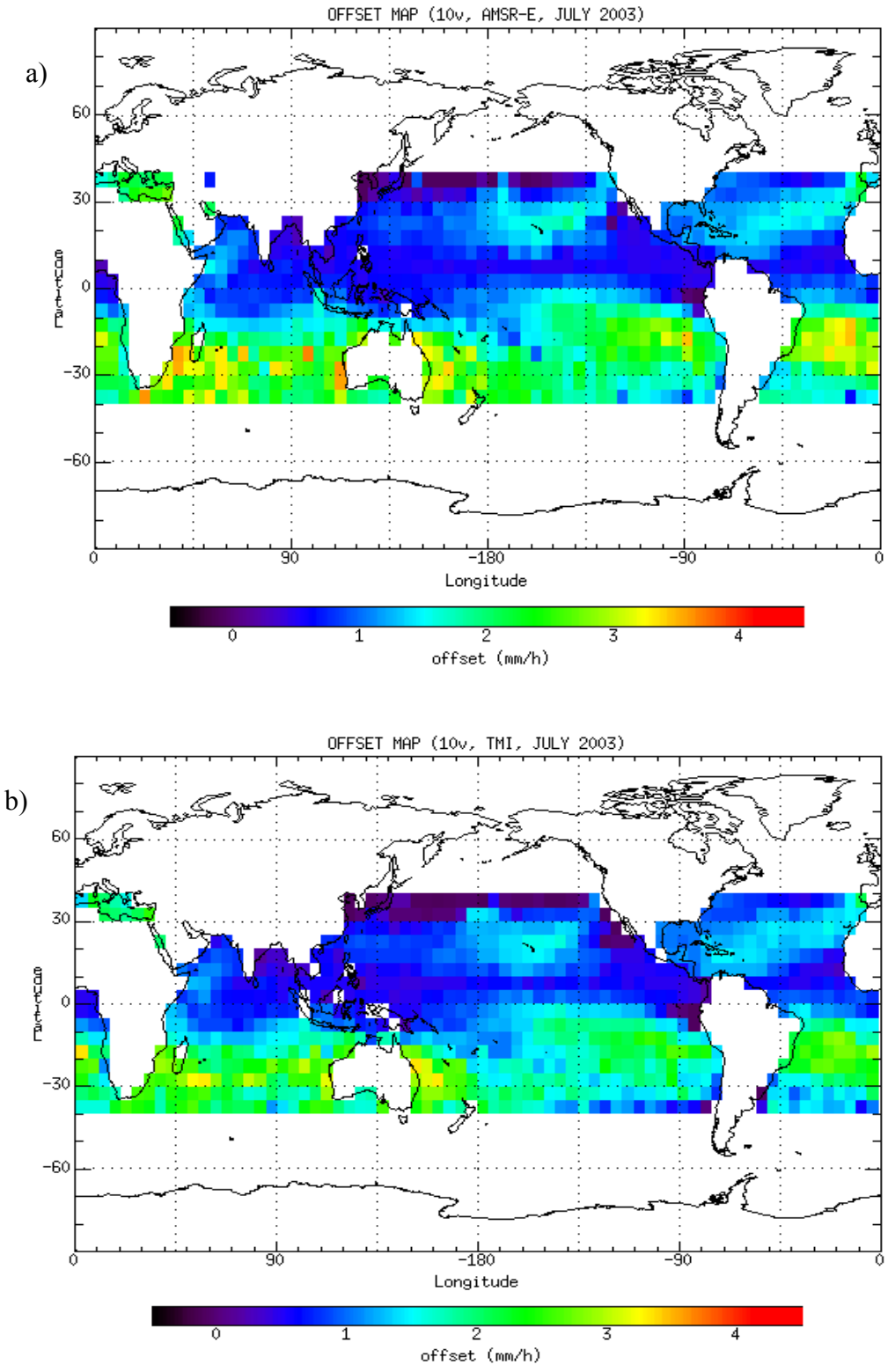

Figure 4.7 Global offset map over 5°x5° boxes for July 2003 data. a) 10V (AMSR-E), b) 10V (TMI) c) 18V (AMSR-E), d) 19V (TMI), e) 37V (AMSR-E), f) 37V (TMI).

c)

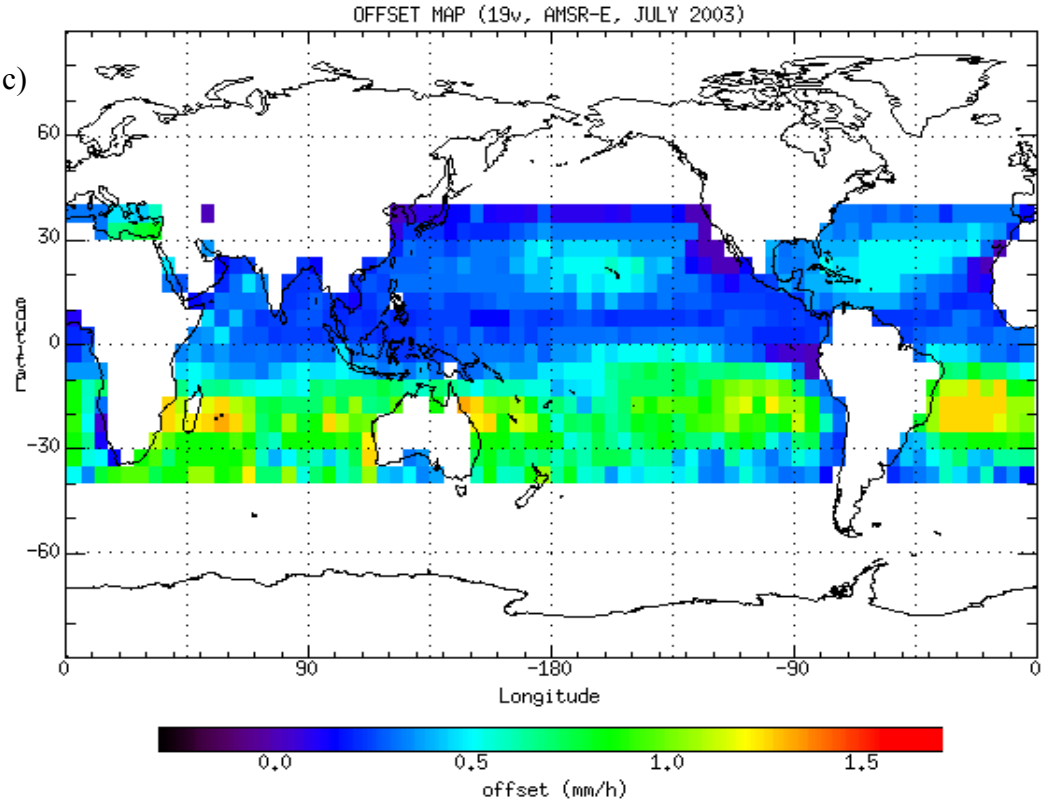

d)

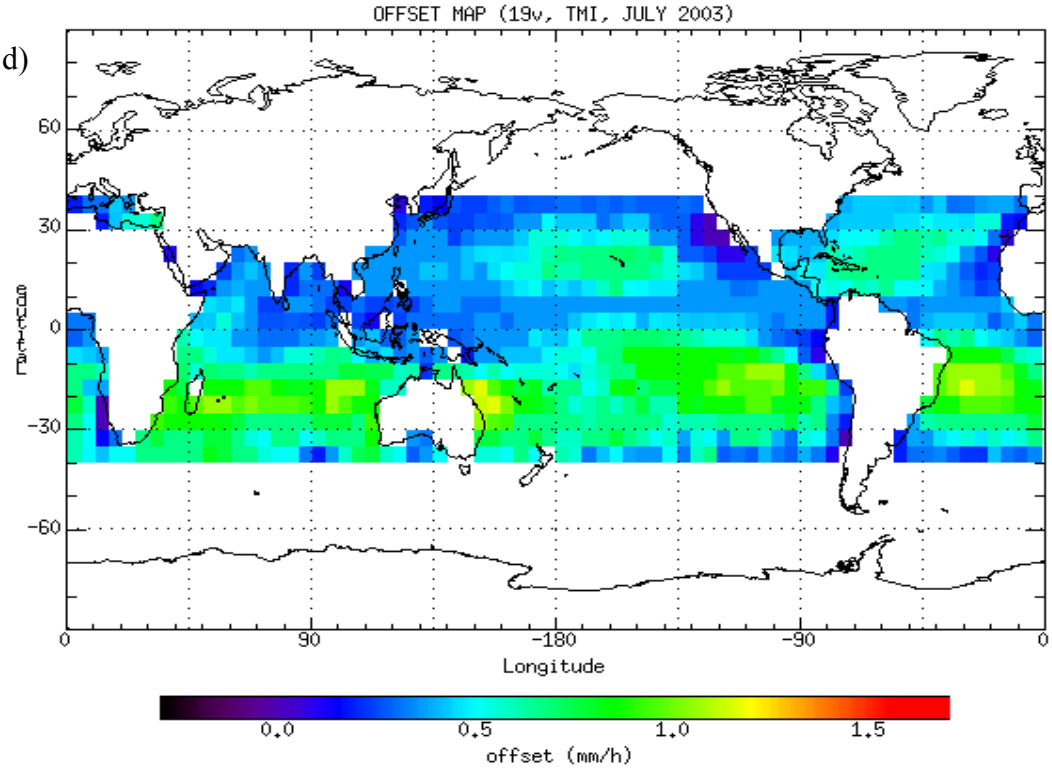

Figure 4.7, continued.

e)

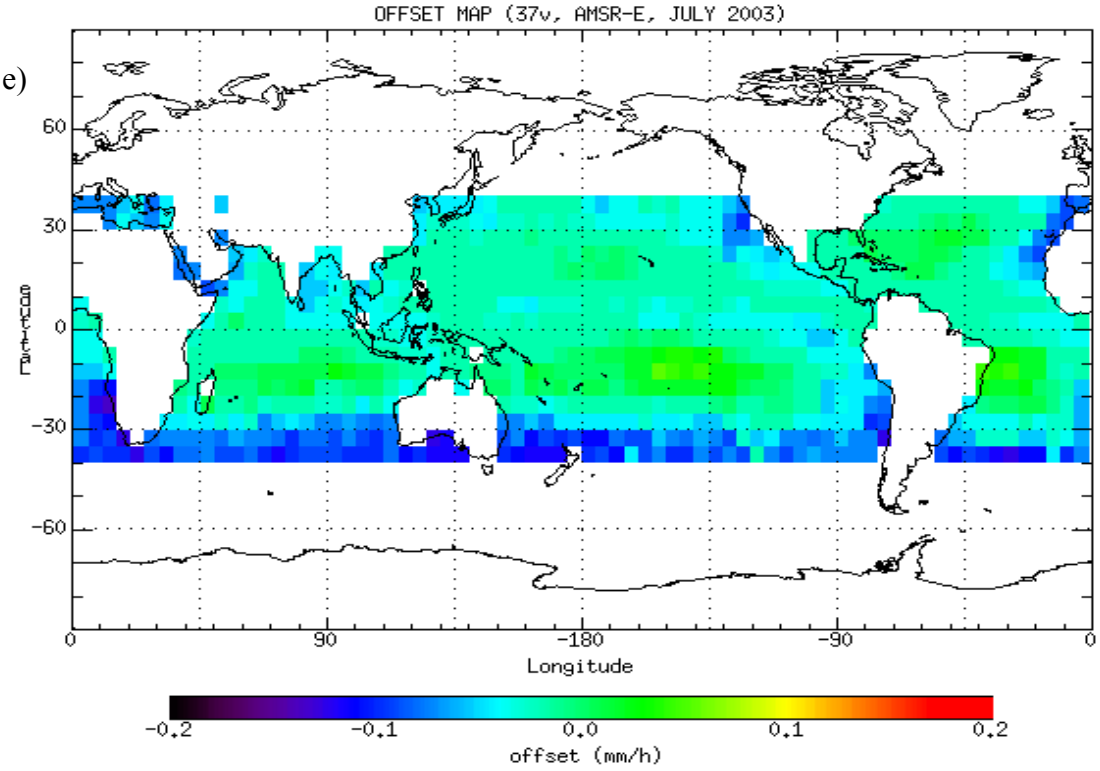

f)

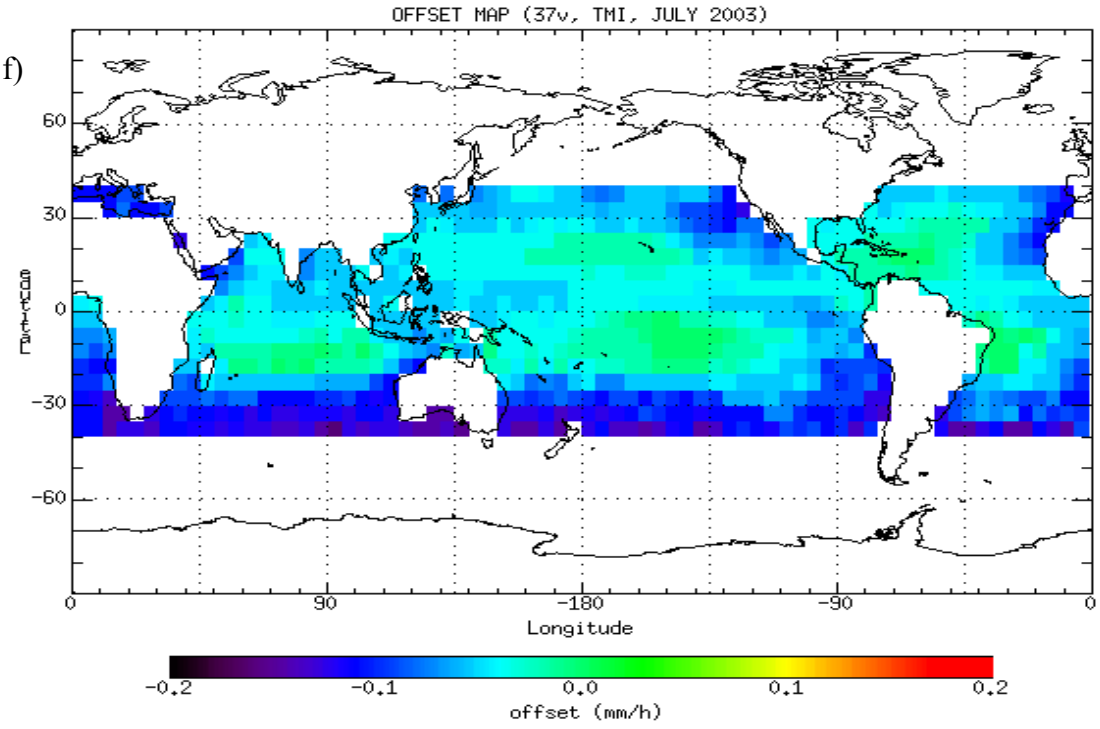

Figure 4.7, continued.

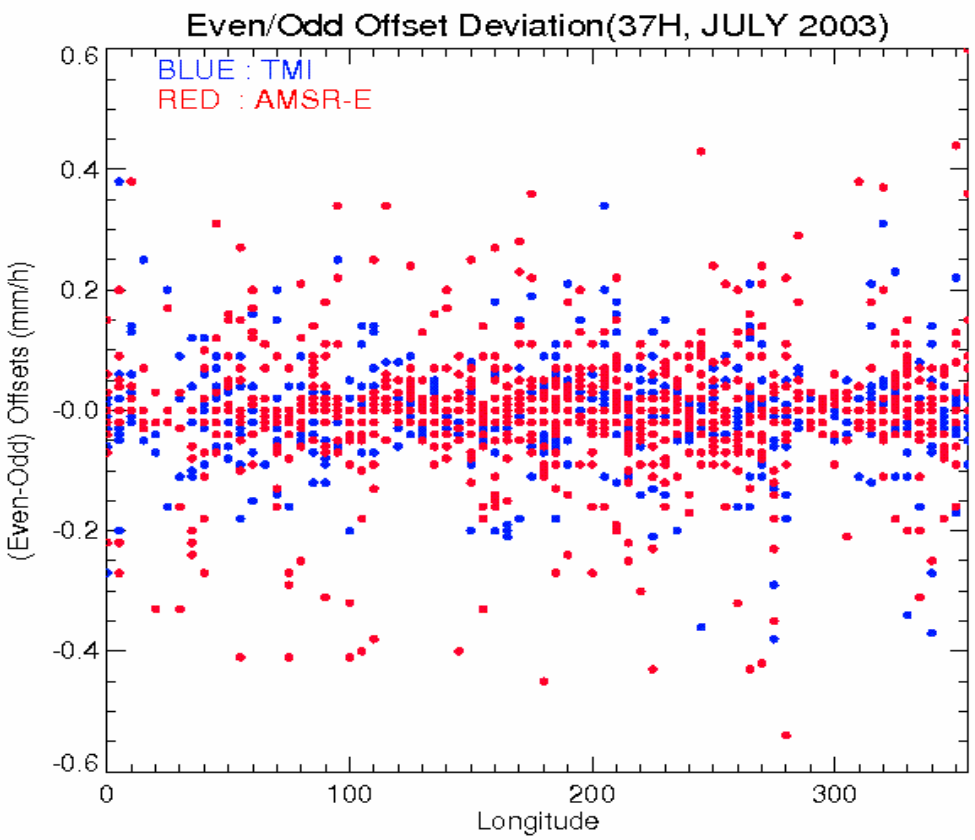

Figure 4.8 Comparison of the random variability of offsets (even -odd offsets): TMI (blue) vs. AMSR-E (red) from July 2003 data.

Table 4.1 Computed root mean square errors of the offsets by partitioning even/odd days of July 2003 data.

	AMSR-E	TMI
10V	0.492009 mm/h	0.408823 mm/h
10H	0.499278 mm/h	0.390270 mm/h
19V	0.149374 mm/h	0.111560 mm/h
19H	0.155403 mm/h	0.095092 mm/h
37V	0.033394 mm/h	0.038133 mm/h
37H	0.094695 mm/h	0.069910 mm/h

b. Weighted average scheme

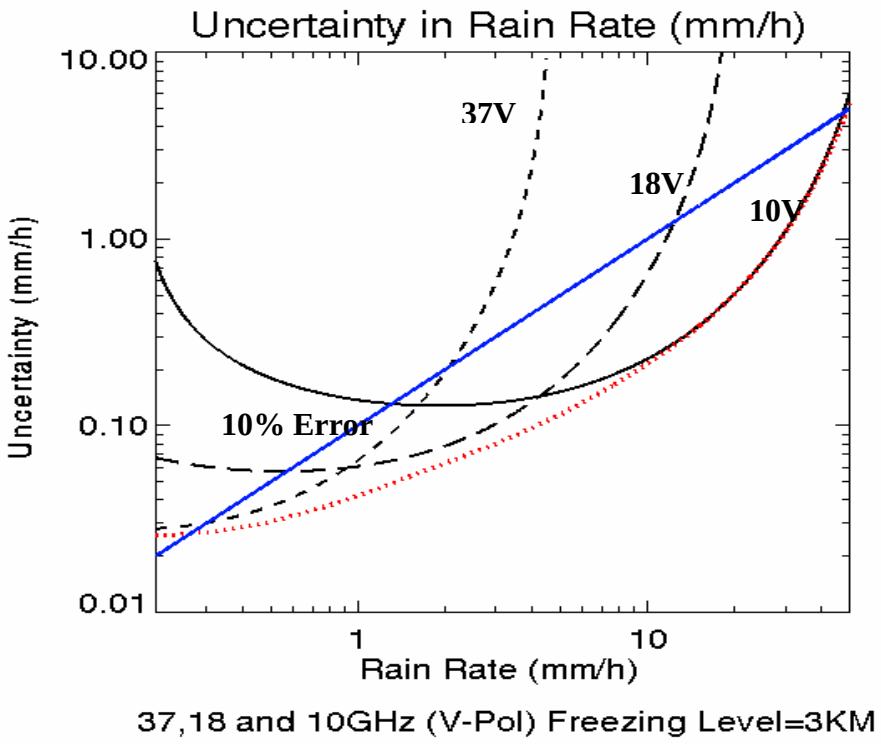

Figure 4.9 Simple model of optimal weighting of three (37, 18 and 10GHz-vertically polarized) channels. Rain rate uncertainty was computed based on a 2K calibration uncertainty, a 0.5K radiometer noise. Assumed freezing level was 3km.

To utilize all six channels' advantages fully and to reduce uncertainties of the rain rate retrieval, we designed a "weighted average scheme" so that the weighted average of the six rain rates can minimize the uncertainties in rain rate. Figure 4.9 shows an example of designing of an "optimally weighted combination" of three channels (37, 18 and 10GHz). In this case, only instrument noise and calibration uncertainties were considered for an analytical illustration. For each channel, the uncertainty in the rain rate was computed based on a 2K calibration uncertainty and a 0.5K radiometer noise. The calibration error was assumed near zero at zero rain rate brightness temperature,

accounting for the offset correction and it was increased linearly up to the limiting brightness temperature that represents the equivalent effective radiating temperature of the rain layer (about 285K). In the Figure, the 37GHz has the lowest uncertainty at light rain rates (in the range of less than 1mm/h) and the 18GHz has less than 10% uncertainty (straight line) at approximately 1mm/h to 5mm/h. The 10GHz channel gives us less than 10 % uncertainty from about 5mm/h up to 50mm/h. The estimated rain rate uncertainties from an optimal weighting were also indicated in the dotted line. It is clearly shown that a large fraction of the uncertainty in rain rate was minimized. The simple optimal weighting scheme used for this analytical illustration is described in Appendix A.

Based on the simplified weighing scheme for the cases which are independent and uncorrelated, we've built up the weighed average method to merge optimally the six rain rates for monthly rain total estimation. However, computing the appropriate weights for merging six rain rates (from the dual polarized 37, 18 and 10GHz channels) in the rainfall algorithm are much more complex because the weight for each channel needs to be estimated based on properly computed uncertainties on a pixel-by-pixel basis. As major uncertainties for estimating the weights, beam filling error (BFC) and drop size distribution uncertainty (DSD) along with calibration uncertainty (CAL) and instrument noise uncertainty (NEΔT) were considered. The total uncertainty was computed by summing those uncertainties.

However, errors are divided into two components: correlated (systematic) and uncorrelated (random) parts and each part should be treated differently in the computation. In the case of uncorrelated errors, total errors are computed as simply adding all error variances. If measurements are correlated (coupled), we assumed that

measurements are perfectly correlated, and thus we add the amplitudes of the coupled errors. All errors can be partitioned into random and perfectly correlated parts.

c. Freezing level retrieval improvements

When TMI data were used for the experimental algorithm, only the vertically-polarized (V-pol) channels of 19 and 21GHz were utilized to retrieve freezing levels because the TMI does not have a horizontally-polarized (H-pol) 21GHz channel. However, AMSR-E has H-pol channels for both 18 and 24 GHz. Thus, we used the H-pol channels along with the V-pol channels for the freezing level retrieval. Figure 4.10 shows comparison of the FLRRT chart using the V-pol and the H-pol. When the H-pol channels are used, there is a larger change of brightness temperature for a given change in the freezing level. As a result, the impact of calibration and NEΔT uncertainties of AMSR-E data was mitigated.

Moreover, we examined better thermodynamic assumptions resulting in a more reasonable relationship between precipitable water and freezing level. Since freezing level is a proxy variable for not only the raining column height but also the upper limit of water vapor in a radiative transfer model, the freezing level retrieval must be derived from appropriate model assumptions to give us a reasonable relationship between precipiatable water and freezing level. The original assumption using 6.5K/km of lapse rate as a standard temperature profile yields unreasonably high precipitable water values at high freezing levels (> 5km). Rangno and Hobbs (2005) presented that the average lapse rate value over the tropics is 5.3K/km by analyzing the KWAJEX data.

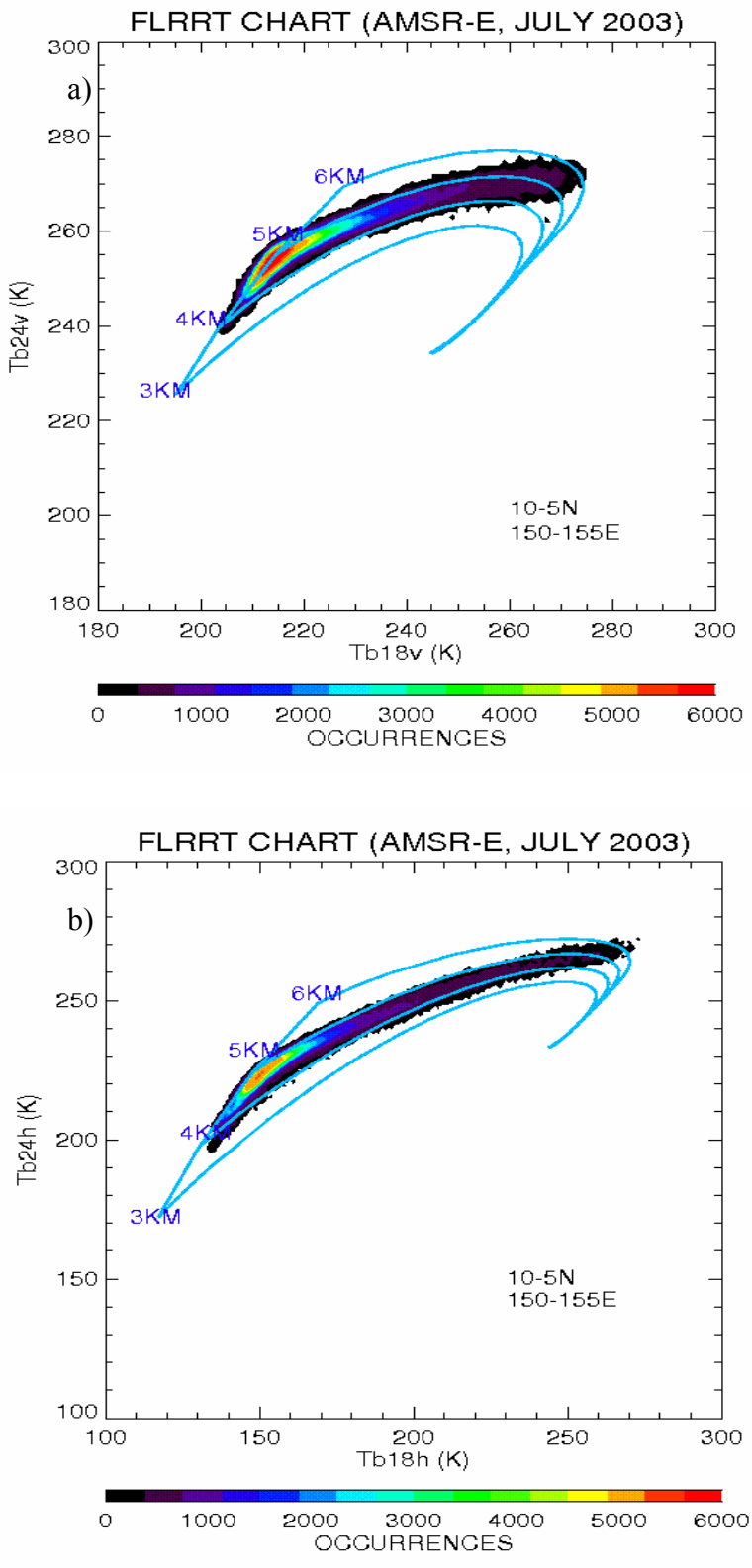

Figure 4.10 Comparison of FLRRT chart using a) V-pol channels and b) H-pol channels for the 10-5N, 150-155E grid box for July 2003 AMSR-E data.

In addition to the lapse rate assumption, the impact of the modified water vapor model by Thomas-Stahle (2001) which has 5% reduced line width parameter compared to the original Rosenkrantz model (Rosenkrantz, 1993, 1998) was tested. Cimini et al. (2003) and Mattioli et al. (2005) suggested that there is a no unique forward model after testing four different water vapor models that were used for their simulation. Their study revealed that the simulated brightness temperatures from the four water vapor models show large uncertainties (maximum 5K difference) in tropical environments. Thus, the modeling uncertainty of the water vapor spectroscopy is an important uncertainty source of the freezing level retrieval and should be properly taken into account.

Consequently, as a new thermodynamic profile in the radiative transfer model, we adopted a mixed lapse rate assumption (5.3K/km lapse rate below the FL and 6.5K/km lapse rate above the FL) and the original water vapor model (Rosenkranz, 1993, 1998). Figure 4.11 shows that the new adjustments provide more reasonable integrated water vapor amounts from which the equivalent freezing levels can be approximated. Note that at low freezing levels there is little sensitivity to the changed lapse rate assumption.

By applying the new thermodynamic assumption, the new FLRRT charts for both TMI (vertical channel only) and AMSR-E (both polarizations) over a particular 5° x 5° grid box for the July 2003 data were generated in Figures 4.12a-c. For comparison, the dotted lines which indicate the results from the original assumption were overlapped. They show that more reasonable freezing levels are achieved from the changed thermodynamic approximations: In case of the new FLRRT, around 4.5km of mean freezing level is retrieved while around 4km of mean freezing level is estimated from the original assumption.

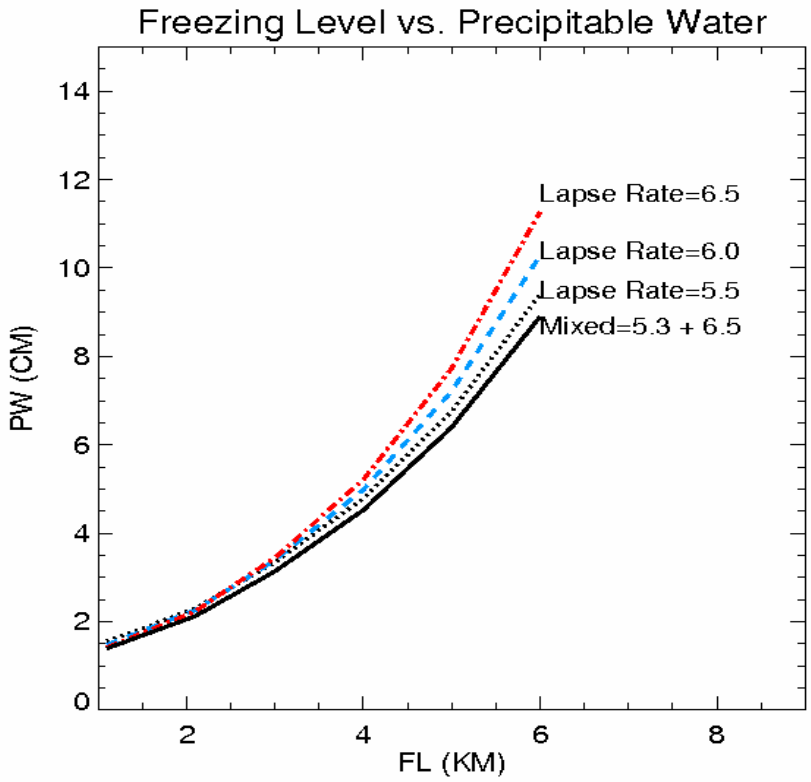

Figure 4.11 Relationship between freezing level and precipitable water as a function of lapse rate.

a)

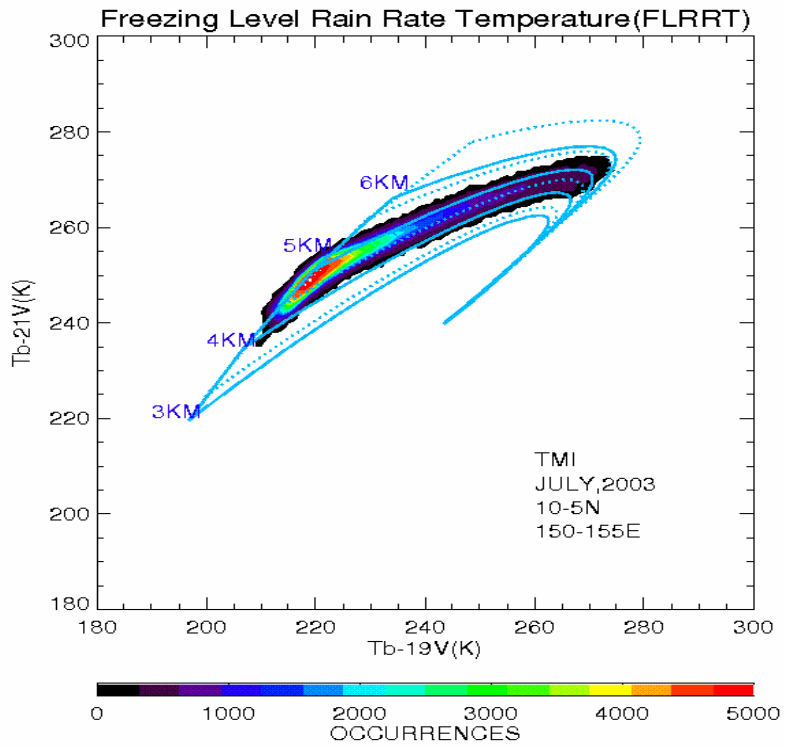

b)

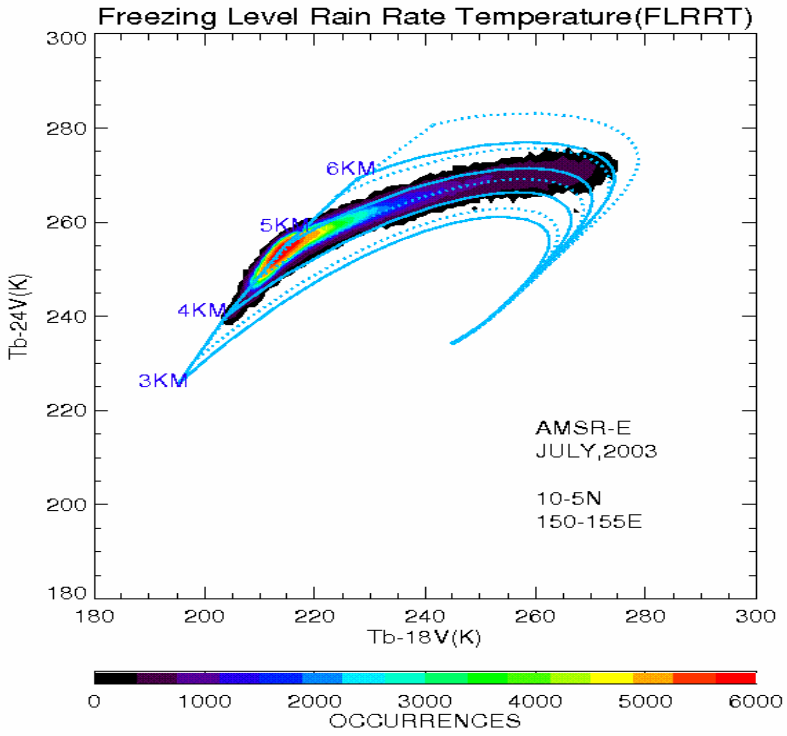

Figure 4.12 FLRRT based on the mixed lapse rate and original water vapor model: a) FLRRT from July 2003 TMI data b) FLRRT from July 2003 AMSR-E data using 18 and 24GHz vertical channels, c) FLRRT from July 2003 AMSR-E data using 18 and 24GHz horizontal channels.

c)

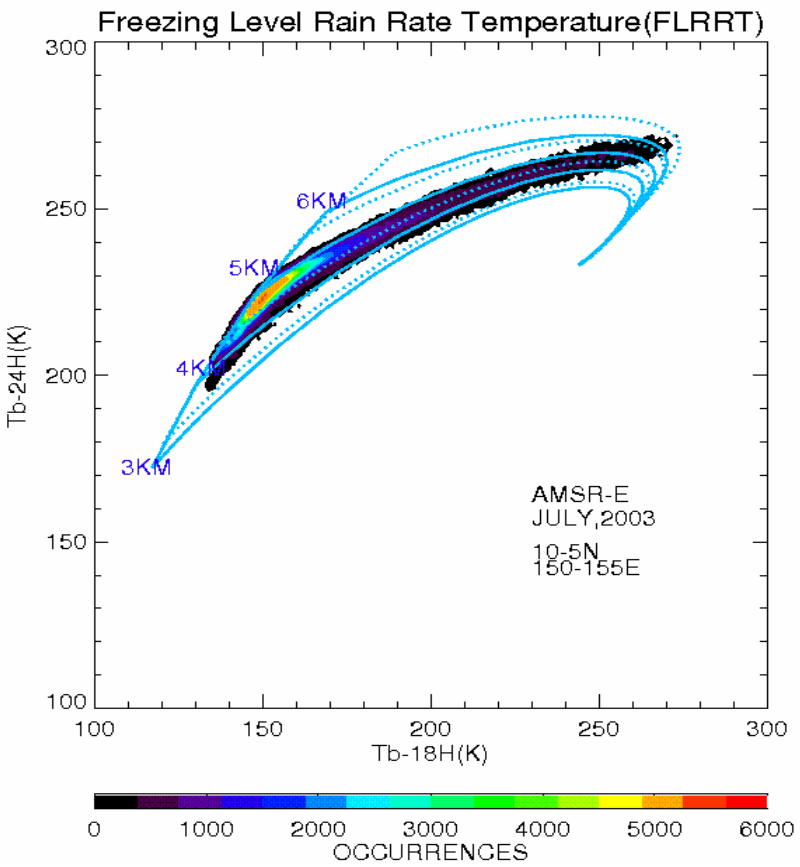

Figure 4.12, Continued.

4.3 Error Models

Error models were established to quantify rainfall retrieval uncertainties and to compute proper weights for merging of the six rain rates. As primary error sources of the rainfall retrieval, beam filling correction error (BFC), drop size distribution uncertainty (DSD), calibration uncertainty (CAL) and instrument noise (NEΔT) were considered. In addition to these errors, sampling errors were also taken into account as an error source of the monthly rain totals (Level 3 product), but not for determining the weights.

a. BFC

Beam filling error is caused by the combined effect of the inhomogeneity of rainfall within the field of view (footprint size) and the non-linear behavior of the R-T relationship (concave downwards shape). This beam filling error leads to underestimation of rain rate when the face value of rain rate corresponding to the observed brightness temperature is taken. The ratio of the true mean rain rate within the field of view to the face value of the rain rate is referred as a beam filling correction factor (BFC). The analytical form of the BFC was designed by Wang (1996) as follows.

$$BFC=1.0 + (0.478LOG(S)-0.687)/Rc,\ S<=60$$

Where, Rc is the characteristic rain rate in the analytical expression for the R-T relationship (Section 2.3) and S is the longer radius of footprint size in km. Combining this with the equations of Section 2.3 results in

$$BFC=1.0 + (0.478*LOG\ (A) -.687)*(FL^{B})/C$$

The constants which are used in the formula are listed in Table 4.2.

The BFC is proportional to the logarithm of the size of field of view and is inversely proportional to the characteristic rain rate which depends on the frequency and the freezing level. Because the footprint size dependence is logarithmic, the characteristic rain rate has the dominant effect rather than the field of view size. Therefore, the 10GHz channel has smallest beam filling errors among the three channels (10, 18 and 37GHz) due to its largest characteristic rain rate. The computed BFC as a function of freezing level is shown in Figure 4.13. Besides, to account for the two components of the BFC error (non-systematic and systematic errors), we approximated that the standard deviation (σ) of beam filling correction factor due to the random error in the BFC is about 1.5C

(where, C=BFC-1) and due to the correlated error is 0.3C based on the beam filling error study using KWAJEX and TOGA CORE airborne radar data sets (Chen, 2003; Figure 4.14).

Table 4.2 Constants in BFC formula.

	A	B	C
10GHz	40	1.315	75.38
18GHz	21	1.928	58.26
37GHz	12	0.54	5.9

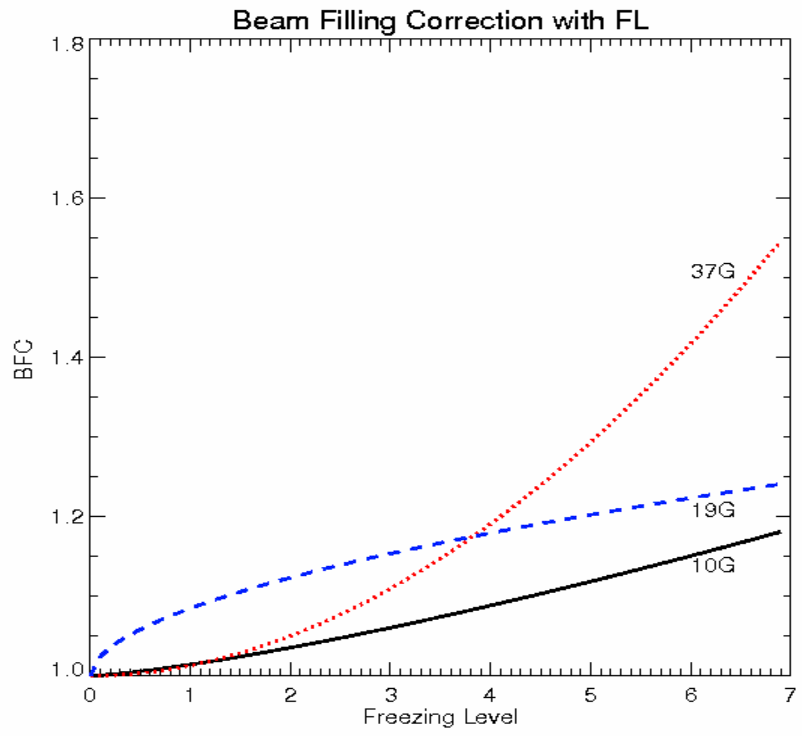

Figure 4.13 Beam filling correction factor with freezing level for the 37, 19 and 10GHz frequencies.

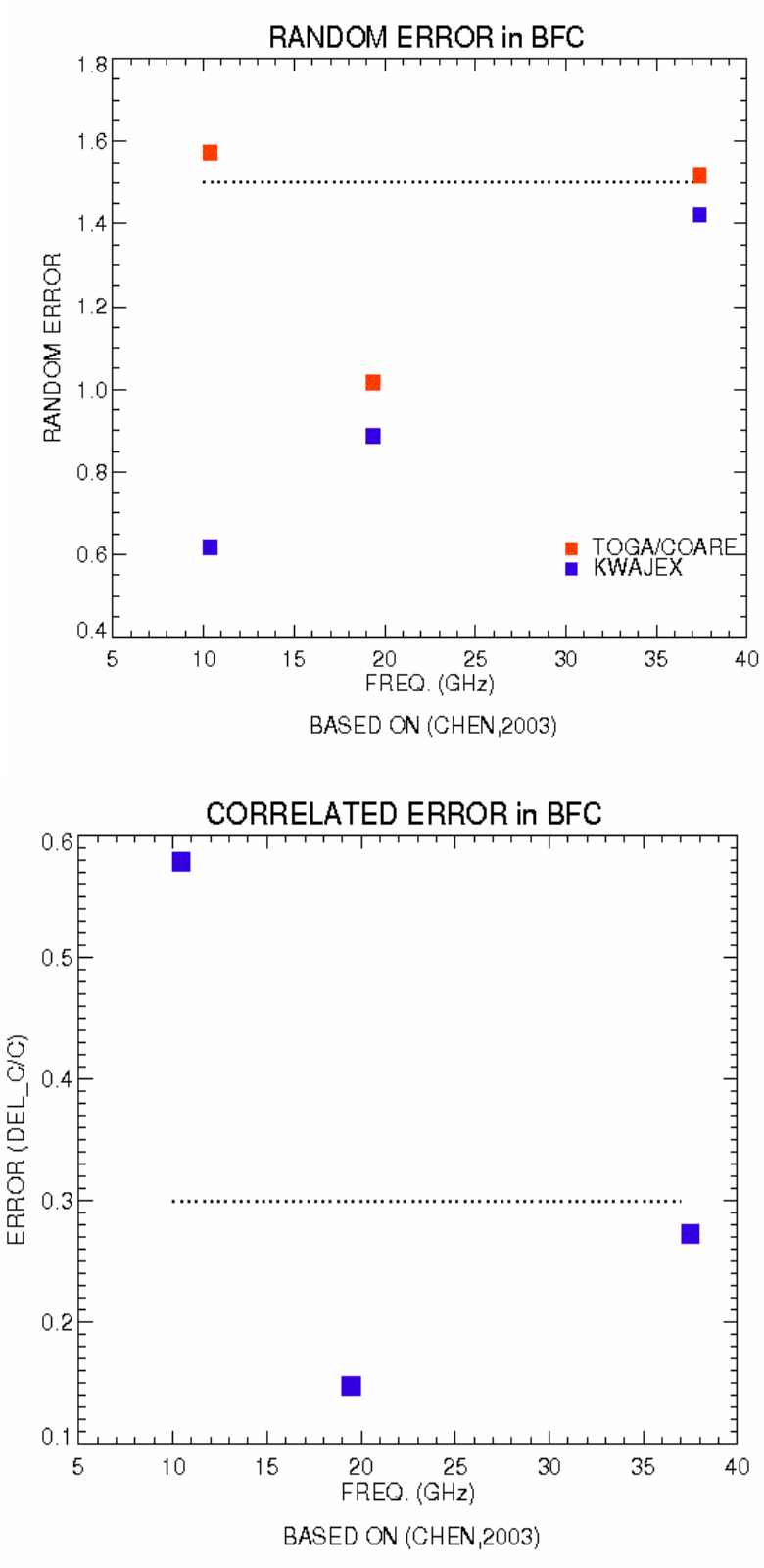

Figure 4.14 Random and correlated beam filling errors based on Chen (2003).

b. DSD

To address the uncertainty driven by the DSD, the sensitivity of the three frequencies that are used in our rainfall retrieval to the DSD was computed. Based on Chandrasekar et al. (2003) we assumed that N_w, the intercept value of the drop size distribution which is expressed as $N(r) = N_w \cdot \exp(-\Lambda r)$, has a range of from $N_0 \times 1/\sqrt{10}$ to $N_0 \times \sqrt{10}$ (in other words, $LOG_{10}(N_w) = LOG_{10}(N_0) \pm 0.5$), where N_0 is the intercept value of the original M-P DSD.

In Figure 4.15, the variability of the 10GHz brightness temperatures for the assumed minimum and maximum values of N_w is shown. The impact of N_w on the brightness temperature change becomes more dominant as rain rates increase. The computed rain rate uncertainty along with the percentage uncertainty contribution caused by the DSD uncertainty as a function of rain is plotted in Figures 4.16, 4.17 and 4.18. Figure 4.19 shows relative percentage contribution of rain rate uncertainty by the three frequencies. In these figures, the assumed freezing level was 4km. While the impact of the variability of DSD is significant at the 37GHz, overall net uncertainty contributions are dominated by the 10GHz since the 37GHz's uncertainty contributed by the DSD is minimal due to its very narrow dynamic range (< 2mm/h).

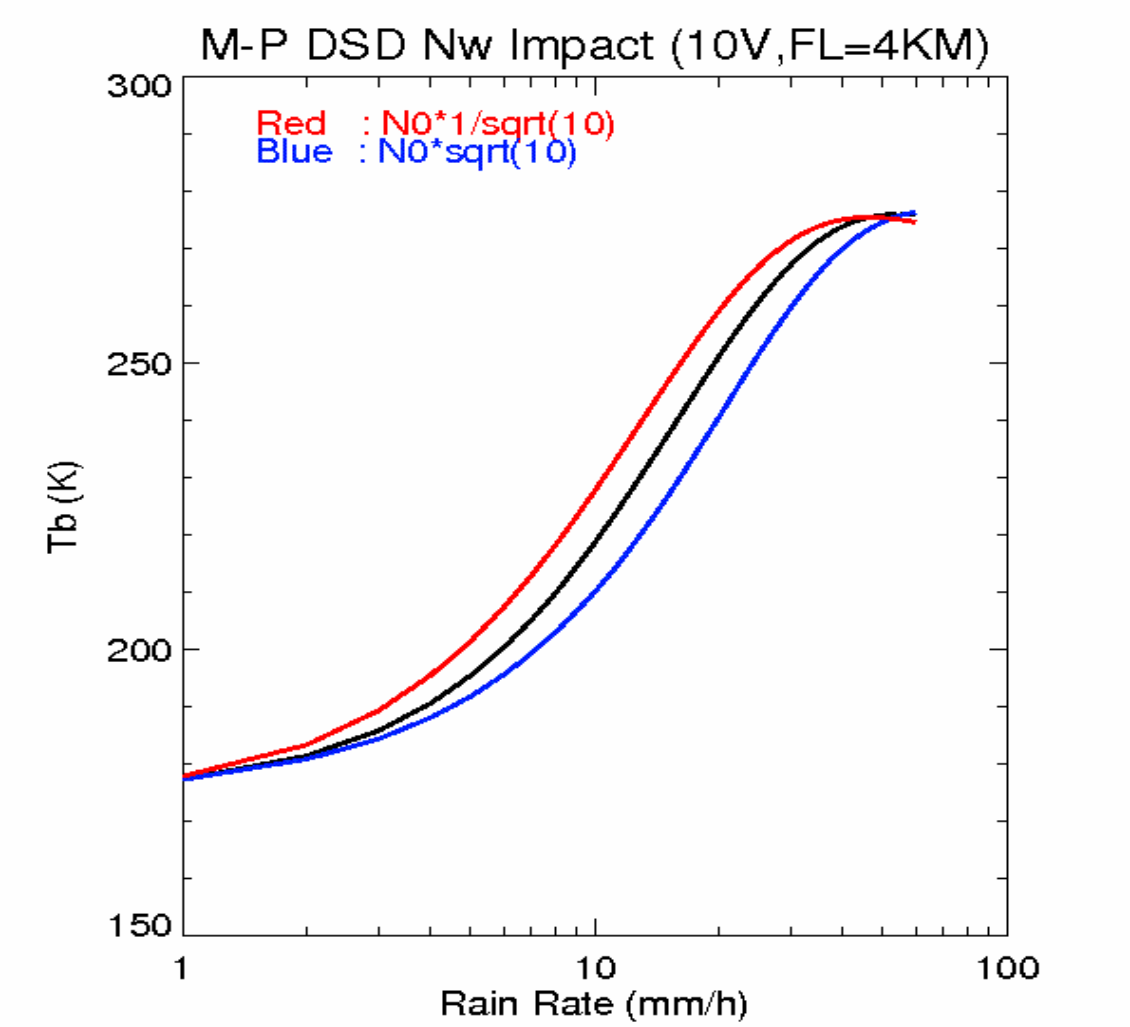

Figure 4.15 Sensitivity of the brightness temperatures corresponding to the N_0 were examined based on the minimum (red) and maximum (blue) value of N_0 based on Chandrasekar (2003).

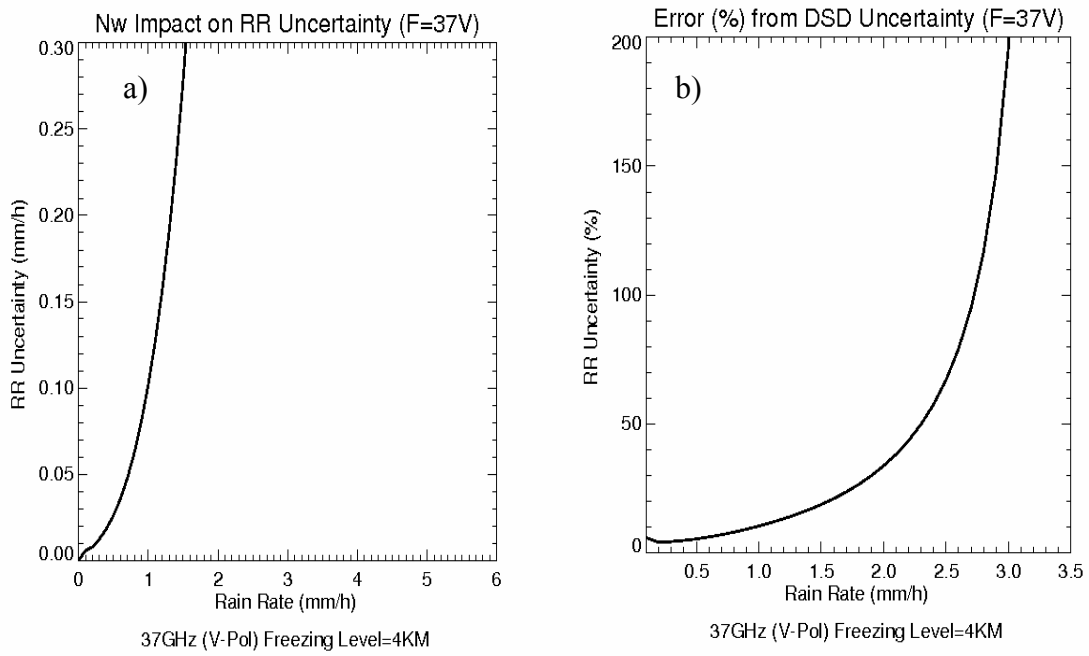

Figure 4.16 Impact of the DSD uncertainty on the rain rate uncertainty for the 37GHz, vertical channel. a) Computed rain rate uncertainty caused by the DSD, b) percentage rain rate uncertainty contribution driven by the DSD.

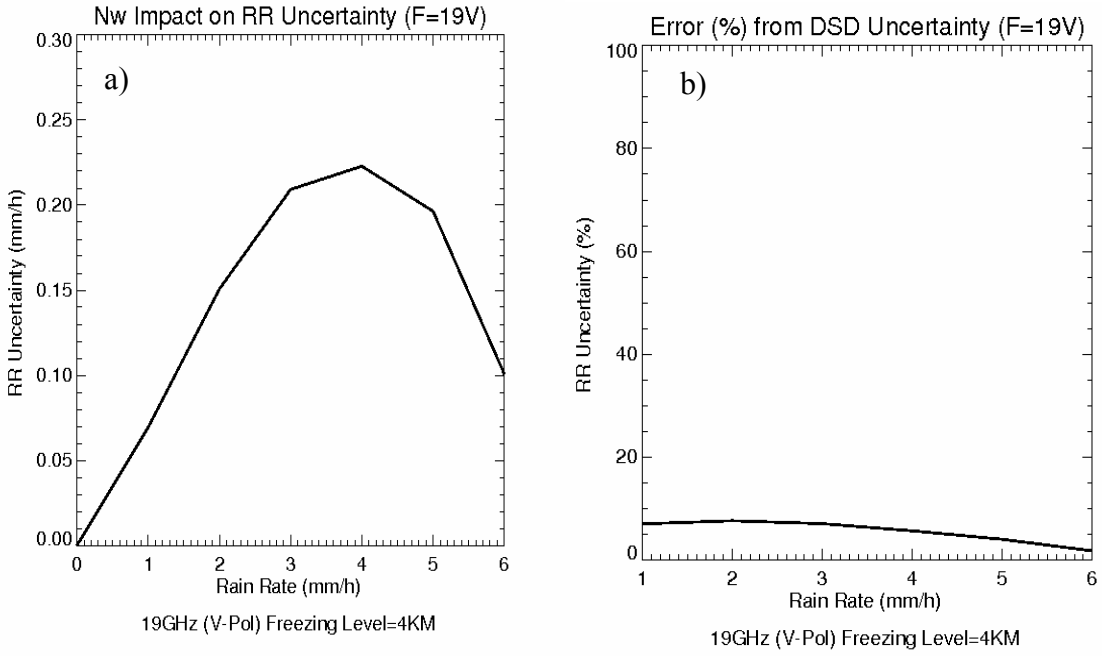

Figure 4.17 Impact of the DSD uncertainty on the rain rate uncertainty for 19GHz, vertical channel. a) Computed rain rate uncertainty due to the DSD as a function of rain rate, b) percentage rain rate uncertainty contribution driven by the DSD.

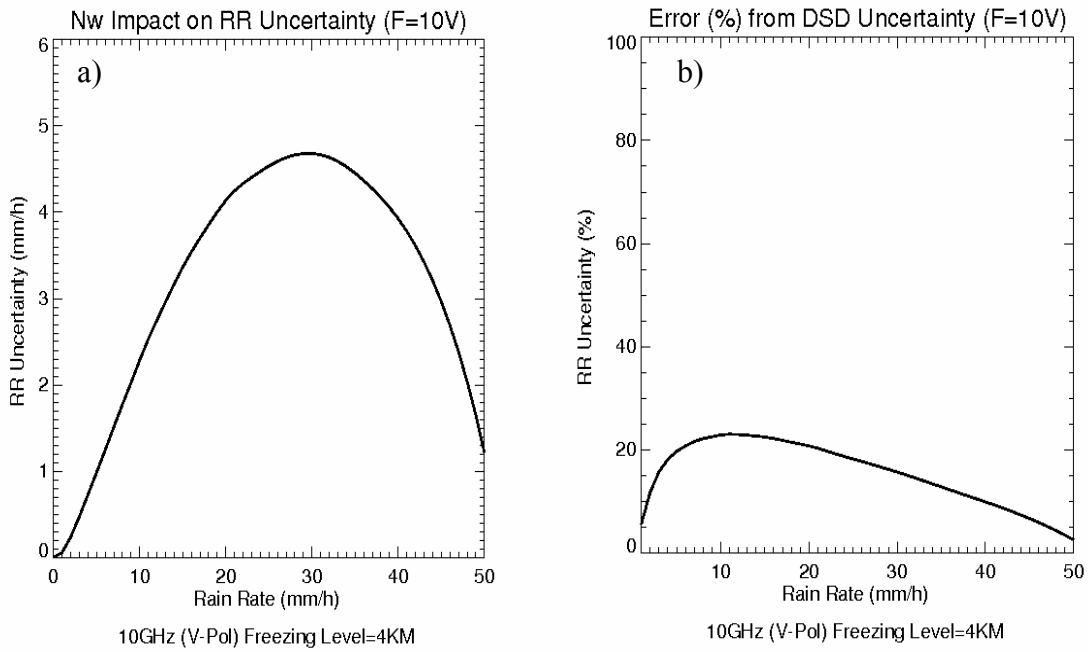

Figure 4.18 Impact of the DSD uncertainty on the rain rate uncertainty for 10GHz, vertical channel. a) Computed rain rate uncertainty due to the DSD as a function of rain rate, b) percentage rain rate uncertainty contribution driven by the DSD.

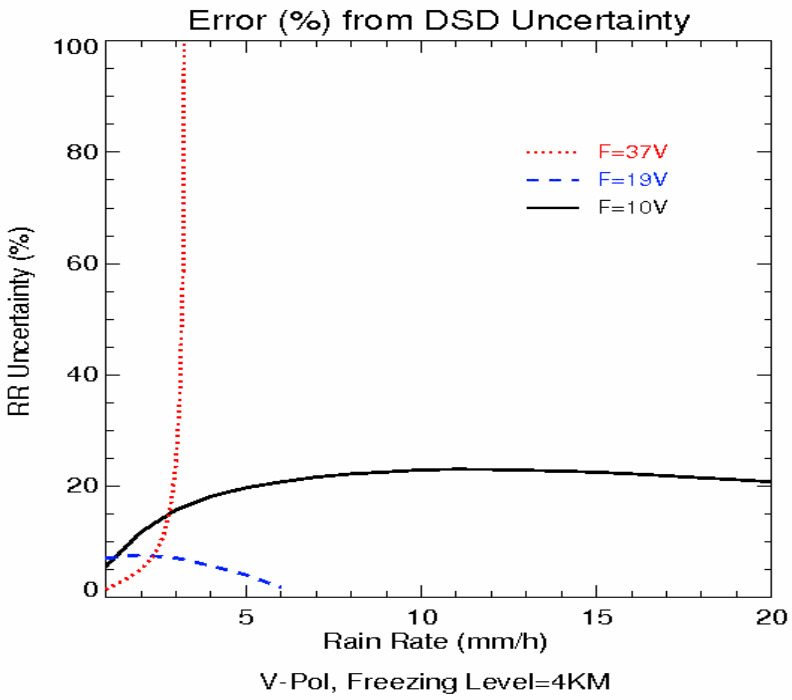

Figure 4.19 Relative percentage contribution of rain rate uncertainty driven by the DSD for the vertically polarized three channels (37, 19 and 10GHz).

c. CAL and NEΔT

For calibration uncertainty (CAL) and instrument noise (NEΔT), we simply assumed that those uncertainties are constant throughout the entire rain retrieval dynamic range. The assumed values are 2.0K for CAL and 0.5K for NEΔT, respectively. With the offset correction, however, the estimated rain rate uncertainty from CAL can be substantially reduced to near zero rain because the offset correction effectively absorbs the biases which are attributed to cold-end calibration uncertainty, including the modeling errors. The averaging absorbs the NEΔT as well.

The computed rain rate uncertainty from CAL and NEΔT is shown in Figure 4.20. The dashed-dot line denotes the rain rate uncertainty only from CAL and the dotted line

only from NEΔT. The dashed line indicates the combined effect (CAL and NEΔT). The substantially reduced rain rate uncertainty after the offset correction is represented by the solid line in the middle.

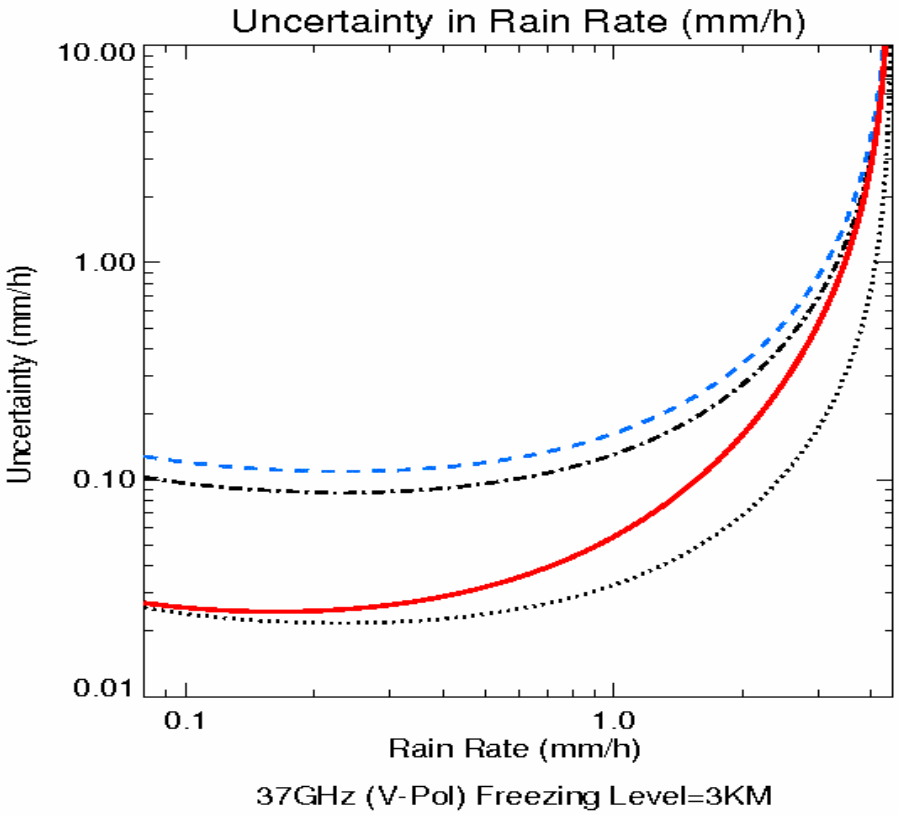

Figure 4.20 Computed rain rate uncertainty as a function of rain rate for the 37GHz, vertical channel and 3km freezing level. Only calibration uncertainty (dashed-dot line), only instrument noise (dotted line), combined (CAL+NEΔT) uncertainties (dashed line) and combined uncertainties (CAL+NEΔT) with the offset correction (solid line) were plotted together.

d. Random (sampling) errors

For the monthly rainfall retrieval (Level 3 product), a primary error source is random error driven by sampling differences. We estimated the random error by dividing the entire month into even and odd days. This method was adopted from Chang and Chiu (2001). Their result which shows the percentage random error as a function of the mean rain rate is presented in Figure 4.21. As seen in the dotted line which indicates 30% and 50% of $1/\sqrt{RR}$ respectively, the random errors are inversely proportional to the square root of the mean rain rate.

The simple procedure for computing the random errors which are based upon the partitioning the even/odd days is as follows. Since observed data can be decomposed into two parts (mean true value and errors), we let the retrieved rain rate consist of the true rain rate and the error for each case of even and odd days:

$$RR\ (E) = TRUE\ (E) + SYS\_ERROR\ (E) + RANDOM\_ERROR\ (E)$$
$$RR\ (O) = TRUE\ (O) + SYS\_ERROR\ (O) + RANDOM\_ERROR\ (O)$$

Where, E and O indicate even and odd days respectively. It was assumed that the error has two components: correlated (systematic) and uncorrelated (random). By definition, the mean true rain rate and the systematic error for both cases are identical. Therefore, the expected variance between even and odd day rain rates are expressed as

$$< (RR(e) - RR(o))^2 > = < (RAN(e) - RAN(o))^2 > = 2< (RAN(e))^2 + (RAN(o))^2 >.$$

Because we can assume random errors for both even and odd days are same, the random error is computed as

$$\sigma\ (RANDOM) = SQRT(0.5\ < (RR(e) - RR(o))^2 >).$$

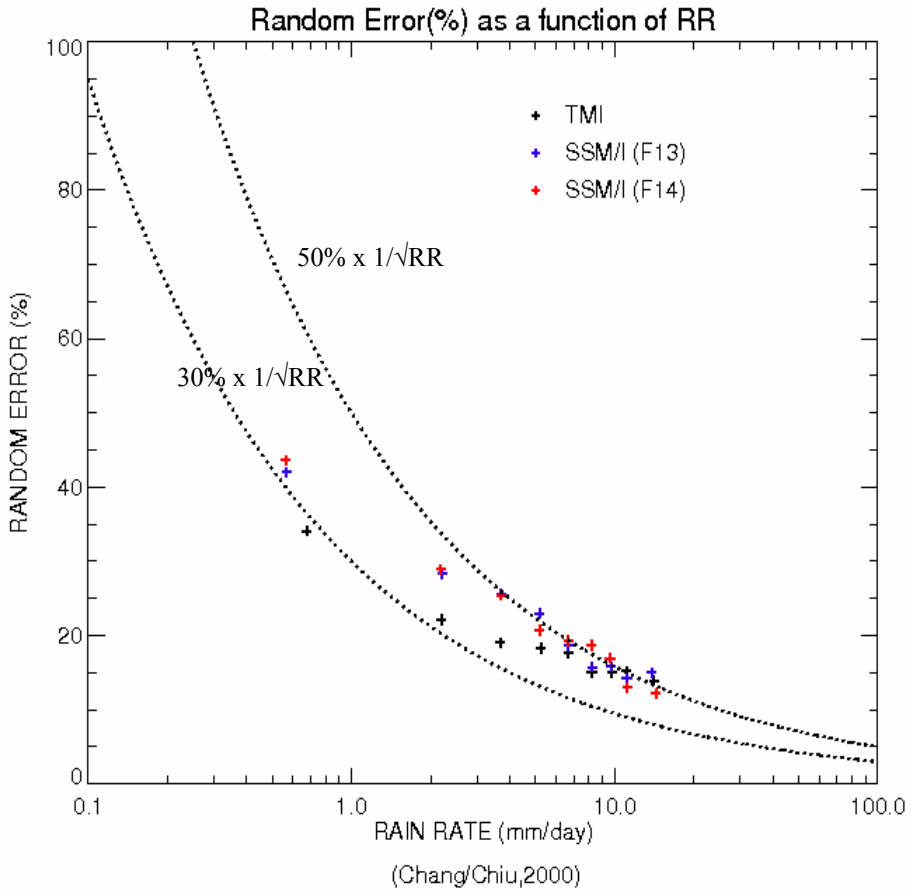

Figure 4.21 Percentage random error as a function of the mean rain rate based on Chang and Chiu (2001).

CHAPTER V

RESULTS

5.1 Evaluation of the Experimental Algorithm

The experimental algorithm was evaluated in several ways.

a. Monthly mean freezing levels

First, the retrieved mean freezing levels over 5 ° x 5° grid boxes for the TMI and the AMSR-E data (July, 2003) from the experimental algorithm were compared with the same month's official product which is based on the operational algorithm in Figure 5.1. Because rain rates are retrieved based on the computed freezing level which determines the height of a raining column, reasonable estimation of the freezing level is vital for accurate rainfall retrieval. Note that the TRMM coverage regions (40N ~ 40S) were only used for the AMSR-E data for comparison purpose. Figure 5.1 shows that the operational algorithm overestimates freezing levels in most regions. In particular, the discrepancy is much larger in the southern hemisphere. The July, 2003 values from the operational algorithm (3~5km freezing levels) are unreasonably high for the winter hemisphere.

Freezing level histograms were also plotted in Figure 5.2 to observe the characteristics of the monthly freezing level distribution using mean freezing levels based on 5° x 5° grid boxes. The comparison between TMI and AMSR-E agree well with each other for both the operational and experimental algorithms. However, the histograms of the operational algorithm (Figure 5.2a) show that the most probable freezing level for July, 2003 over the globe is about 4.8km and that low freezing levels (less than 3km) are

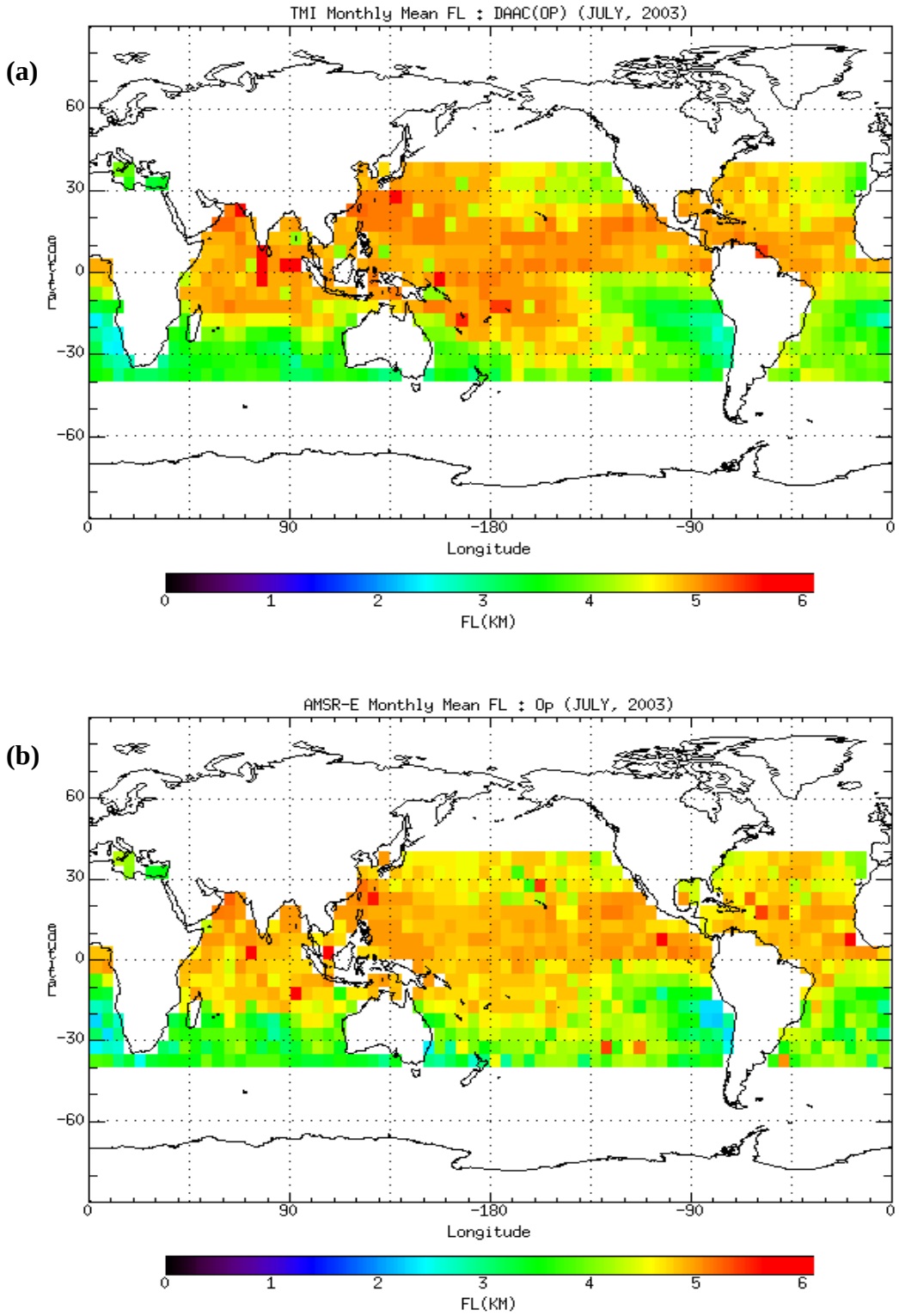

Figure 5.1 Global mean freezing level map over 5° x 5° boxes for the July 2003 data. a) Official DAAC TMI product, b) from operational algorithm (AMSR-E), c) from experimental algorithm(TMI), d) from experimental algorithm (AMSR-E).

(c)

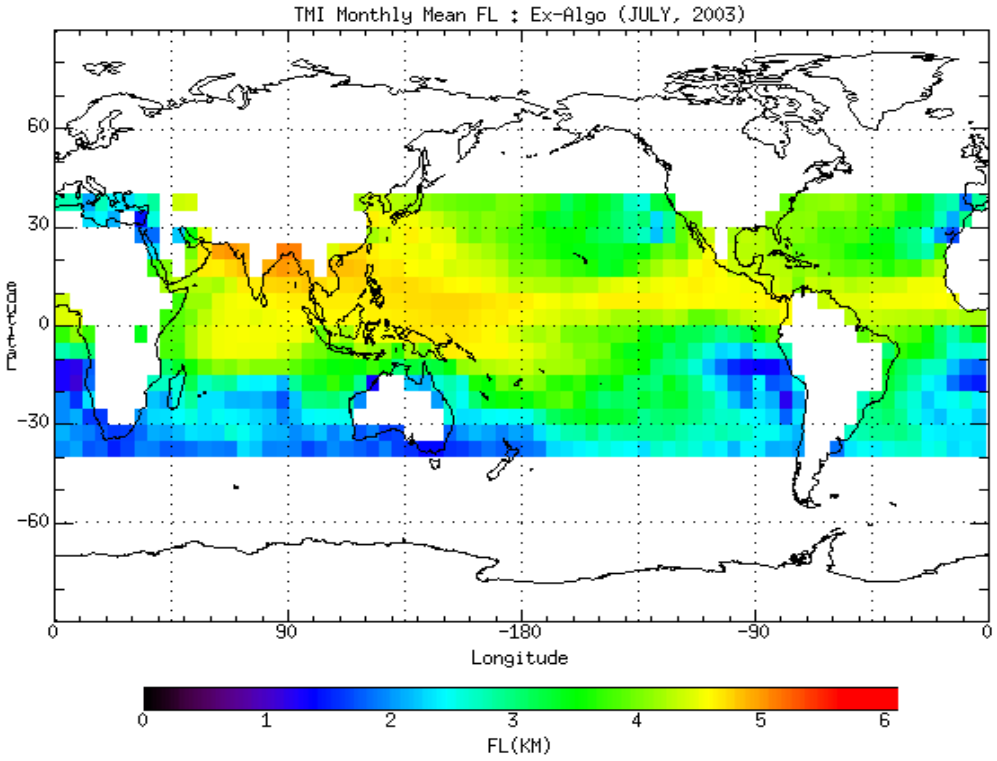

(d)

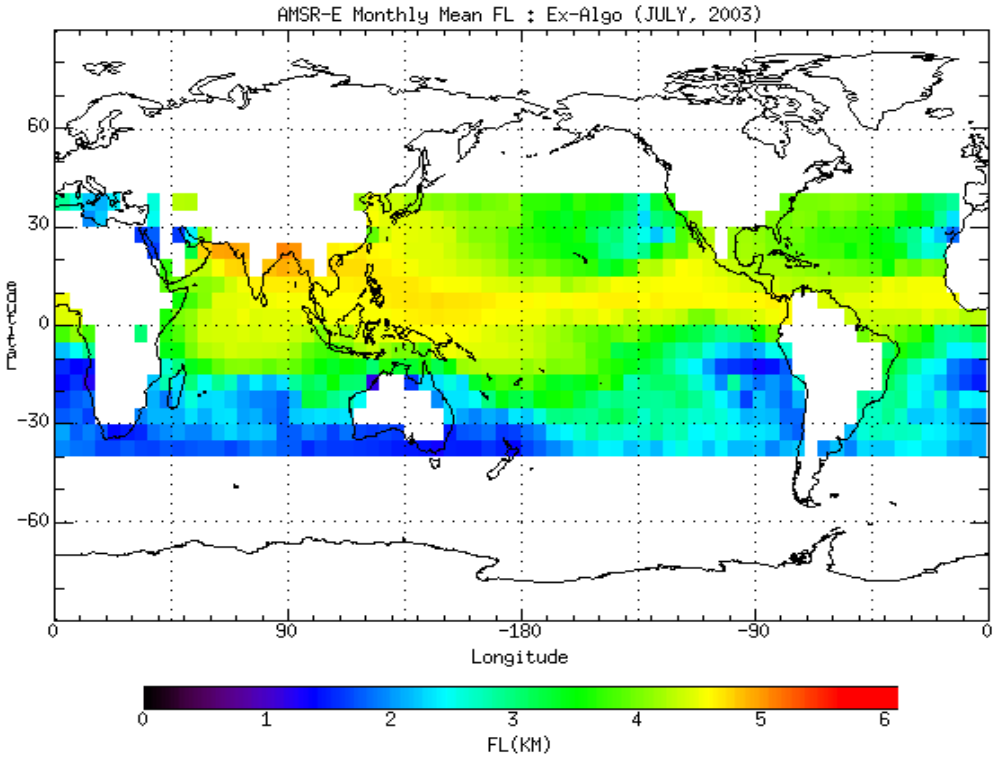

Figure 5.1, Continued.

(a)

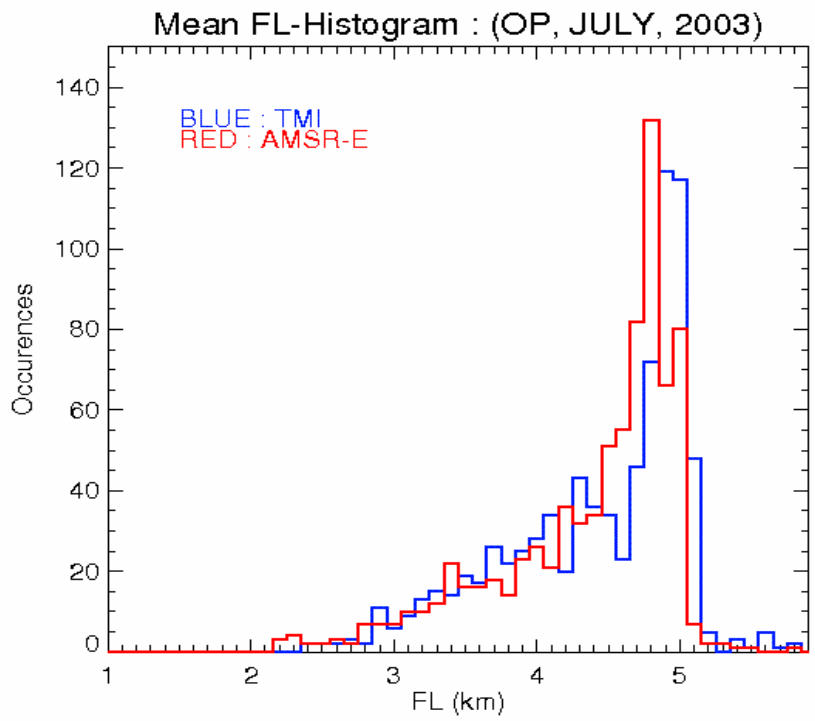

(b)

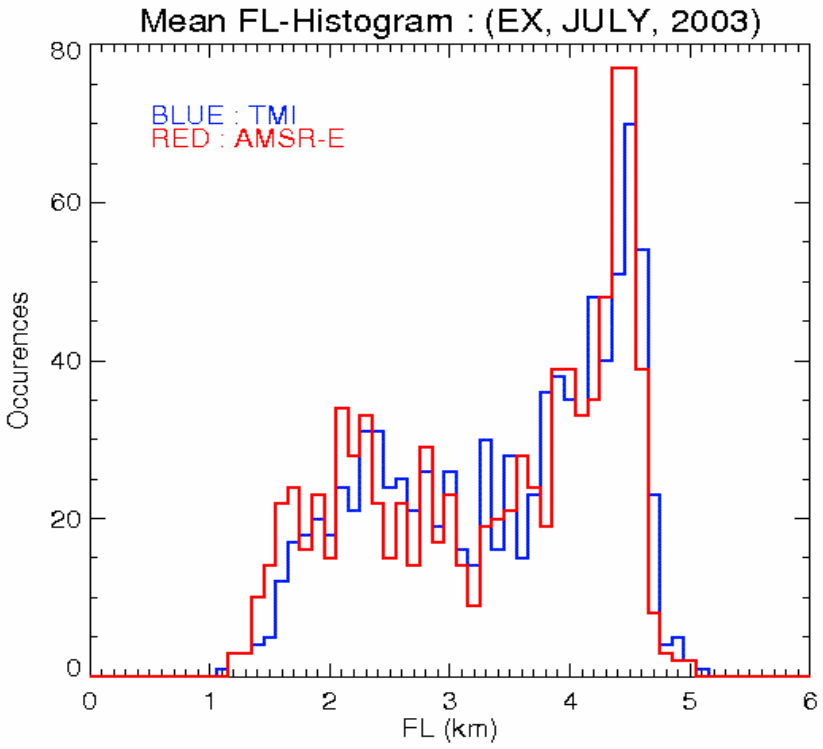

Figure 5.2 Comparison of monthly mean freezing level histograms between TMI and AMSR-E for July 2003 data. a) Operational algorithm, b) experimental algorithm.

rare. On the other hand, the histograms from the experimental algorithm show a bimodal distribution: one peak is located in around 2.2km and the other peak is around 4.5km (Figure 5.2b).

To examine the co-variability of the freezing levels between TMI and AMSR-E data over 5 ° x 5°grid boxes, scatter-plots were generated in Figures 5.3a-d. While the freezing levels between TMI and AMSR-E data are in good agreement for both algorithms (Figures 5.3a and 5.3b), the experimental algorithm gives us more consistent results. But, comparison between the two algorithms shows that the official product based on the operational algorithm has much higher freezing level values than those of the experimental algorithm (Figures 5.3c and 5.3d): by about 30 percent at low freezing levels (2~3.5km) and 10~20 percent at high freezing levels (4~6km).

This overestimation of the freezing level is mainly attributed to the shortcoming of the operational algorithm that uses only one freezing level over 5 ° x 5° grid box for the entire month. On the other hand, the experimental algorithm handles the temporal and spatial variability of freezing levels properly due to its pixel-by-pixel retrieval scheme and in turn yields more reasonable estimates.

b. Monthly mean rain rates

Second, the monthly rain totals computed from the experimental algorithm were compared with those of the official products. Figures 5.4a and 5.4b show monthly rain totals (expressed as mm/day) from the official products for the July 2003 TMI data: TMI+IR composite image (Figures 5.4a, from http://trmm.gsfc.nasa.gov) and DAAC Level 3 product which is based upon the operational algorithm (Figure 5.4b).

(a)

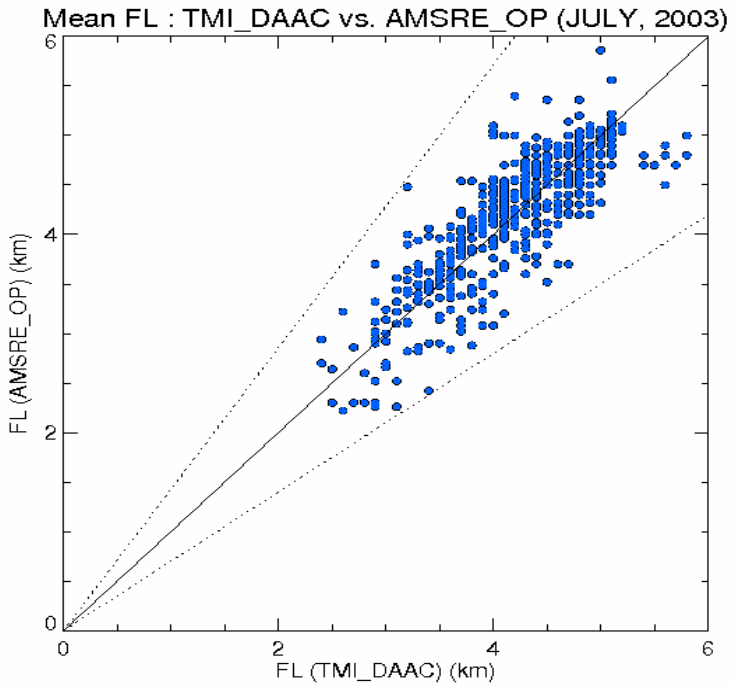

(b)

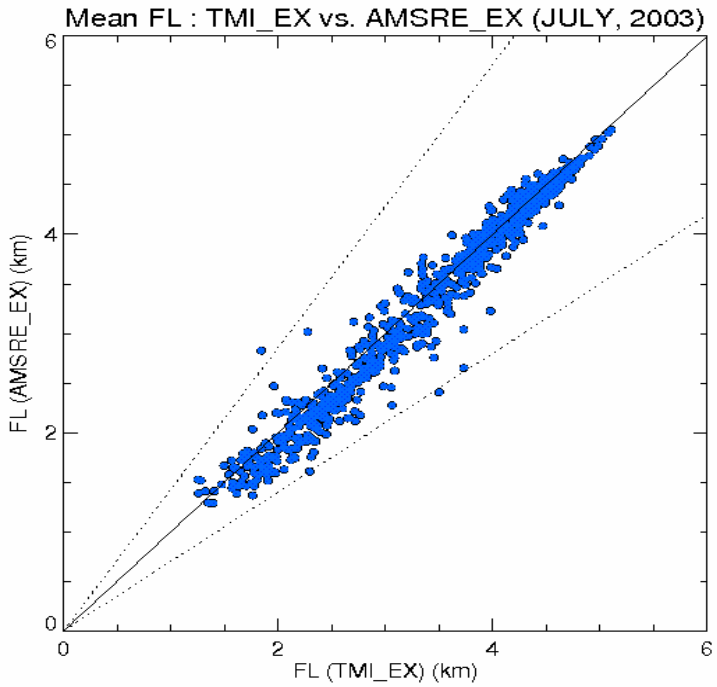

Figure 5.3 Scatter-plot of mean freezing levels based on 5°x5° grid boxes over the global ocean using July 2003 data. a) TMI vs. AMSR-E (operational algorithm), b) TMI vs. AMSR-E (experimental algorithm), c) TMI DAAC product vs. TMI (experimental algorithm), d) TMI DAAC product vs. AMSR-E (experimental algorithm).

(c)

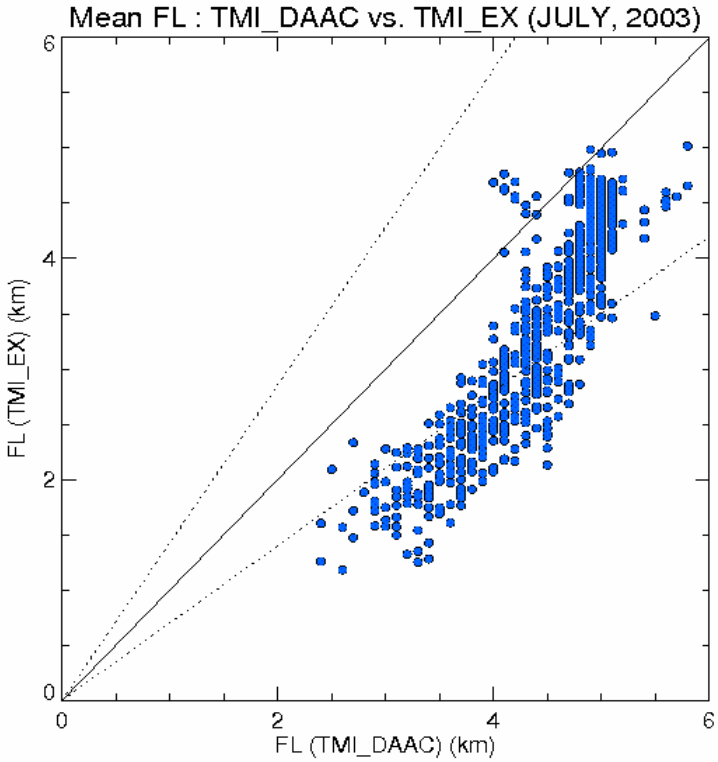

(d)

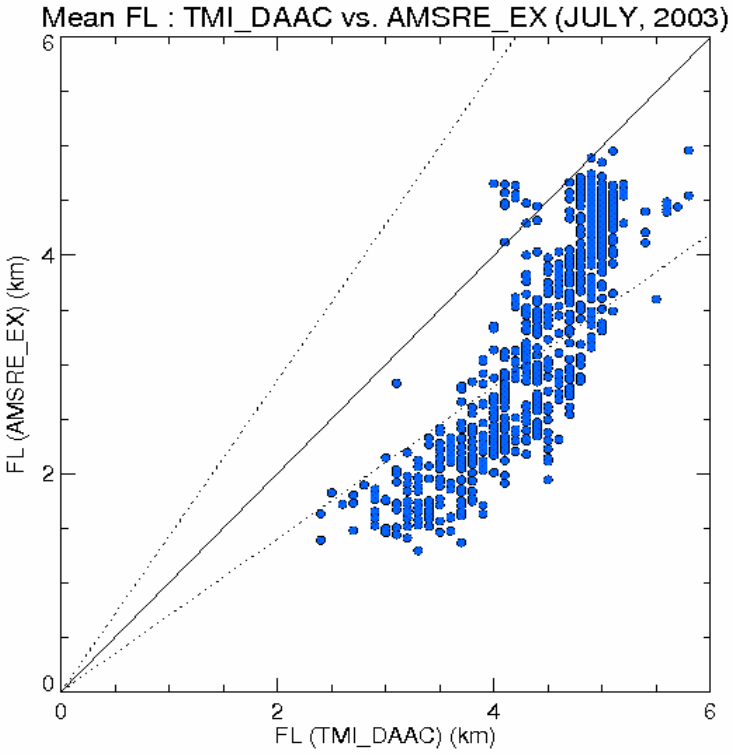

Figure 5.3, Continued.

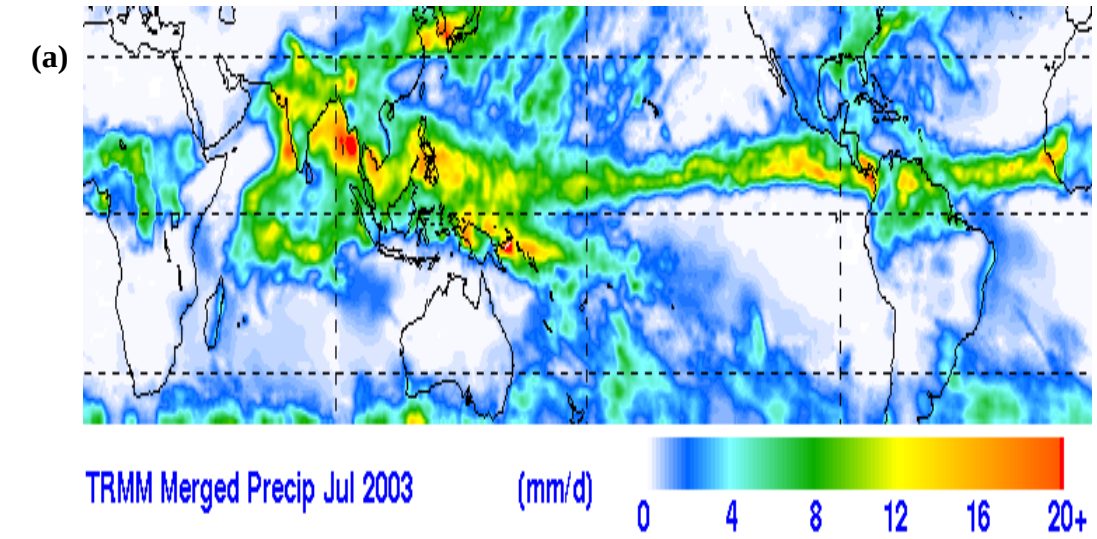

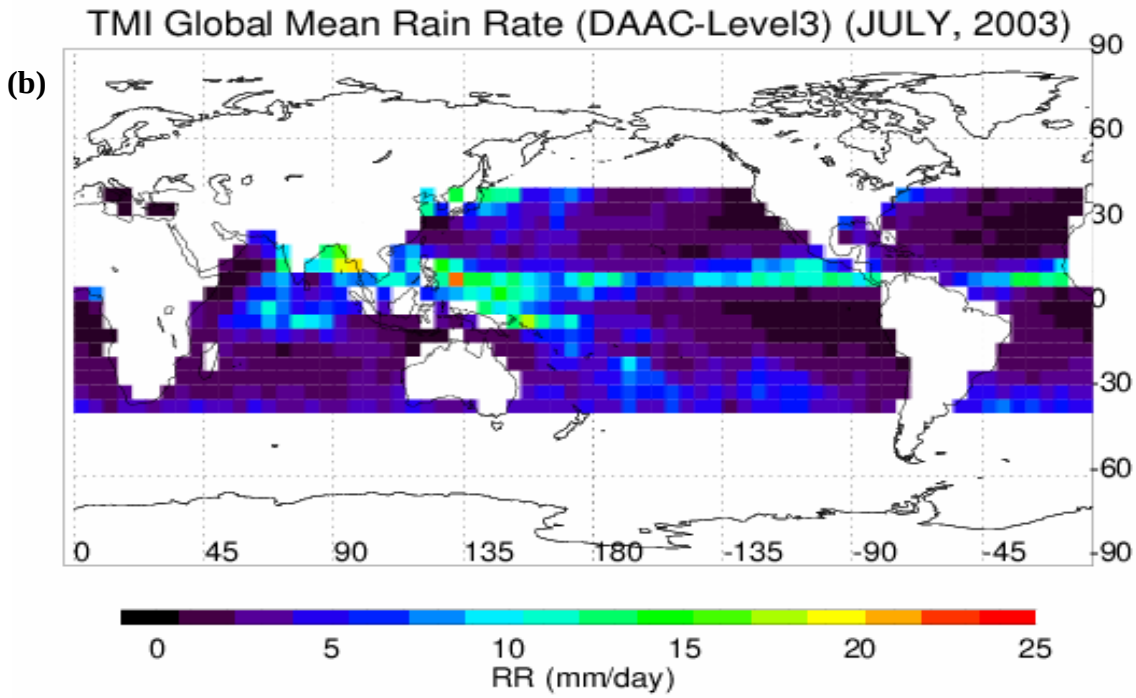

Figure 5.4 Global monthly rain totals over 5° x 5° boxes for the July 2003 data. a) TMI+IR composite (scattering-based), b) operational algorithm (TMI), c) experimental algorithm (TMI), d) experimental algorithm (AMSR-E).

(c)

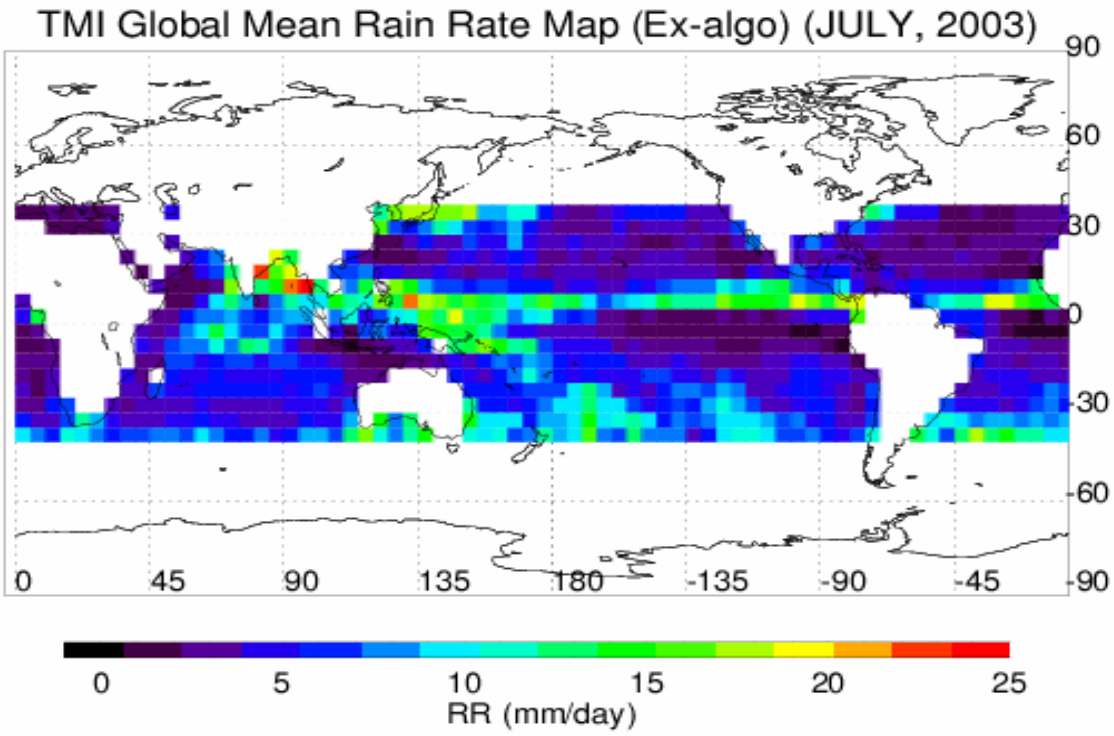

(d)

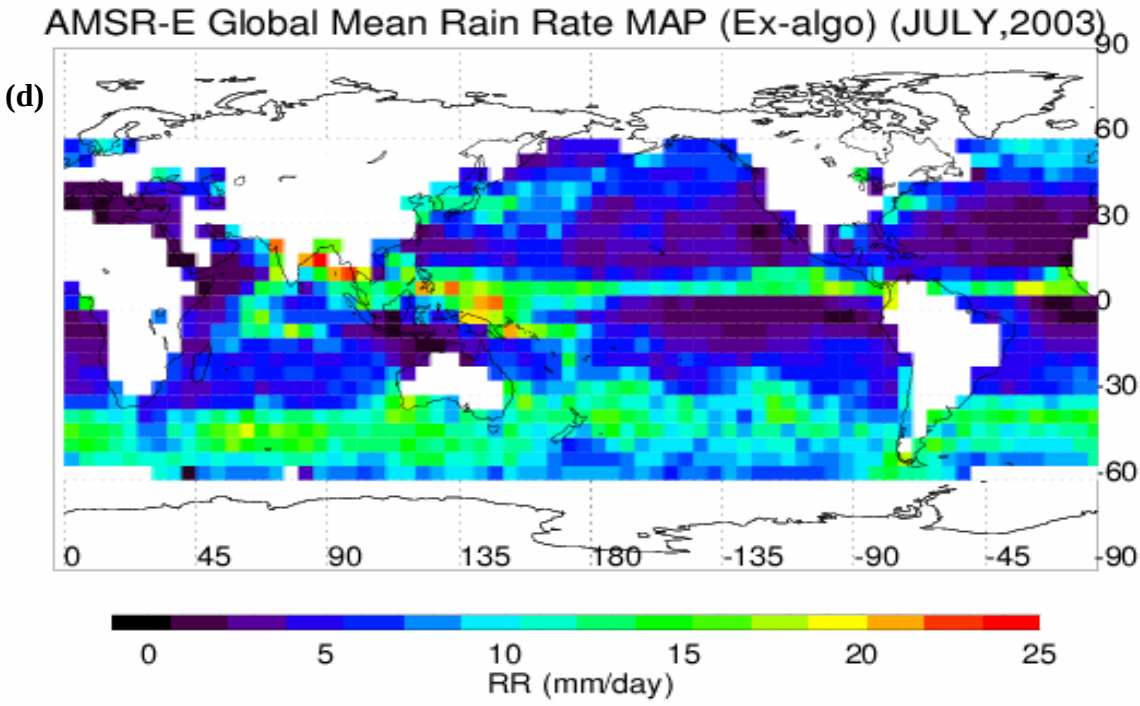

Figure 5.4, Continued.

respectively. The results from the experimental algorithm using TMI and AMSR-E data are shown in Figures 5.4c and 5.4d respectively.

The monthly rain rates from the operational algorithm which has higher freezing levels are lower than those of the experimental algorithm since rain rate is inversely related with freezing level. However, the general features of the mean rainfall distribution between the two algorithms are consistent. The monthly mean rain rates from the TMI and AMSR-E data based upon the experimental algorithm (Figures 5.4c and 5.4d) show reasonable consistency over the TRMM coverage (40N~40S) as well. However, compared with the variability of the freezing levels (Figure 5.3b), the fluctuations of rain rates are much larger.

Overall, the retrieved rain rates based on the experimental algorithm (Figures 5.4c and 5.4d) have much higher values than those of the operational algorithm (Figure 5.4b). In addition, a much larger proportion of higher rain rates is observed in AMSR-E compared to TMI. The notable difference of the monthly rain totals between the operational and the experimental algorithm is the discrepancy of the estimated rain rates at the high latitudes of the southern hemisphere (winter hemisphere in July). Besides, the comparison of the monthly rain totals between the AMSR-E and TMI from the experimental algorithm shows biases especially at the winter hemisphere (30S~40S) which are indicated by blue in Figure 5.5.

c. Mean rain rate bias between AMSR-E and TMI

To investigate AMSR-E mean rain rate discrepancy with that of TMI, which is mainly observed in the winter hemisphere, we first carried out a credibility check to

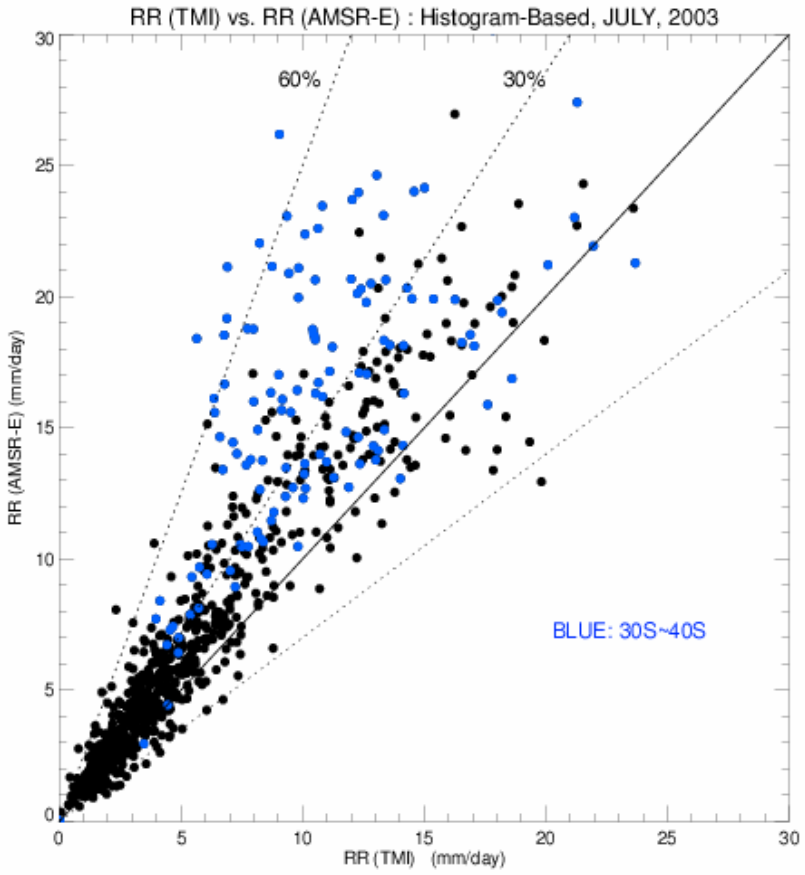

Figure 5.5 Scatter-plot of monthly mean rain rates between TMI and AMSR-E over 5°x 5° boxes for July 2003 data based on the experimental algorithm.

assure the performance of the experimental algorithm. The monthly rain totals computed by a simple adding method (hereafter SUM RAIN) which sums all the pixel-by-pixel rain rates over 5 ° x 5° grid box were compared with another output (hereafter HIST RAIN) which was calculated from rain rate histogram. For SUM RAIN, two different conditions were applied: one uses the same condition as HIST RAIN which uses only reliable

samples (pixels) for freezing level retrieval (0.5km < FL < 6.0km) and the other allows a more general condition which includes all the erroneous samples which are problematic for the freezing level retrieval due to too little rain (hereafter NO-FL samples). It is assumed that more reasonable monthly rain totals can be achieved in the second case which includes all the problematic cases for the freezing level retrievals because most of those cases are assumed to be non-raining cases. If those of apparently erroneous samples are ignored, many non-raining samples are excluded in computing the average rain rate in some regions, especially in the winter hemisphere where air is very dry compared to the tropics. This results in spurious increase in the mean rain rate.

Under the same constraint which only utilizes reliable samples for freezing level retrieval, SUM RAIN and HIST RAIN for both TMI and AMSR-E data show very good agreement (Figure 5.6). However, when the all NO-FL samples were included, HIST RAIN is much higher than SUM RAIN (up to 50%) and there is a geographical dependency (Figures 5.7a and 5.7b): the tropics (10N~10S, red circles) shows much smaller discrepancies than the winter hemisphere (25S-40S, blue circles). The greater occurrence of the NO-FL samples for the freezing level retrieval in the winter hemisphere where atmosphere is very dry is mainly responsible for these errors, resulting in the larger bias between HIST RAIN and SUM RAIN.

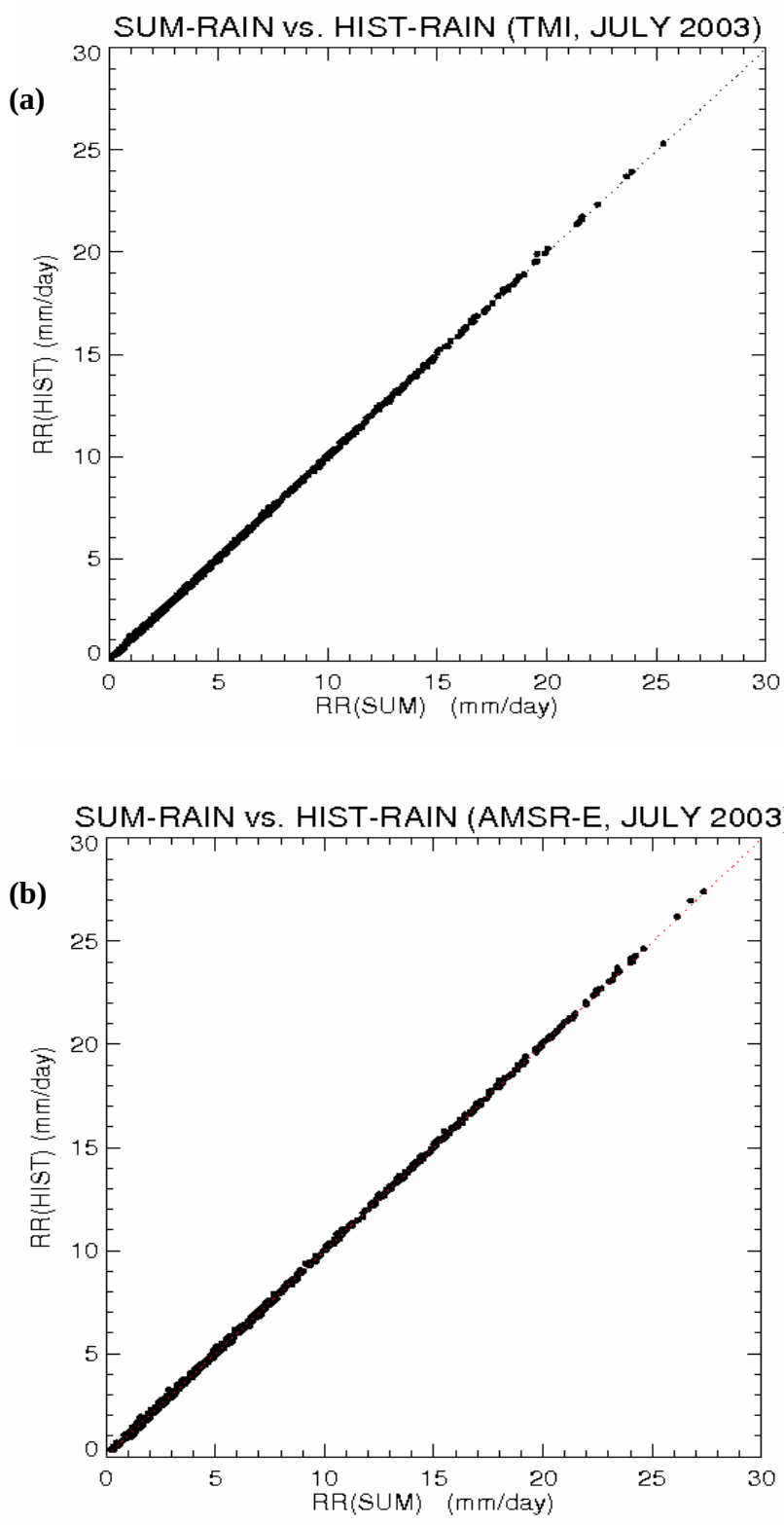

Figure 5.6 Comparison of monthly mean rain rates under the same conditions (only for reliable cases for the freezing level retrieval: SUM RAIN vs. HIST RAIN. a) TMI, b) AMSR-E.

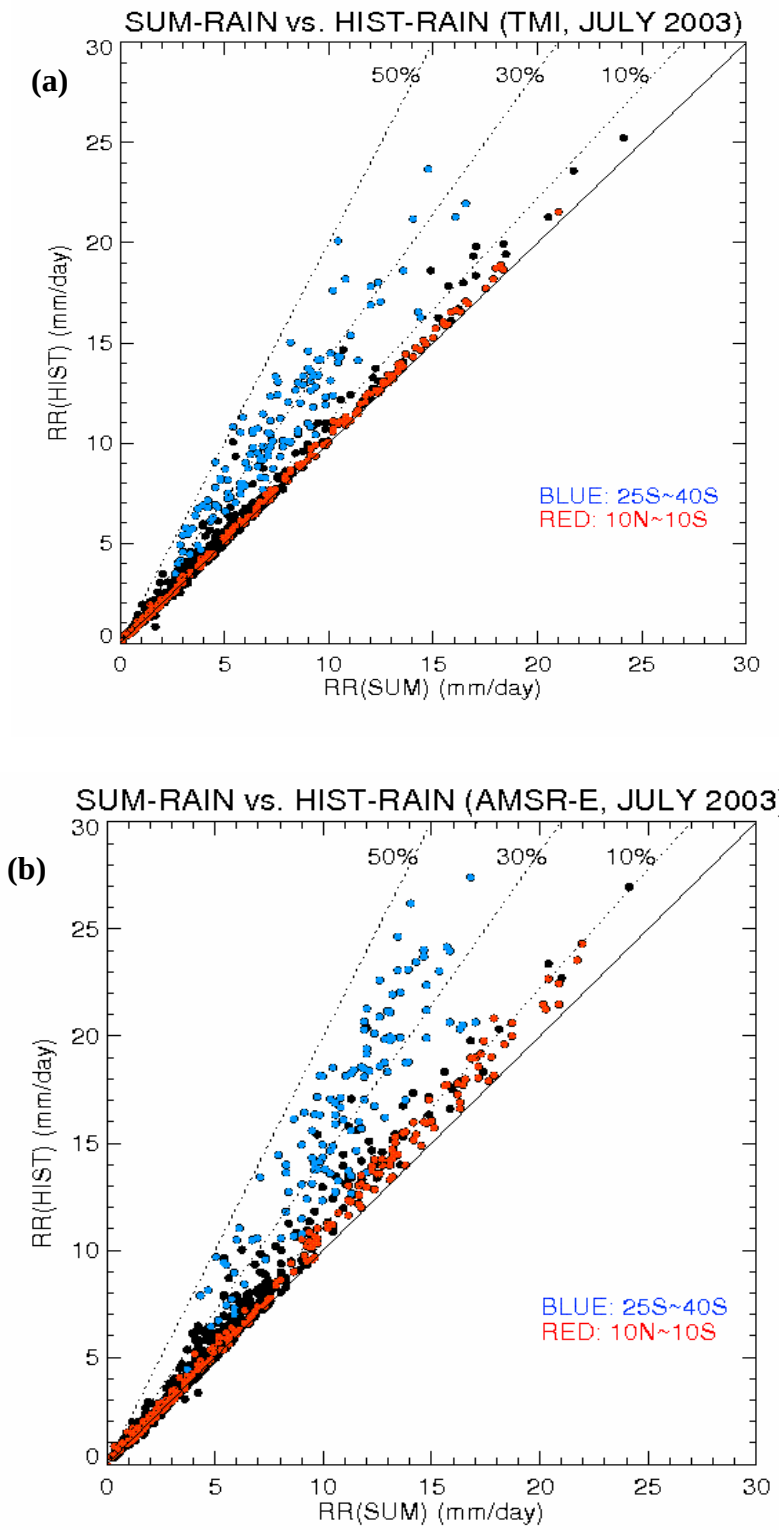

Figure 5.7 Comparison of monthly mean rain rates between SUM RAIN and HIST RAIN under the different conditions (SUM RAIN: for all samples including erroneous pixels for the freezing level retrieval, HIST RAIN: only for reliable cases for the freezing level retrieval. a) TMI, b) AMSR-E.

Second, computed rain rate offsets of TMI and AMSR-E data were examined. Figure 5.8a shows comparison of the weighted average offset over 5 ° x 5° grid box between the TMI and AMSR-E data (July, 2003). It clearly shows that the AMSR-E has higher offsets than the TMI. In particular, much larger values (about 70% higher) are observed in the offsets of the AMSR-E over the winter hemisphere (25S ~40S).

The offsets of all six channels were also examined in Figures 5.8b-g. Individual offsets from each channel show different patterns. For example, the horizontally polarized channels show more discrepancies between TMI and AMSR-E than the vertically polarized channels. In particular, the AMSR-E 37GHz channels have considerably higher offsets than the same channels of TMI. In addition, the 37GHz horizontal channels show strong discrepancy in the winter hemisphere (blue circles).

It is assumed that these much higher offsets of the AMSR-E channels are closely related with the rain rate biases between TMI and AMSR-E observed mostly over the winter hemisphere. It should also be noted that very low freezing levels over the winter hemisphere lead to a drastic increase of rainfall retrieval uncertainty due to the limitation of reasonable computation of a radiative transfer within a very limited raining column. In addition, since determination of reasonable offsets from rain rate histograms has much larger uncertainties in the winter hemisphere, AMSR-E's larger data uncertainty is less effective for the offset correction than TMI.

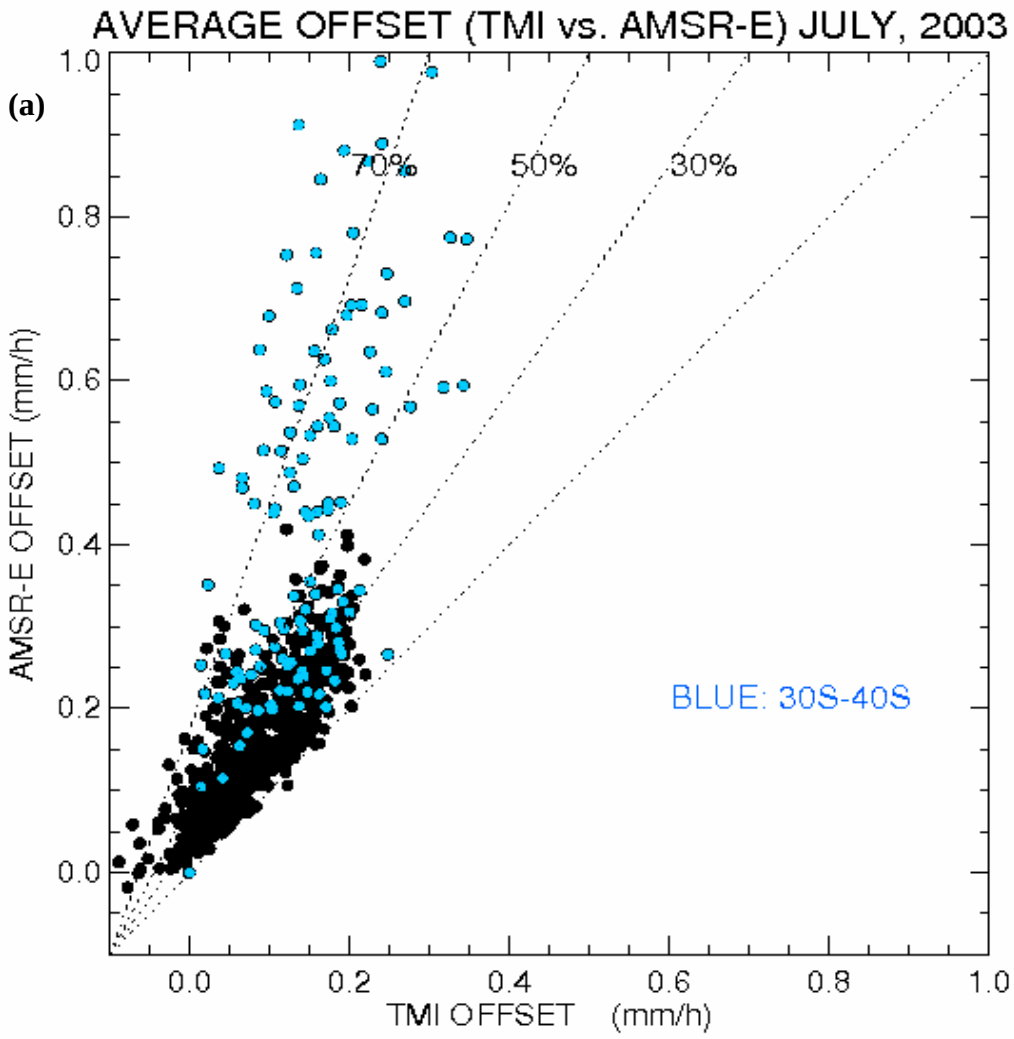

Figure 5.8 Scatter-plot of the computed offsets between TMI and AMSR-E for July 2003 data. a) Weighted average offsets, b) 10v offsets, c) 10h offsets, d) 19v (18v) offsets, e) 19h (18h) offsets, f) 37v offsets, g) 37h offsets.

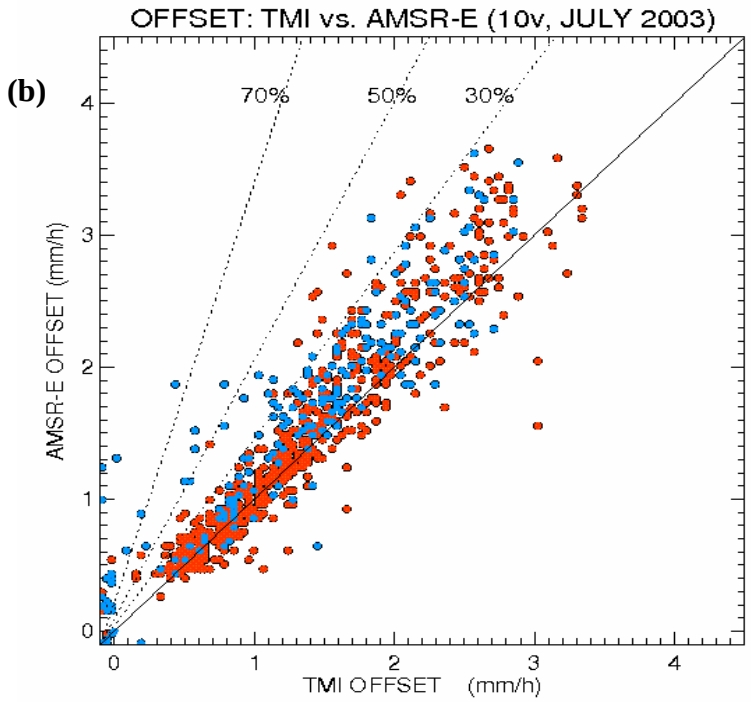

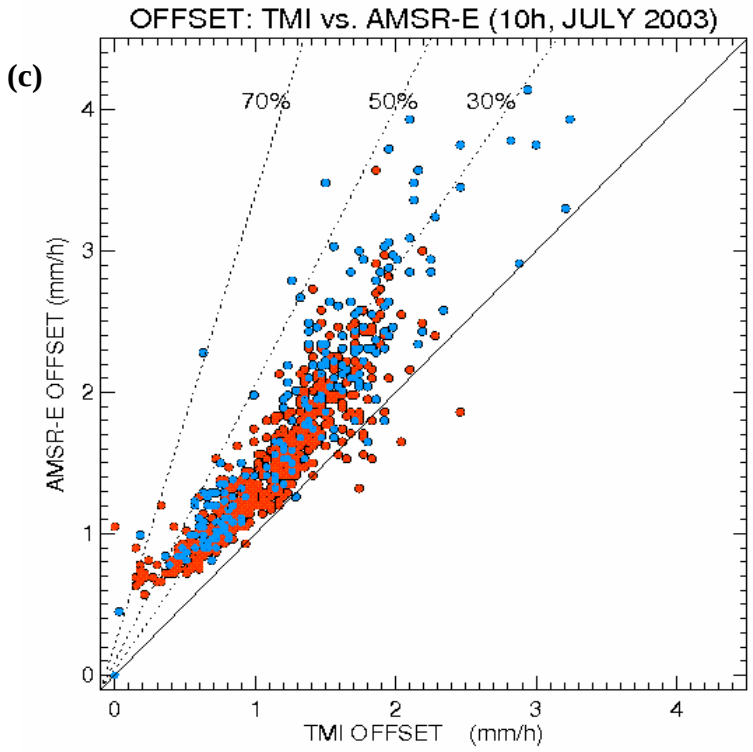

Figure 5.8, Continued.

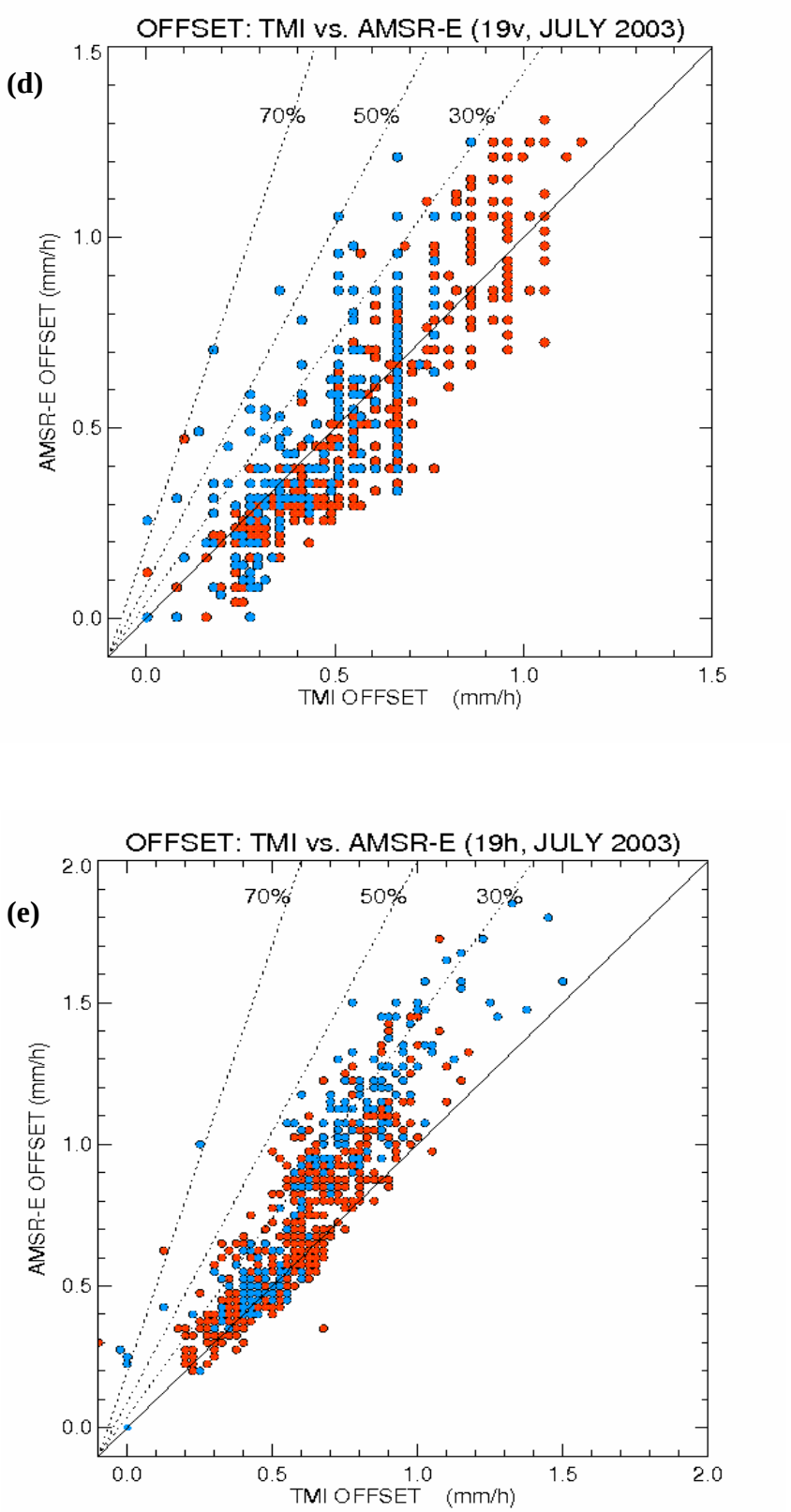

Figure 5.8, Continued.

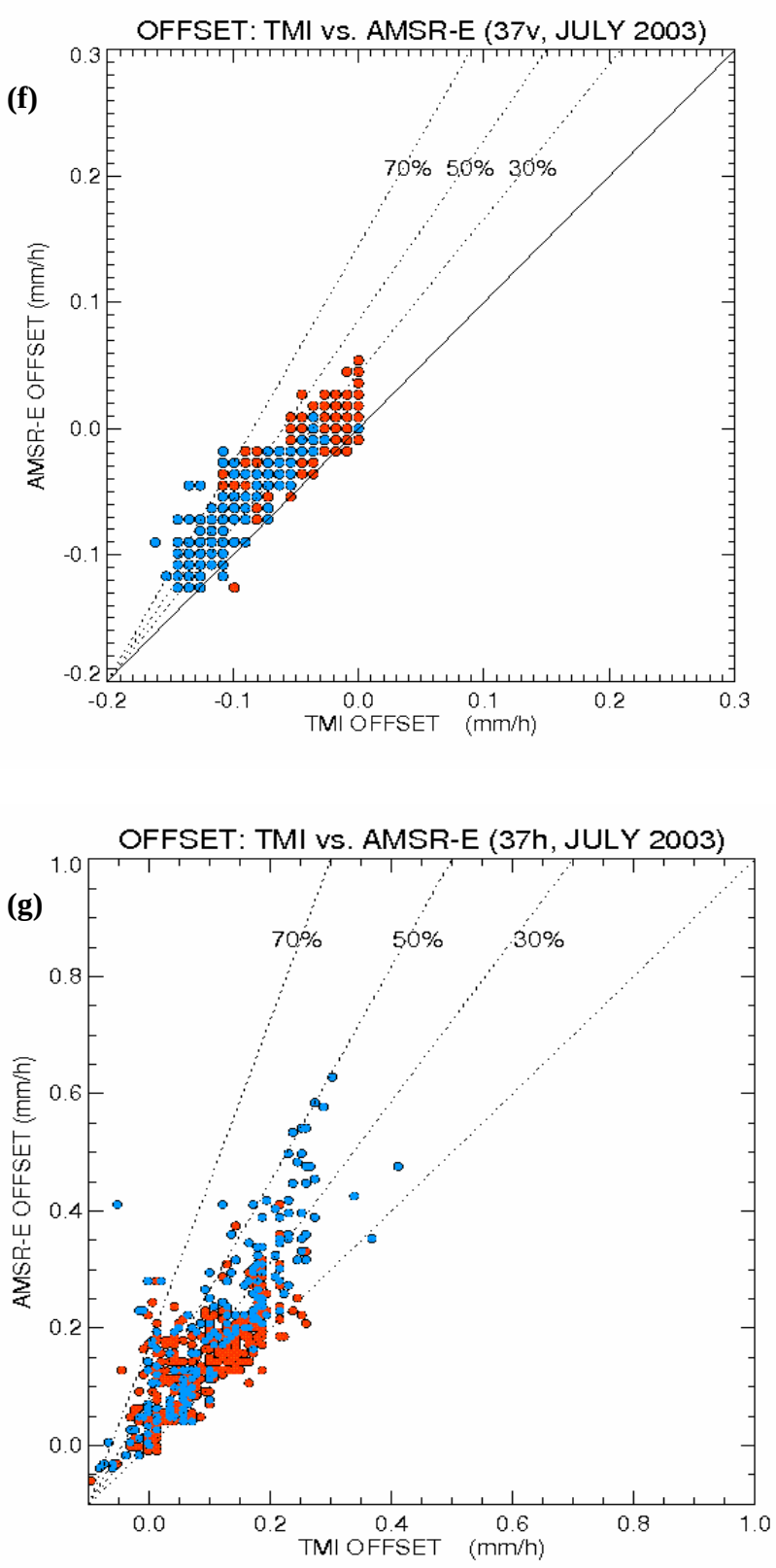

Figure 5.8, Continued.

The offset biases driven by the calibration uncertainty of the AMSR-E channels were examined by partitioning data into Ascending/Descending cases. Figures 5.9a-f show the comparison of mean offset values between ascending and descending samples over 5° x 5° grid boxes for July 2003 AMSR-E data. For comparison, data over the winter hemisphere are indicated by blue. In principle, there is no systematic difference between ascending and descending cases of well-calibrated data. But, some channels (10h, 18v, 18h and 37h) clearly show the biases which are primarily attributed to the calibration problem of AMSR-E.

The impact of the calibration uncertainties of AMSR-E data on retrieved freezing levels and rain rates is presented in Figures 5.10 and 5.11. While results are consistent each other when data are divided into even and odd days (Figures 5.10a and 5.11a), retrieved freezing levels (Figure 5.10b) show some biases at low freezing levels (from about 1.5km to 3km) and estimated mean rain rates (Figure 5.11b) have significant impact (over 30%) for partitioning ascending and descending samples. As a consequence, it is assumed that these offset biases associated with AMSR-E's higher calibration uncertainty lead to the mean rain rate biases between TMI and AMSR-E.

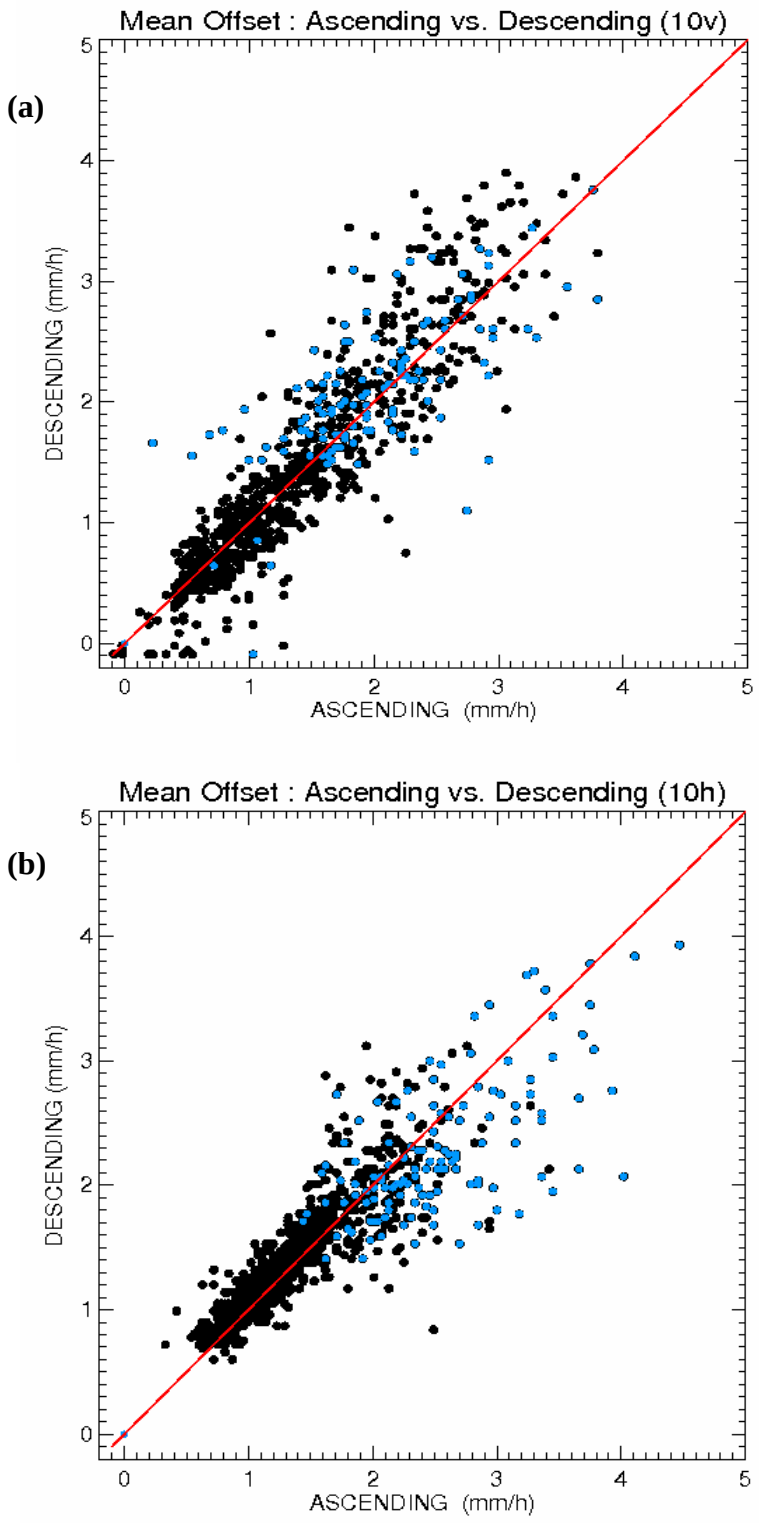

Figure 5.9 Scatter-plot of the computed offsets between Ascending and Descending for July 2003 AMSR-E data. a) 10v offsets, b) 10h offsets, c) 18v offsets, d) 18h offsets, e) 37v offsets, f) 37h offsets.

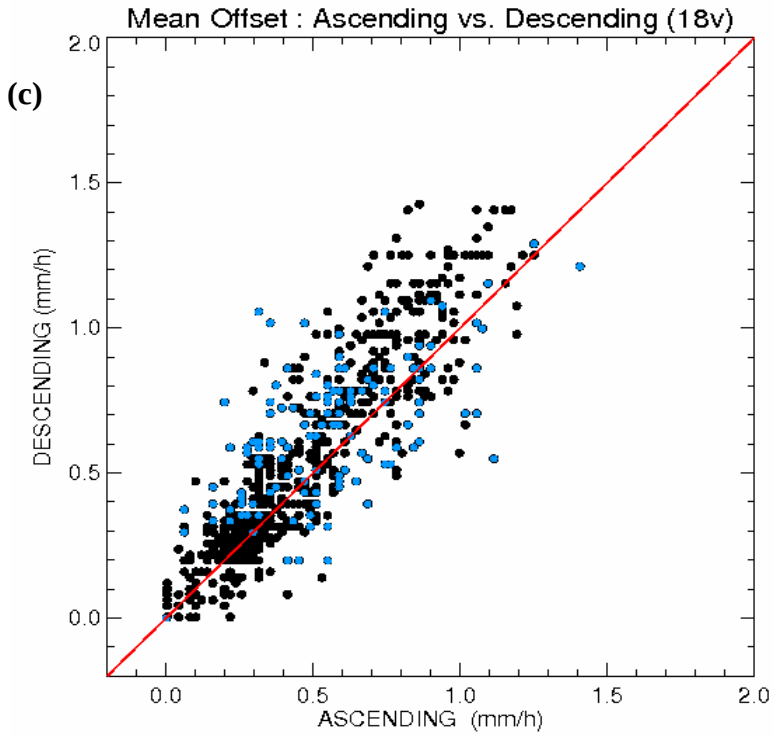

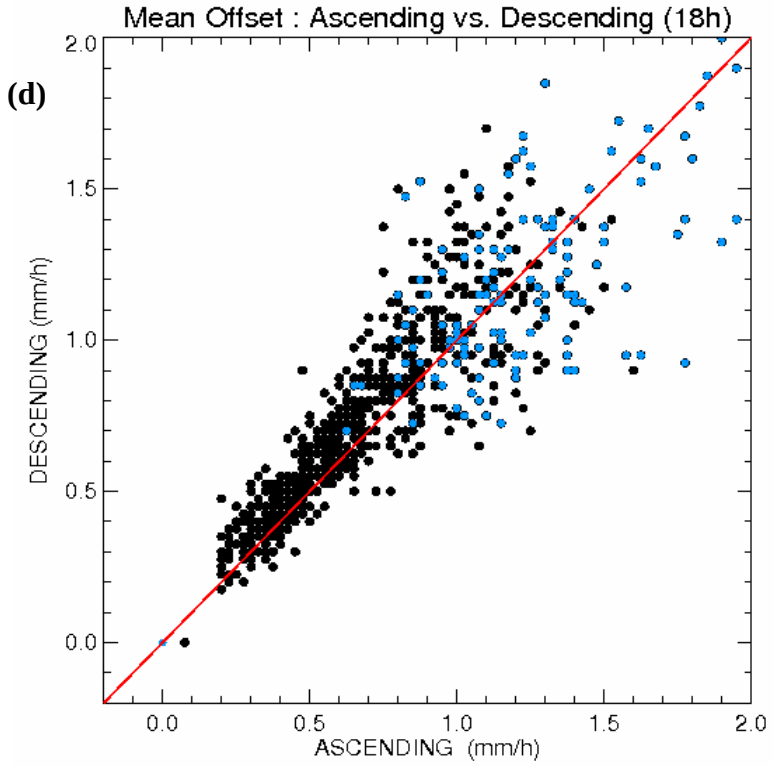

Figure 5.9, Continued.

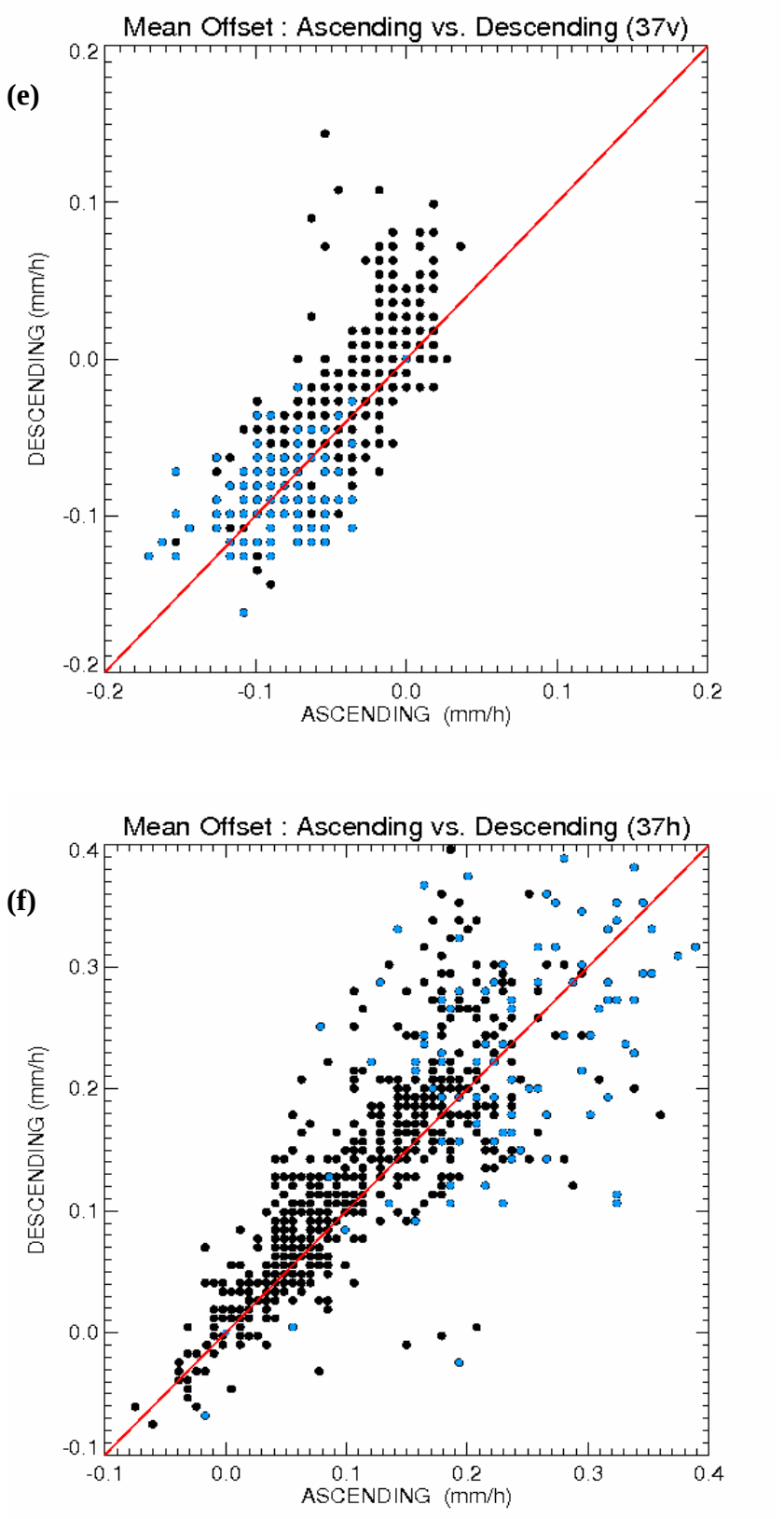

Figure 5.9, Continued.

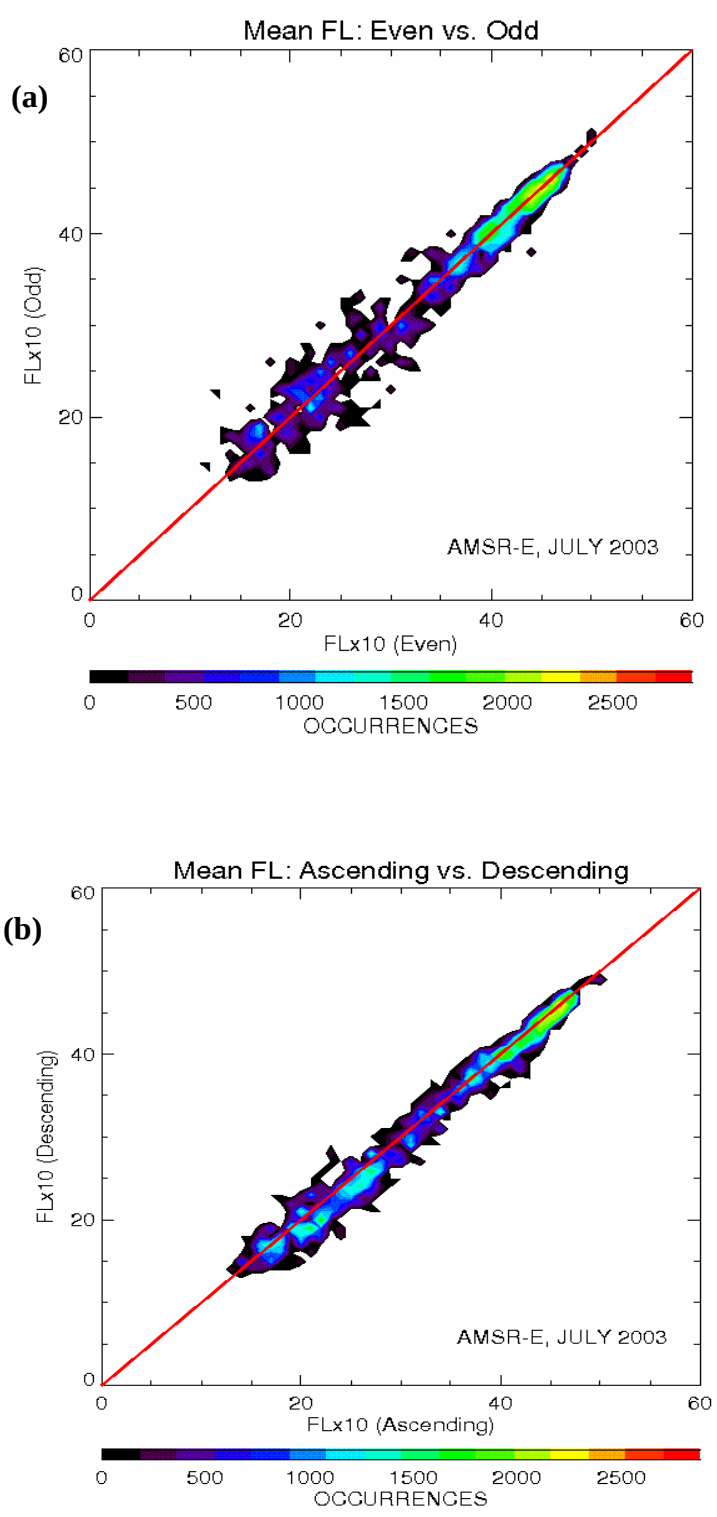

Figure 5.10 Contour scatter-plot of the mean freezing levels based on 5°x5° grid boxes for July 2003 AMSR-E data: a) Between Even and Odd days, b) Between Ascending and Descending cases.

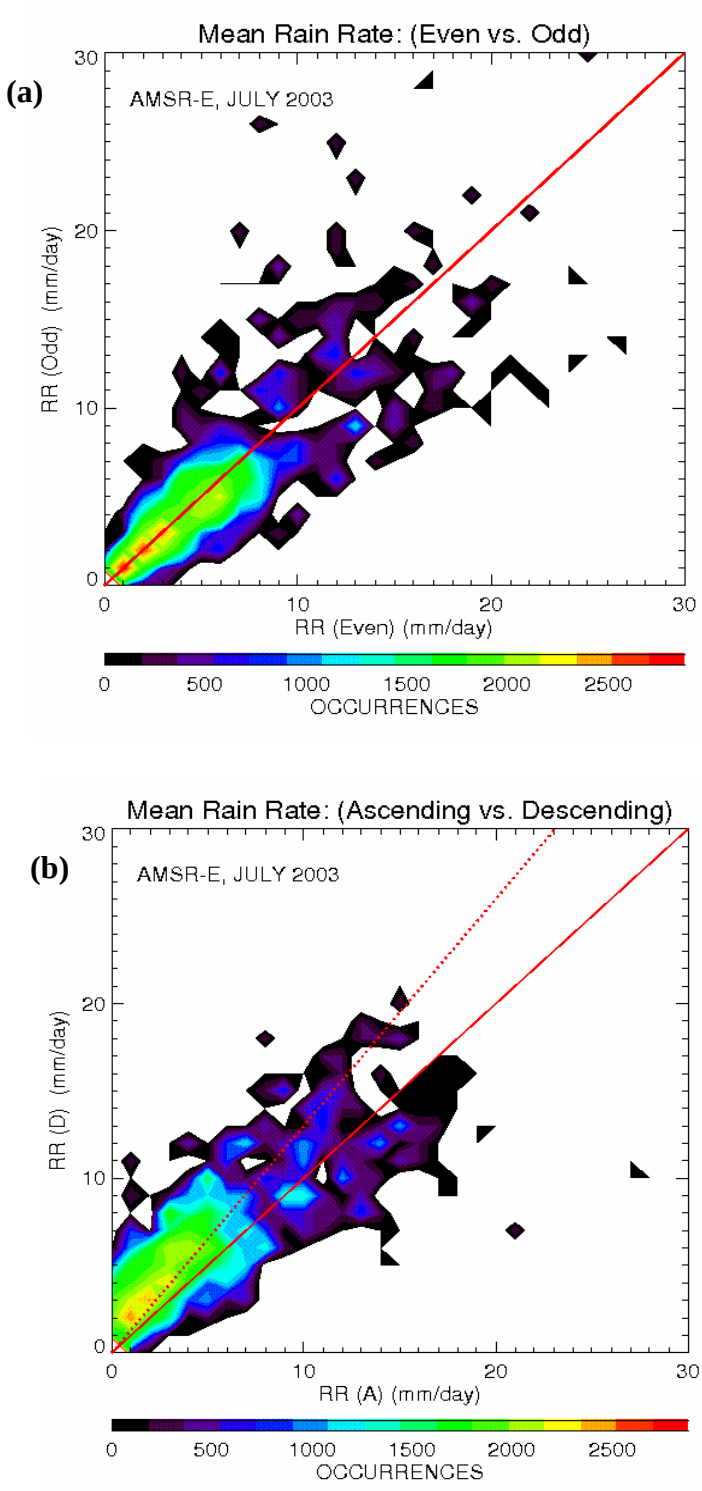

Figure 5.11 Contour scatter-plot of the mean rain rates based on 5°x5° grid boxes for July 2003 AMSR-E data: a) Between Even and Odd days, b) Between Ascending and Descending cases.

d. Heavy rainfall over the winter hemisphere

Next, we examined the typical granule data containing raining events for both TMI and AMSR to validate the results from the experimental algorithm which show higher rain rates over the winter hemisphere than those of the operational algorithm even if very low freezing levels (low raining columns) are observed at these regions. Figure 5.12a shows the intense ocean rainfall captured by the TMI vertically polarized 10GHz channel over the winter hemisphere (24-40S, 150-180W, July 3, 2003: 09Z). About two hours later (July 3, 2003: 11Z), the same raining storm was also measured by AMSR-E (Figure 5.13a). The retrieved rain rates from the 10GHz channels are plotted in Figures 5.12b and 5.13b respectively. In addition, the weighted average rain rates for the co-located area A for TMI and AMSR-E were also shown in Figures 5.12c and 5.13c. Orange spaces which can be observed in Figures 5.12 and 5.13 indicate the very dry area so that retrieval of rain rate is problematic due to the problem of the freezing level retrieval. They clearly show that very heavy rain events (up to about 15mm/h) occur in the winter hemisphere where raining clouds' tops are relatively low compared to the tropics.

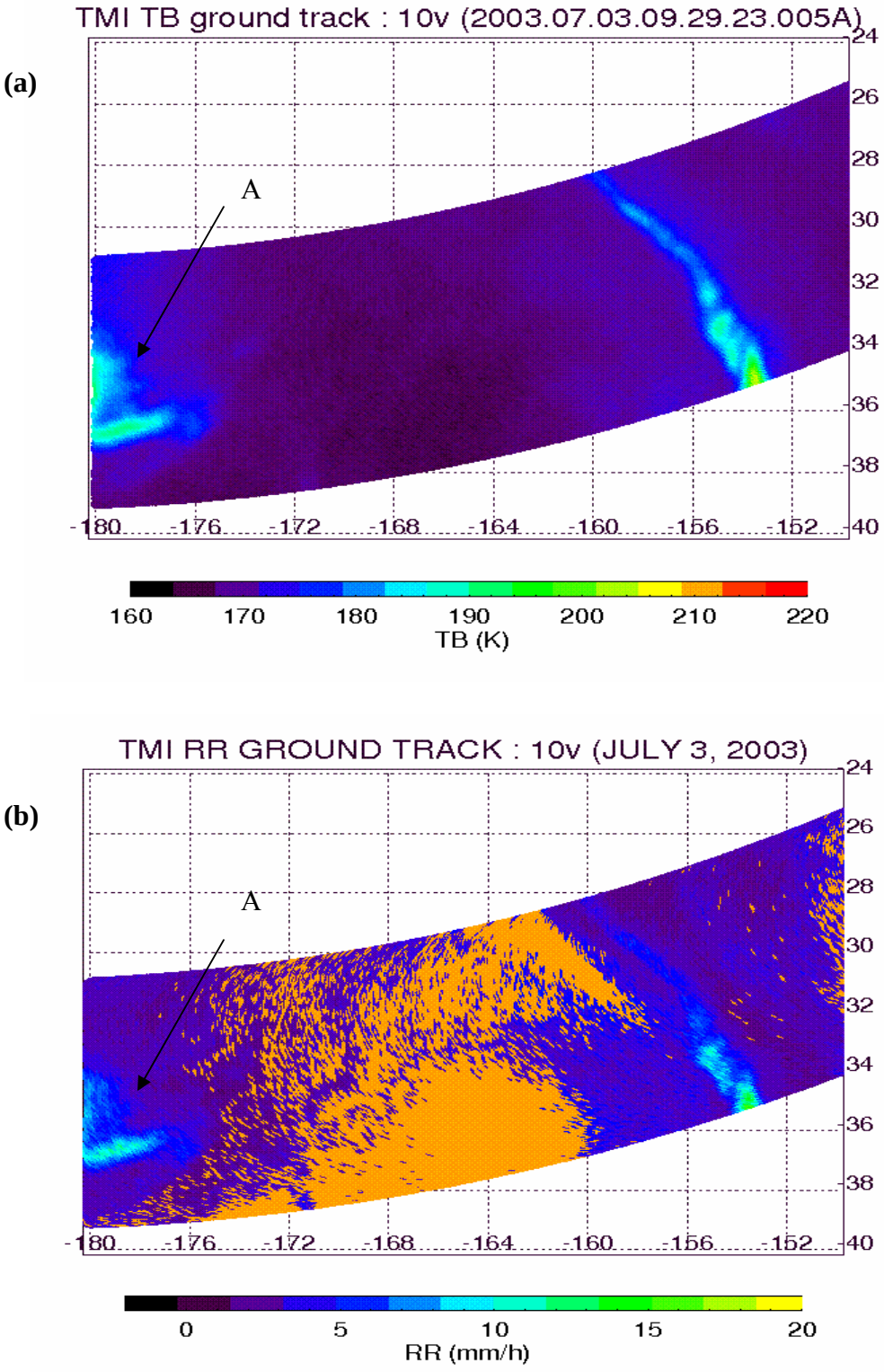

Figure 5.12 Winter hemisphere storm track observed by TMI, July 3, 2003:09Z, 25-40S, 150-180W). a) Brightness temperature of 10GHz, vertical channel, b) Retrieved rain rates of 10GHz, vertical channel, c) Weighted average rain rates over area A. Orange color represents very dry area.

(c)

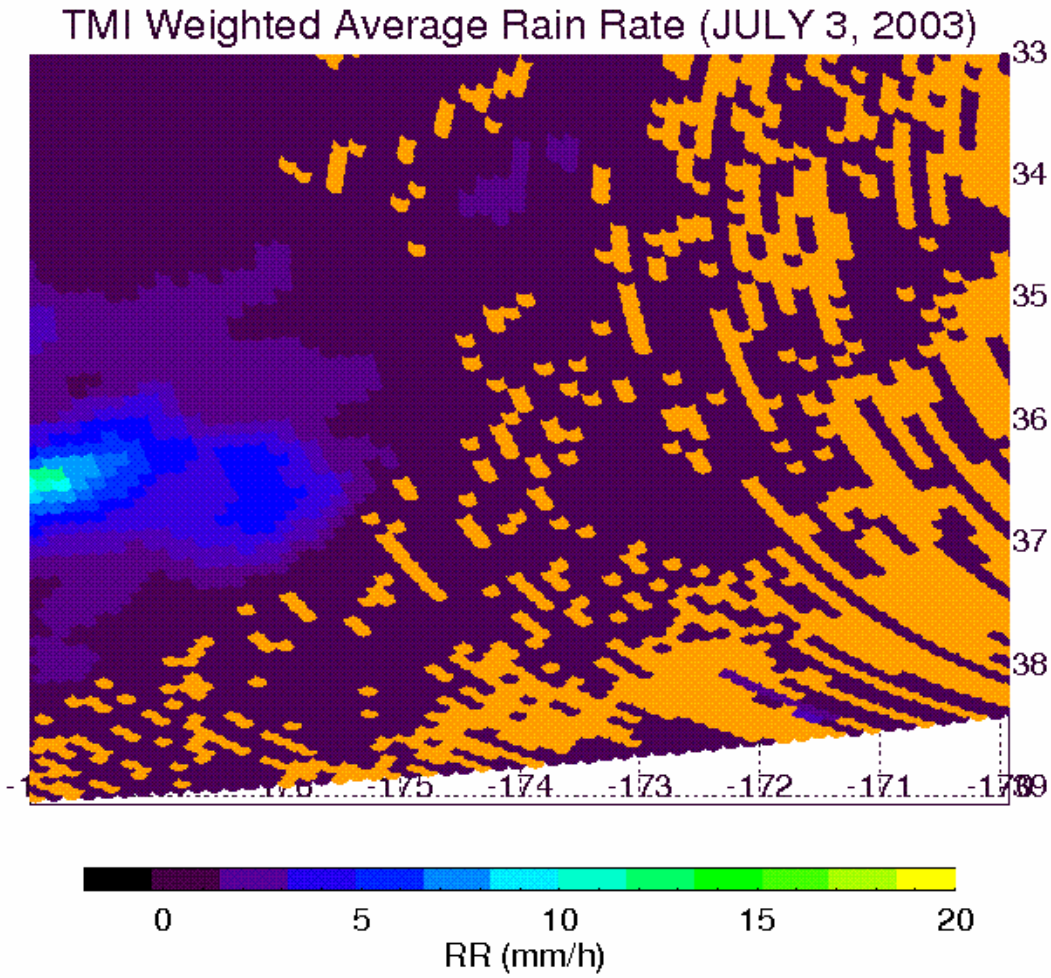

Figure 5.12, Continued.

(a)

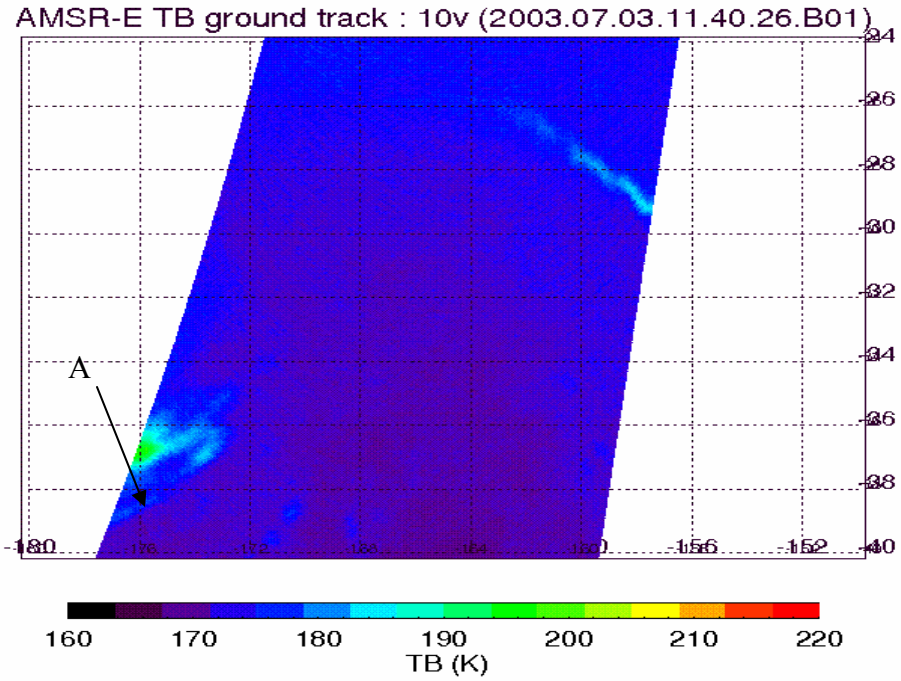

(b)

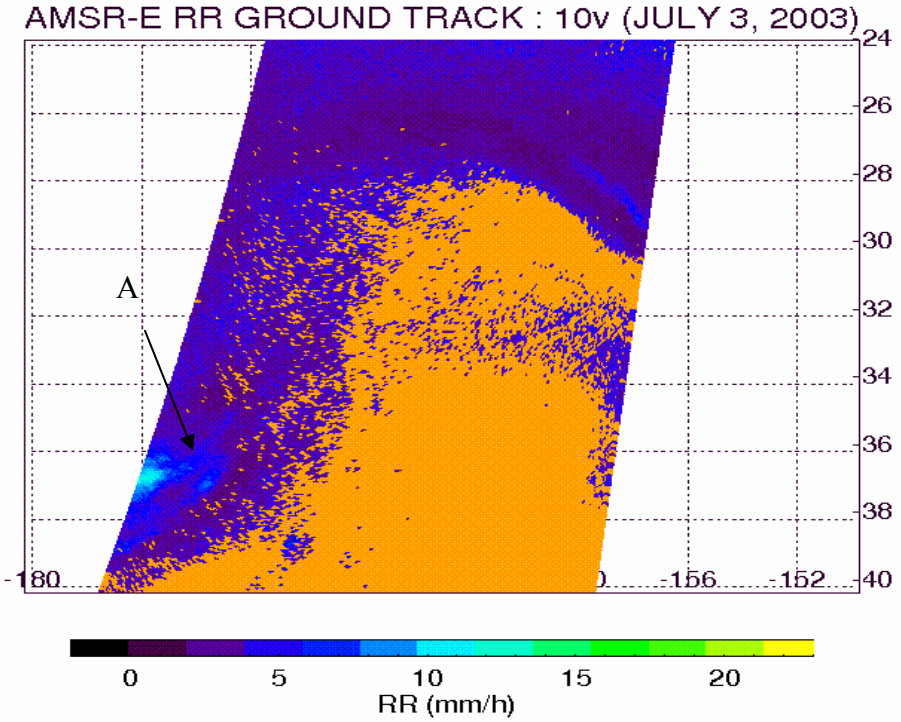

Figure 5.13 Winter hemisphere storm track observed by AMSR-E, July 3, 2003:11Z, 25-40S, 150-180W). a) Brightness temperature of 10GHz, vertical channel, b) Retrieved rain rates of 10GHz, vertical channel, c) Weighted average rain rates over area A. Orange color represents very dry area.

(c)

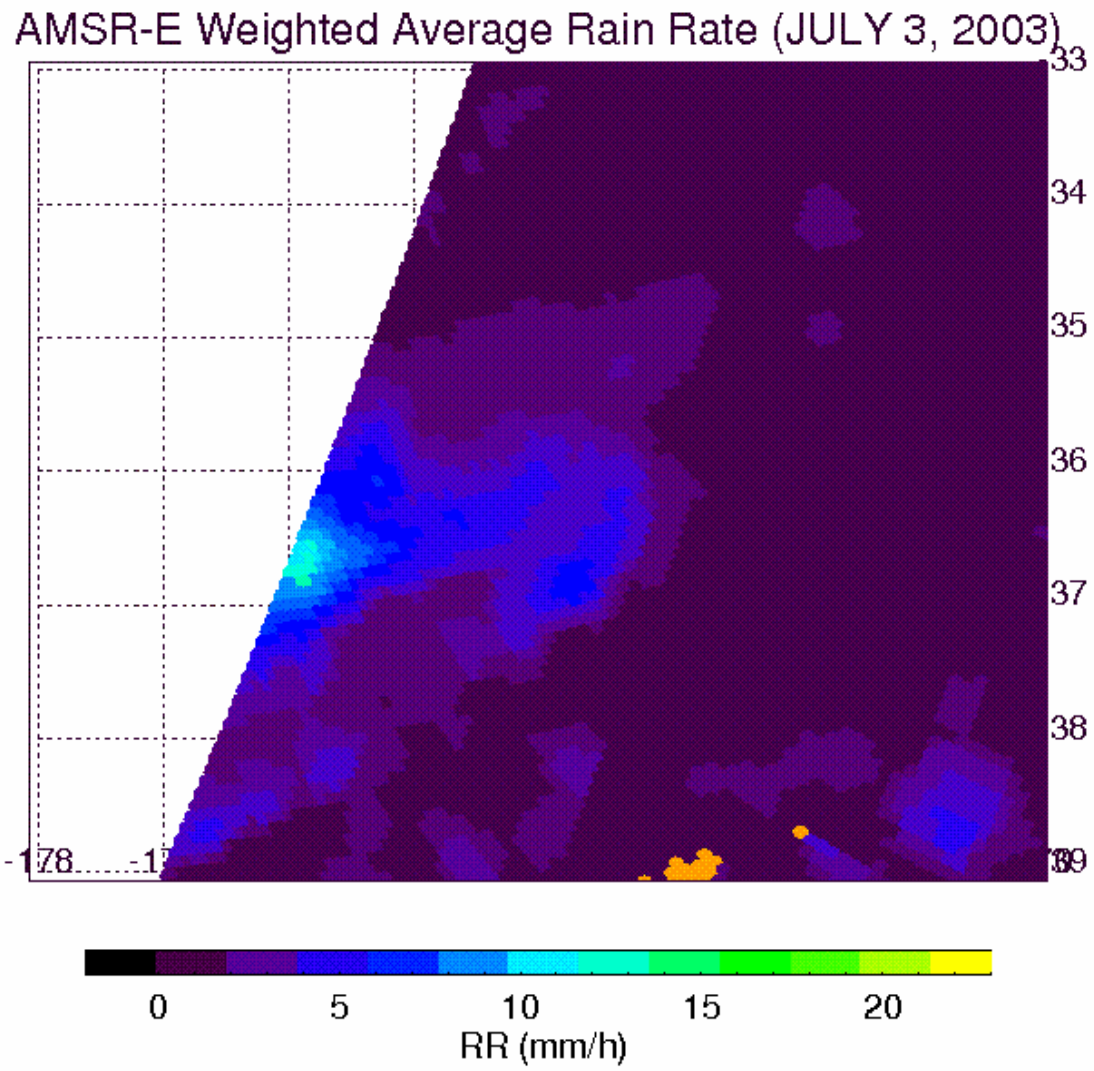

Figure 5.13, Continued.

As another way of verifying heavy rainfall over winter hemisphere, we compared the rainy cases (over about10mm/day) of 5° x 5° grid boxes for both the tropics and the high latitudes (5-10N, 150-155E and 30-35S, 165-170W). First, to examine the freezing level characteristics between the tropics and high latitudes, the distribution of freezing levels over the selected regions was generated. Figure 5.14 shows the freezing level histograms over tropics and high-latitude (winter hemisphere) for both the TMI and AMSR-E July, 2003 data. The freezing levels are distributed from around 3.5km to 5.5km (mean value ~ 4.5km) over the tropics and from about 1km to 4km (mean value ~ 2km) over the winter hemisphere respectively. Note that for the winter hemisphere, the freezing level histogram does not have a dominant peak and it shows a much larger variance compared to that of the tropics.

Rain rate histograms of the TMI and AMSR-E for those regions are shown in Figures 5.15 and 5.16 respectively. Accumulated monthly rain rate uncertainties over 5° x 5° grid box (red line) are included in the histograms. The computed average rain rates using the simple adding method, SUM RAIN, which includes all NO-FL samples, were 15.47mm/day for TMI and 13.64mm/day for AMSR-E over the tropics (5-10N, 150-155E and were 13.57mm/day for TMI and 10.58mm/day for AMSR-E over the winter hemisphere (30-35S, 165-170W). In this computation, the rain rates of all NO-FL cases were set to be zero. For inter-comparison, brightness temperature histograms of TMI and AMSR-E data for both regions were plotted in Figures 5.17a and 5.17b respectively. The rain rate histograms reveal that the rain features of the tropics and the winter hemisphere are very similar in spite of the distinctive differences in the brightness temperature histograms.

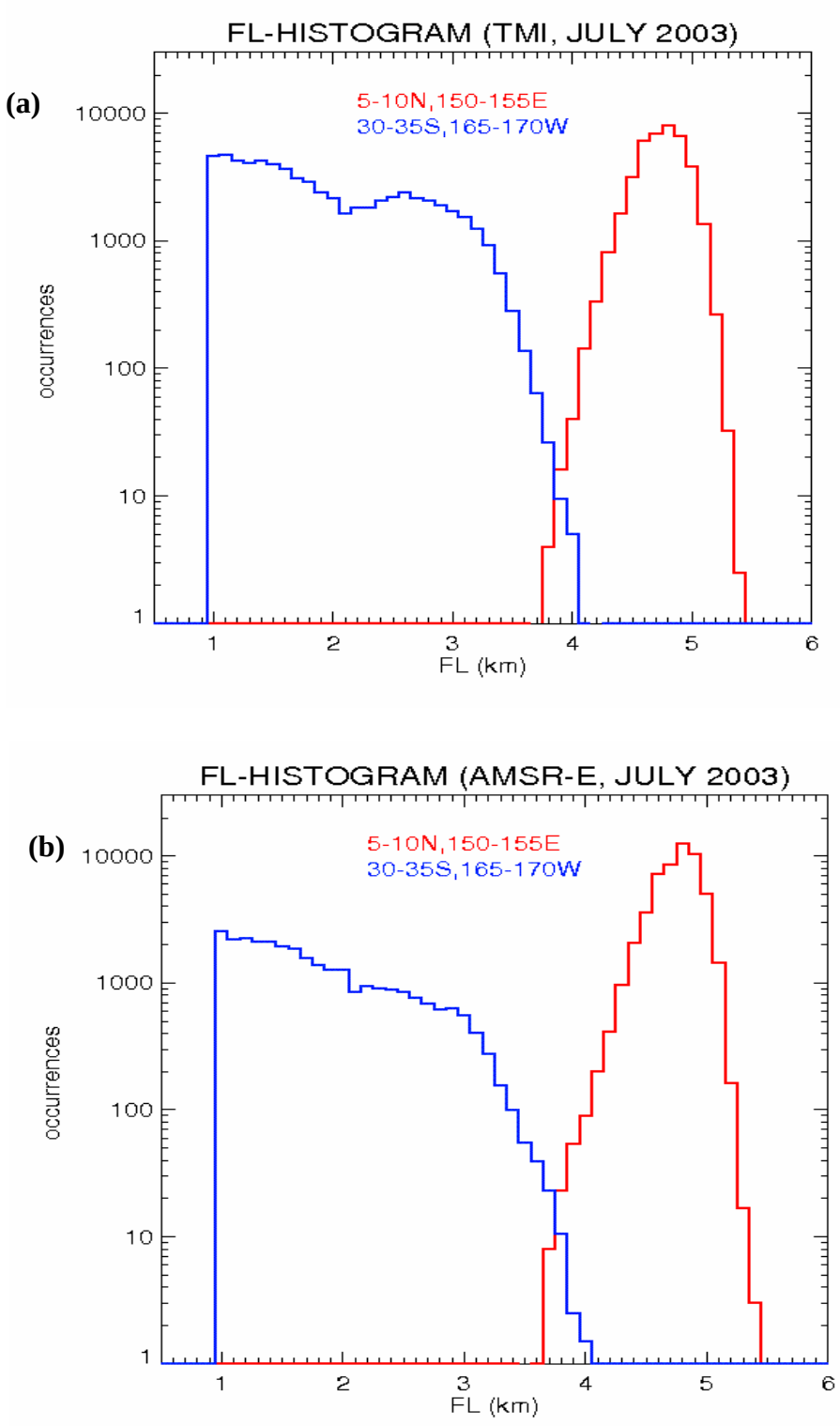

Figure 5.14 Comparison of the freezing level histograms between over the tropics (summer hemisphere: 5-10N, 150-155E) and over high latitudes (winter hemisphere: 30-35S, 165-170W). a) TMI, July 2003 data, b) AMSR-E, July 2003 data.

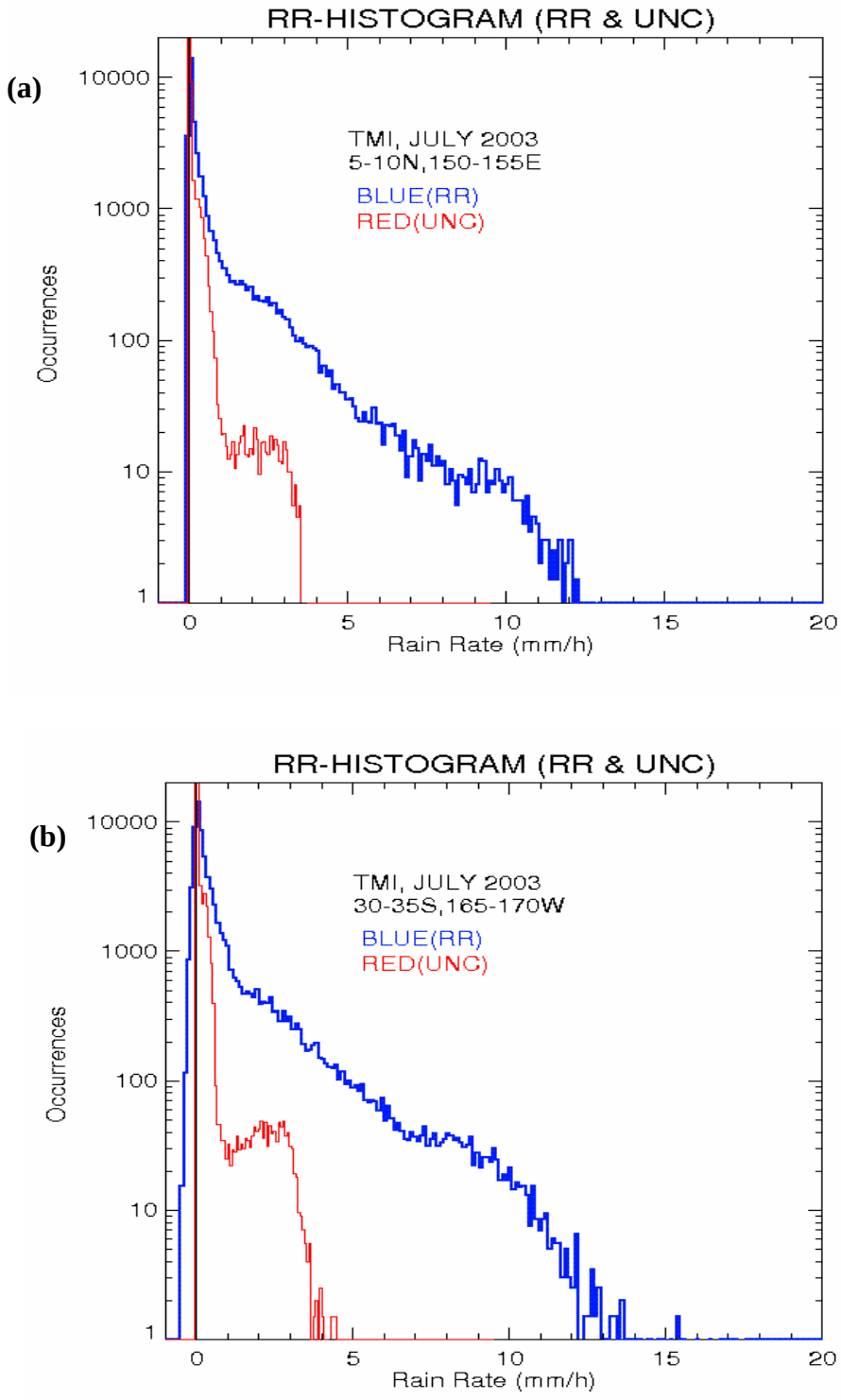

Figure 5.15 Rain rate and uncertainty histograms over 5° x 5° grid box for July 2003 TMI data. a) Over the tropics (5-10N, 150-155E), b) Over the winter hemisphere (30-35S, 165-170W).

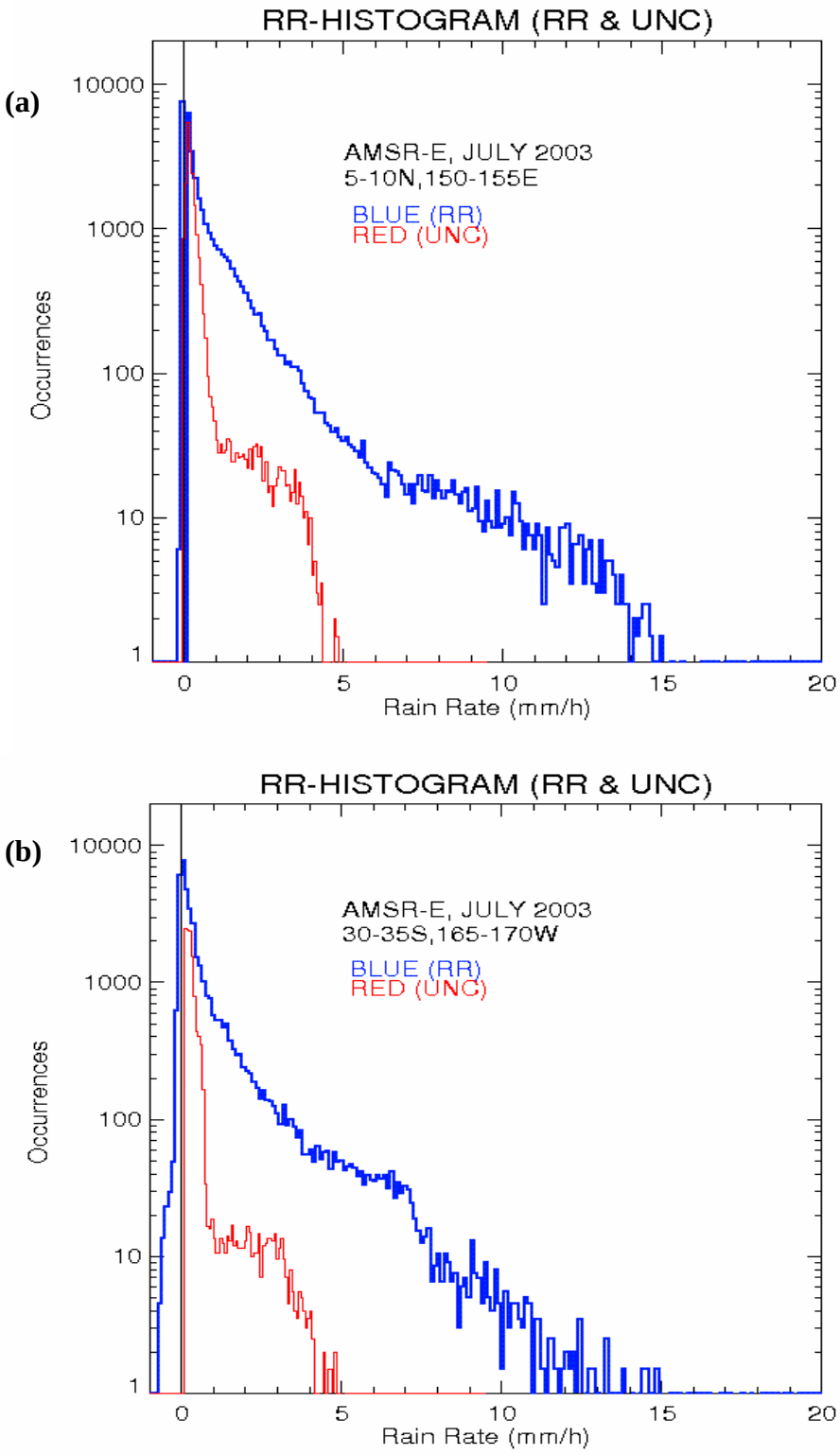

Figure 5.16 Rain rate and uncertainty histograms over 5° x 5° grid box for July 2003 AMSR-E data. a) Over the tropics (5-10N, 150-155E), b) Over the winter hemisphere (30-35S, 165-170W).

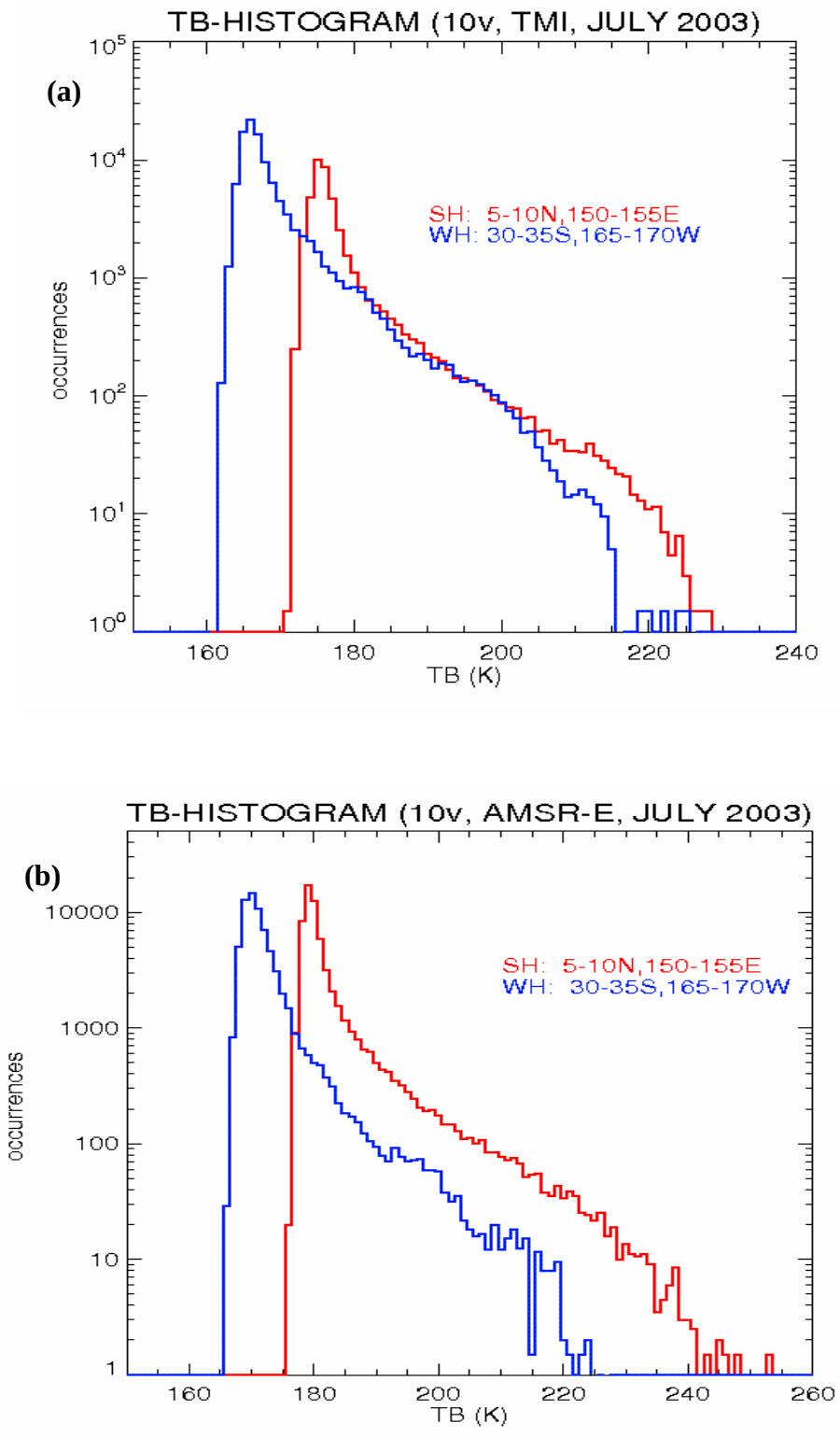

Figure 5.17 Comparison of brightness temperature histogram between the tropics (5-10N,150-155E) and the winter hemisphere (30-35S,165-170W). a) TMI, b) AMSR-E.

In addition, to examine whether the weighted average rain rates are accumulated correctly, we investigated the cumulative rain rate histograms which were constructed based on the accumulated rain rates using two, four, ten days and the entire month data. The comparison between the tropics and the winter hemisphere (Figures 5.18a and 5.18b) shows that they have very similar patterns: the highest peak is observed near zero rain and many portions of the total rain rates are contributed primarily by the medium range of rain rates (1~4mm/h). The same result was found in the AMSR-E data as well (Figures 5.19a and 5.19b). For comparison, the cumulative brightness temperature histograms (10GHz, vertically polarized channel) over the winter hemisphere (30-35S, 165-170W) were also shown in Figures 5.20. They show the many occurrences of high brightness temperatures (over 210K) which represent heavy rainfall events.

Therefore, it is obvious that very high monthly rain totals over high latitudes (winter hemisphere) can be achieved while those regions have very low freezing levels. Furthermore, it reveals the advantage of the experimental algorithm that accounts for rain rates on a pixel-by-pixel basis and that depicts heavy rain features over the winter hemisphere which were poorly handled by the operational algorithm.

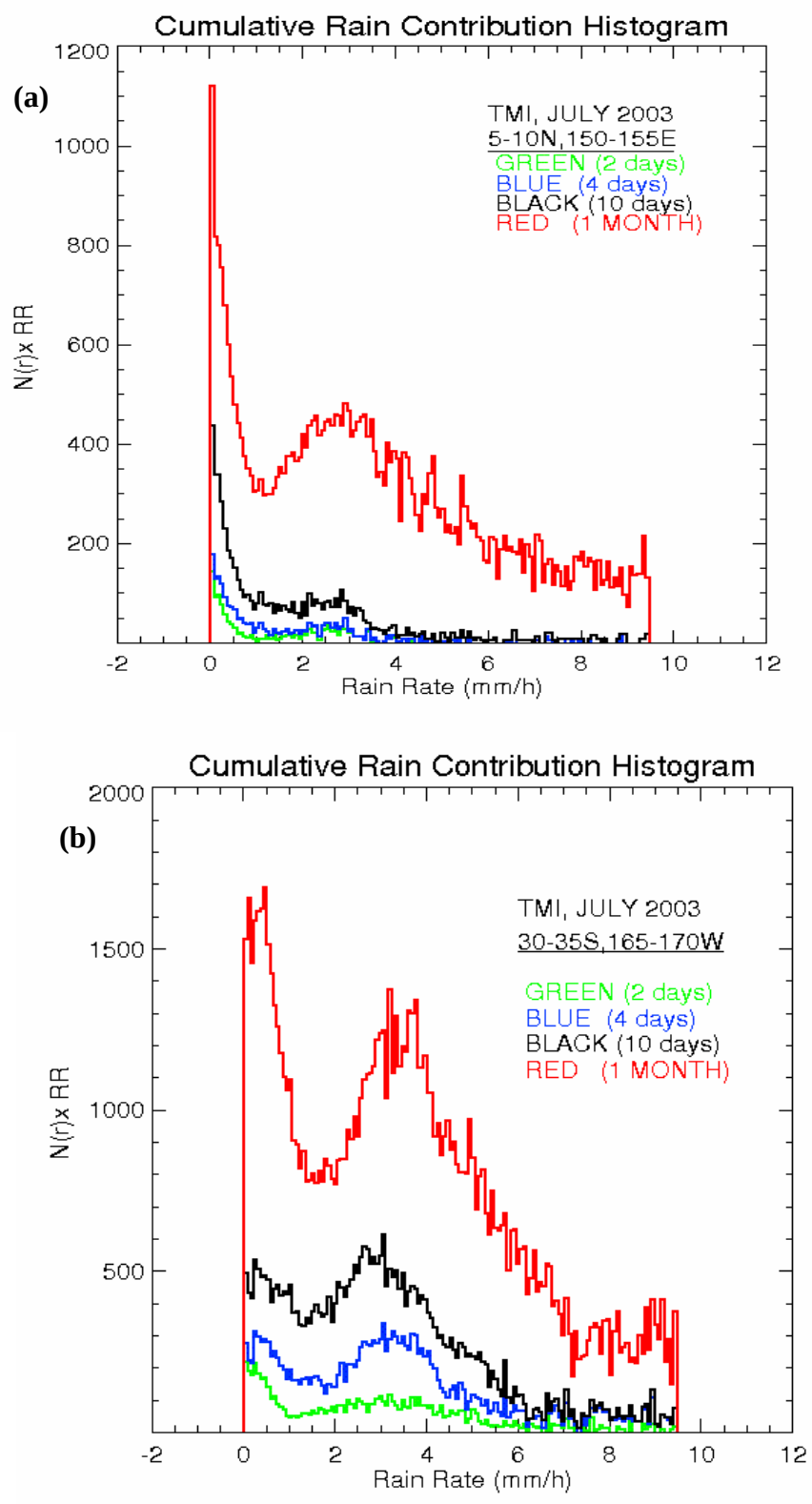

Figure 5.18 Comparison of the cumulative rain contribution histograms between over the tropics (summer hemisphere) and over high latitudes (winter hemisphere) using the July 2003 TMI data. a)5-10N, 150-155E (tropics), b) 30-35S, 165-170W (high latitude).

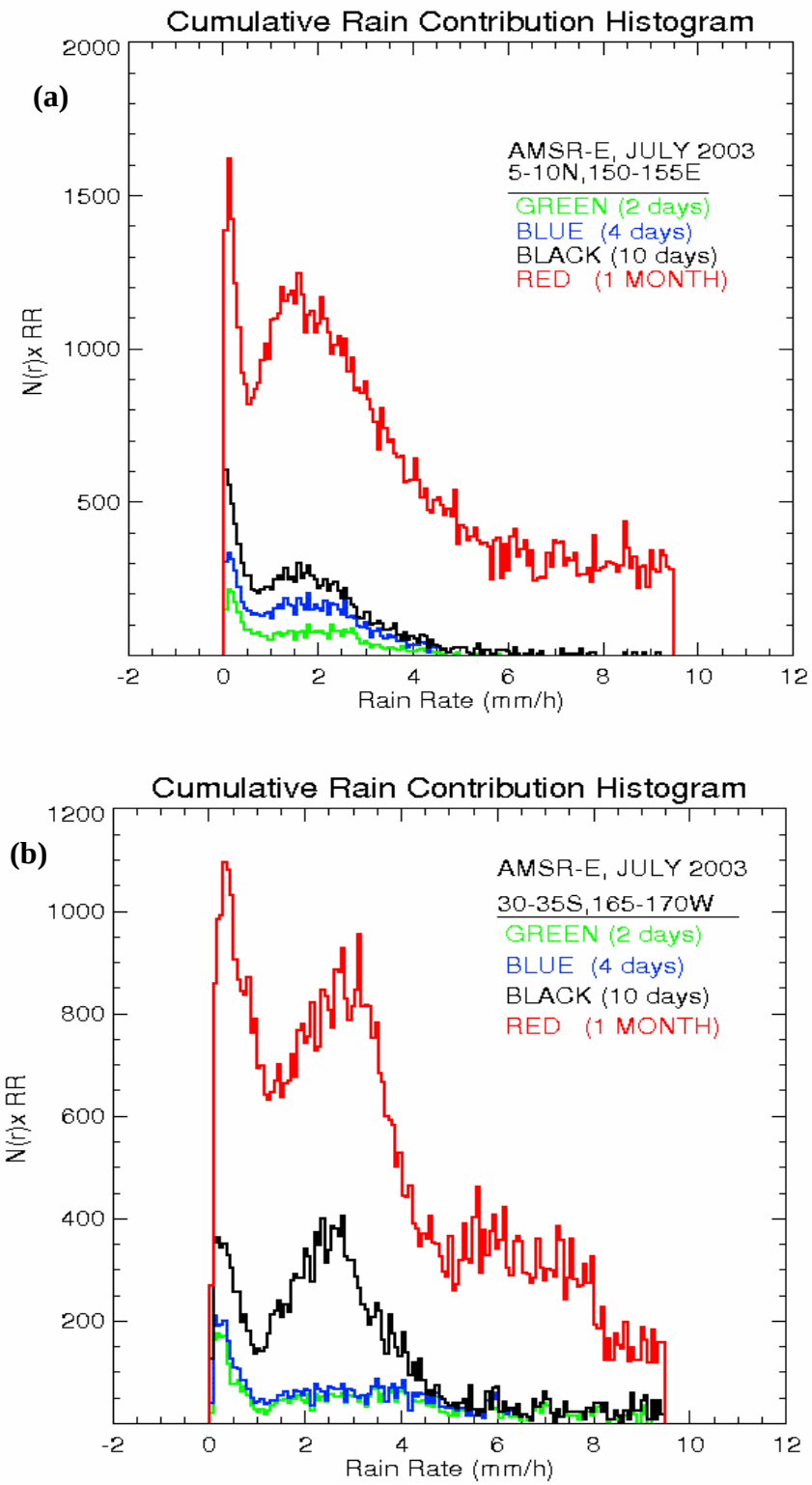

Figure 5.19 Comparison of the cumulative rain contribution histograms between over the tropics (summer hemisphere) and over high latitudes (winter hemisphere) using July 2003 AMSR-E data. a) 5-10N, 150-155E (tropics), b) 25-30S, 165-170W (high latitude).

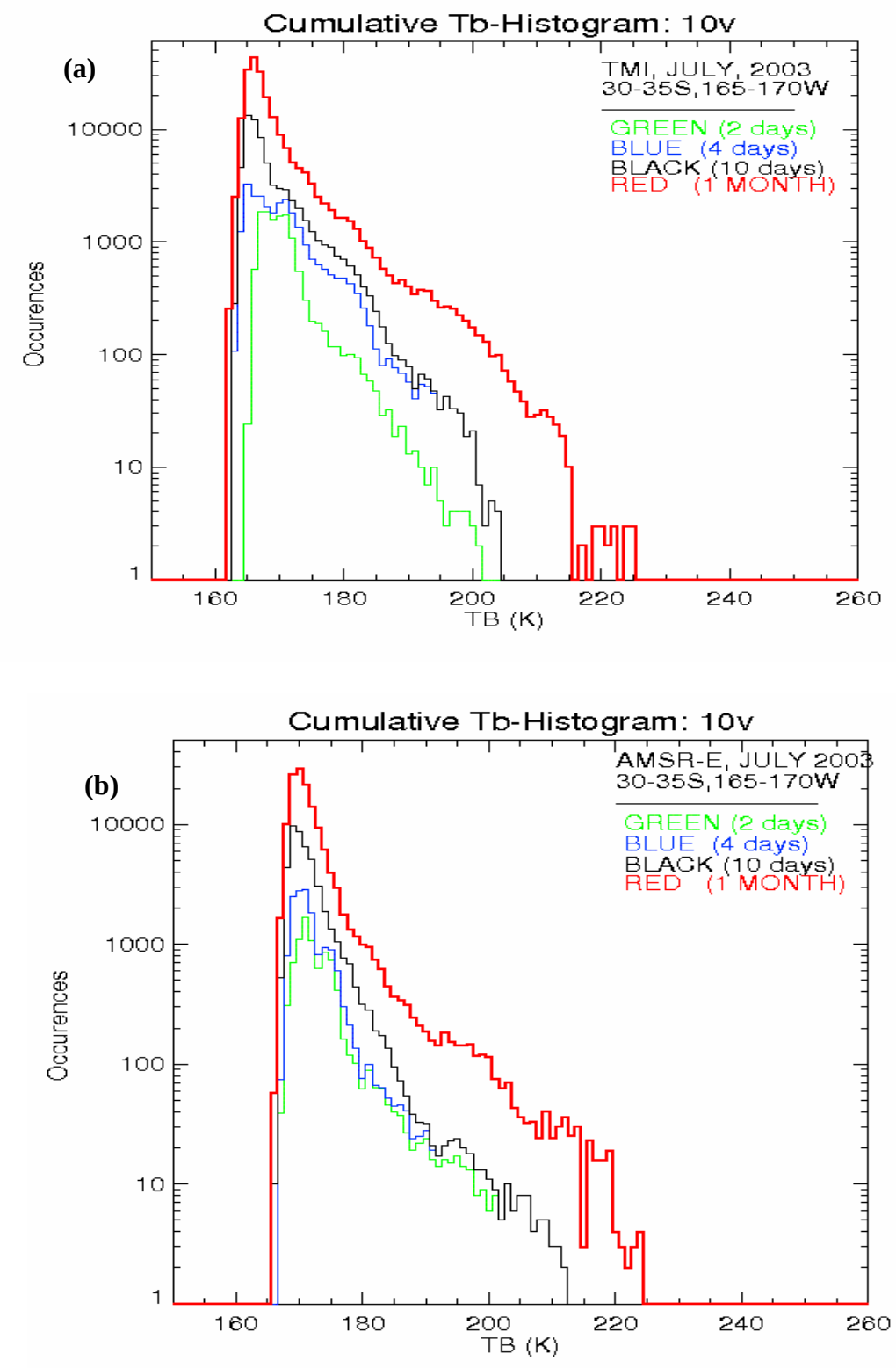

Figure 5.20 Cumulative brightness temperature histograms over high latitudes (winter hemisphere, 30-35S, 165-170W) using the July 2003 data. a) TMI, b) AMSR-E.

5.2 Error Analyses

The error models embedded in the experimental algorithm allow us to estimate rain retrieval errors quantitatively. The error analyses based on the constructed error models were carried out for both a scan and a granule of the AMSR-E data. Monthly rain rate uncertainty total was also estimated by summing all the pixel-by-pixel basis net uncertainties.

a. One scan basis

To analyze the uncertainties of the rainfall retrieval, a particular scan from the granule of the AMSR-E data (July 2, 2003: 20Z) was taken. Figure 5.21 shows the ground track of the brightness temperature of the 10GHz vertical channel of the AMSR-E selected for the analysis. The scan data are highlighted with a white space in the zoom-in image that contains raining storms (Figure 5.22a). This selected scan is also shown in Figures 5.22b. All six brightness temperatures of the scan are plotted in Figure 5.23 as a function of beam position.

To compute the rain rate uncertainties which also provide the weights for merging all six rain rates, several steps were taken. First, the freezing levels were estimated using the vertically polarized 18 and 24GHz channels (Figure 5.24) and then the rain rates were retrieved based on the computed rain rate/brightness temperature relationship as a function of freezing level. Note that the freezing levels approximately from beam positions 120 to 140 are spatially interpolated because when the 18GHz brightness temperature exceeds about 260K, retrieval of freezing levels from the two channels becomes very sensitive to the other assumptions of the model and thus unreliable.

Figure 5.25 shows the retrieved rain rates at the native resolution of the three channels (only vertically polarized channels of the 37, 18 and 10GHz). To indicate saturated cases, arbitrary rain rates of 20 and 25mm/h were assigned to the 37 and 18GHz respectively. At these saturation points, rain rate uncertainties of the channels are drastically increased and warm calibration uncertainty becomes very important. However, the uncertainty associated with warm calibration can be effectively handled by the weighted average of six channels. Especially, the 10GHz has a very important role for reducing this uncertainty because it is not affected by the saturation due to the very large dynamic range (up to 50mm/h).

The three rain rates match well at very low rain rates and the 19 and 10GHz overlap reasonably well in from medium to high rain rates (2~10mm/h). Small differences among the three rain rates at near zero rain are attributed to their different offsets. The computed rain rate uncertainties for all six channels are also plotted in Figure 5.26. The 37GHz shows the lowest uncertainties at the low rain rates (e.g. less then 2mm/h). At high rain rates, the 37GHz has a very high uncertainty while the 10GHz has low uncertainties.

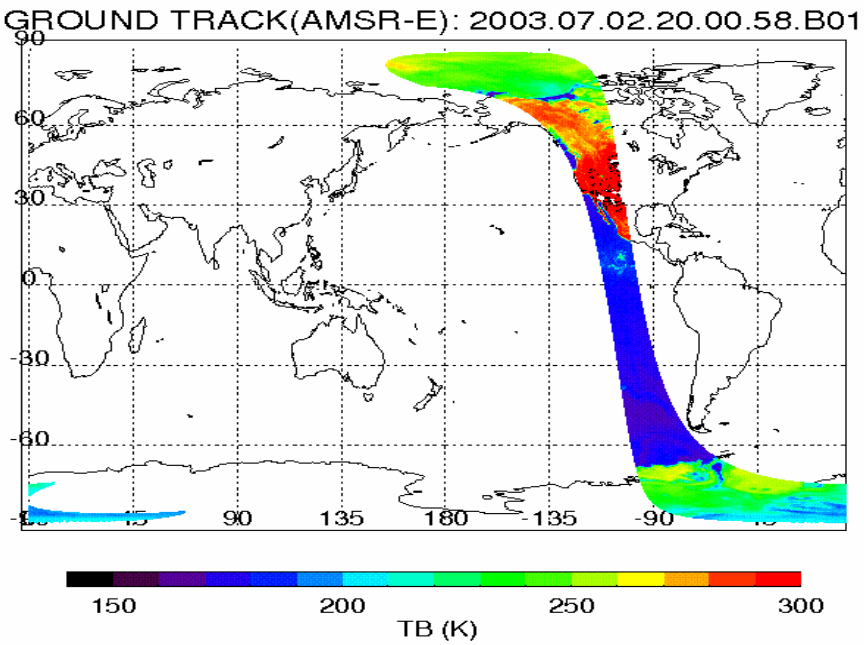

Figure 5.21 Ground Track of the 10GHz-vertically polarized brightness temperature of one granule of the AMSR-E data (July 2, 2003:20Z).

(a)

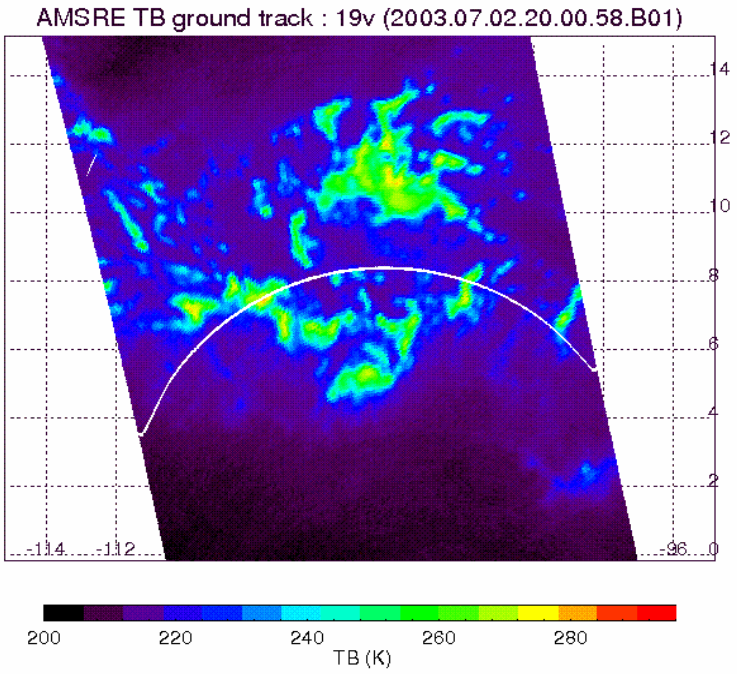

Figure 5.22 a) Selected scan data from a granule data. The scan which was used in this analysis is replaced with white, b) Image of the elected single scan data (shown in Figure 5.22a) for the 19v channel.

(b)

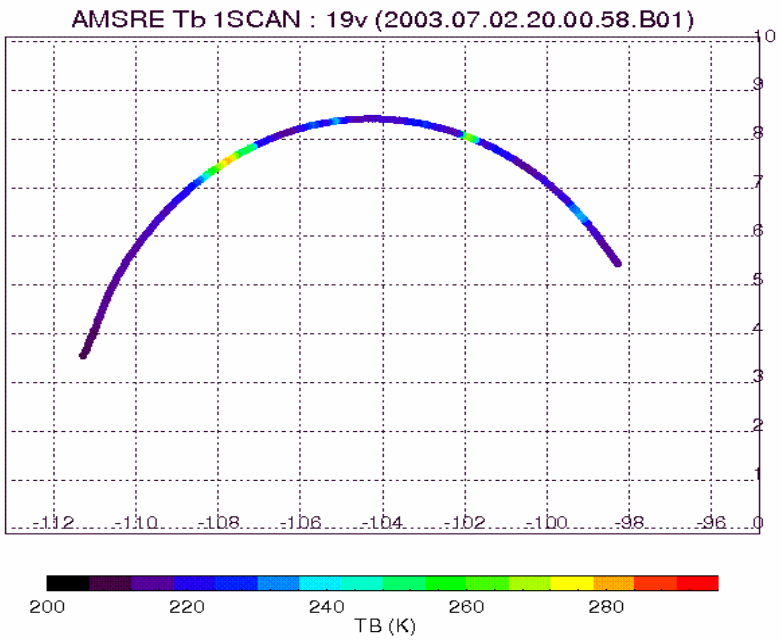

Figure 5.22, Continued.

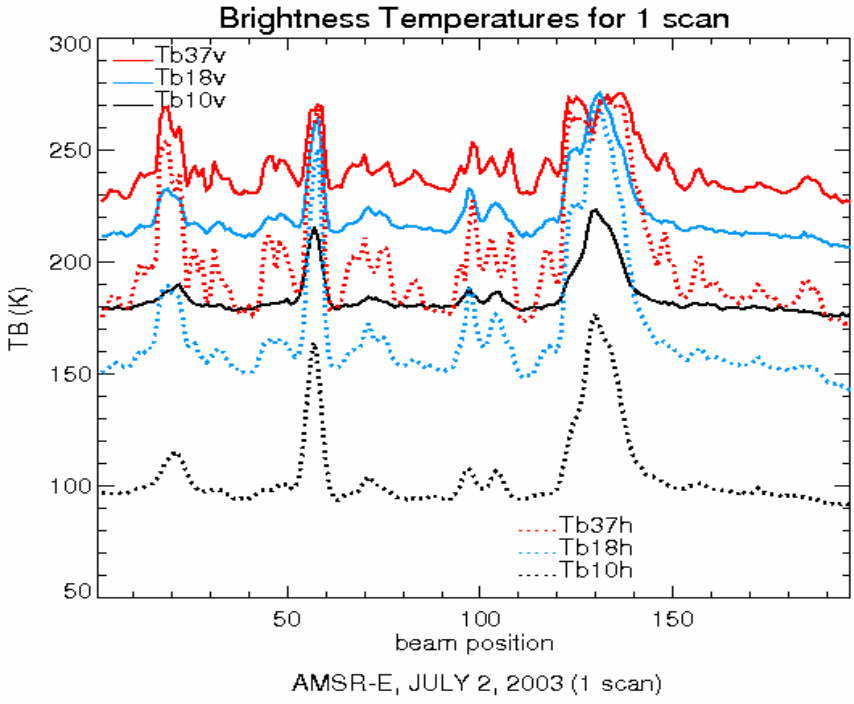

Figure 5.23 Brightness temperatures variation as a function of the beam position for the selected scan. All six channels (37, 18 and 10GHz H & V) are presented.

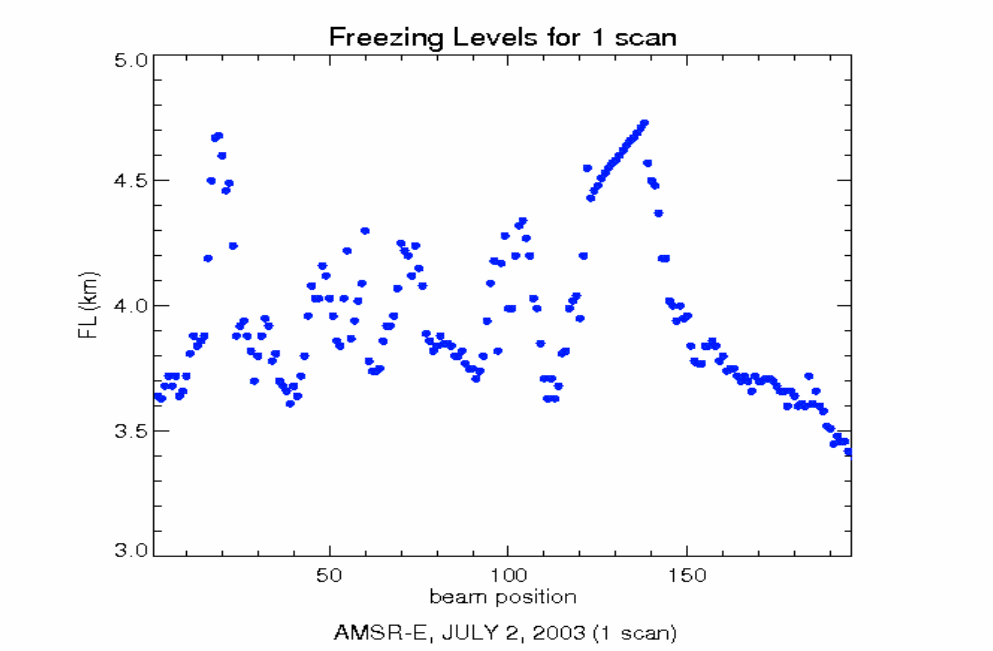

Figure 5.24 Retrieved freezing levels as a function of the beam position.
In the regions where 18GHz is over 260K, spatial interpolation is conducted.

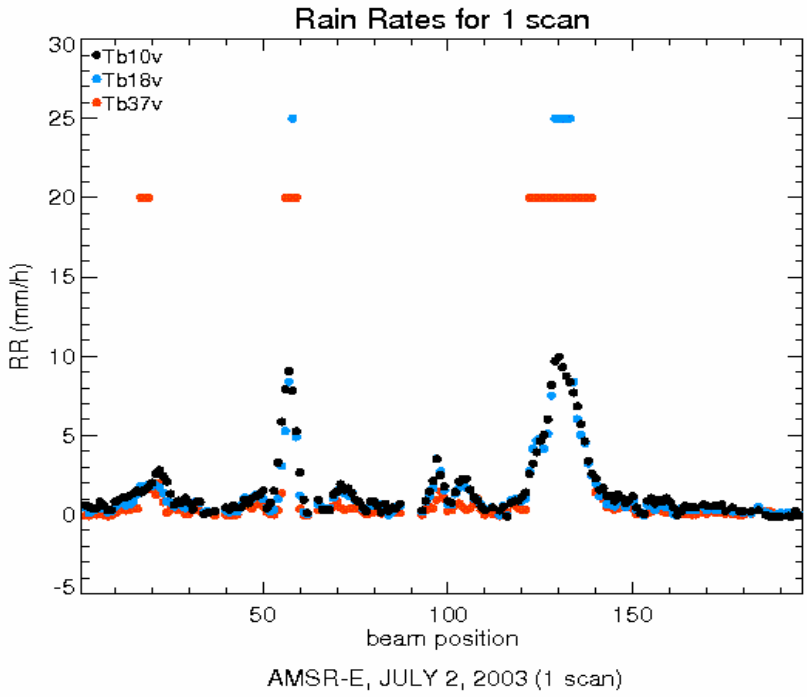

Figure 5.25 Retrieved rain rates with native resolution as a function of the beam position.
In this figure, only vertically polarized channels were shown.

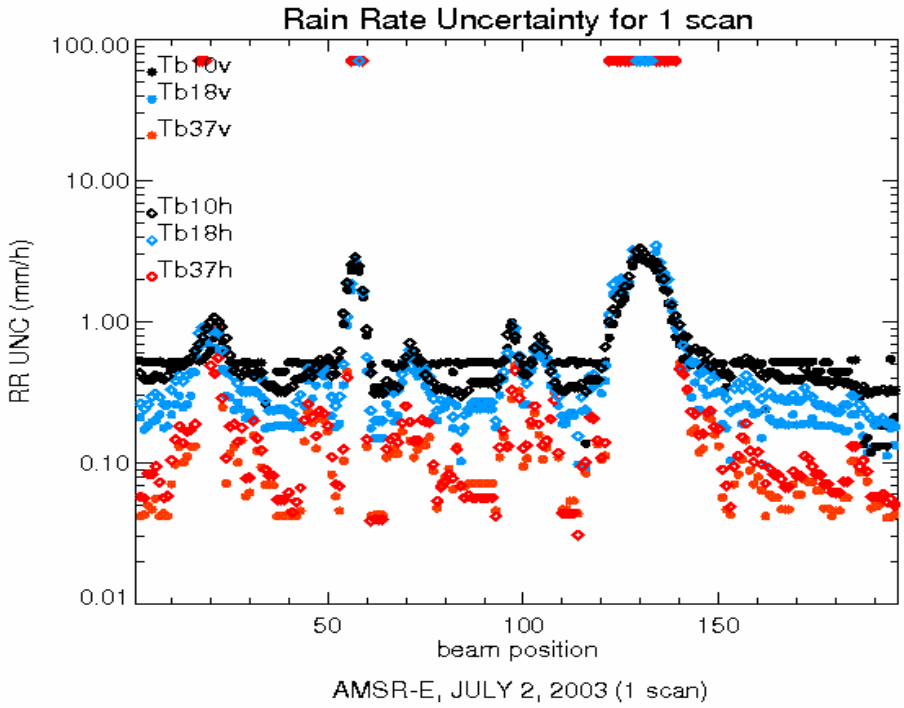

Figure 5.26 Computed rain rate uncertainties as a function of the beam position; all six channels.

Second, the polarizations were merged, that is, the vertical and horizontal polarizations of each frequency were combined. Since the saturation of the vertical and horizontal polarization is different (saturation of vertical channel is little quicker), when the vertical channel is saturated, the horizontal channel is utilized instead up to its saturation point. Figures 5.27a and 5.27b show the uncertainties and the equivalent weights correspond to the two 37GHz channels. The vertically polarized channel shows a slightly higher uncertainty than the horizontally polarized channel near saturation due to its little earlier saturation. Higher uncertainty results in less weight because weight is simply an inverse of error variance. The three channels' rain rate and the uncertainties after merging the polarization are plotted in Figures 5.28 and 5.29 respectively

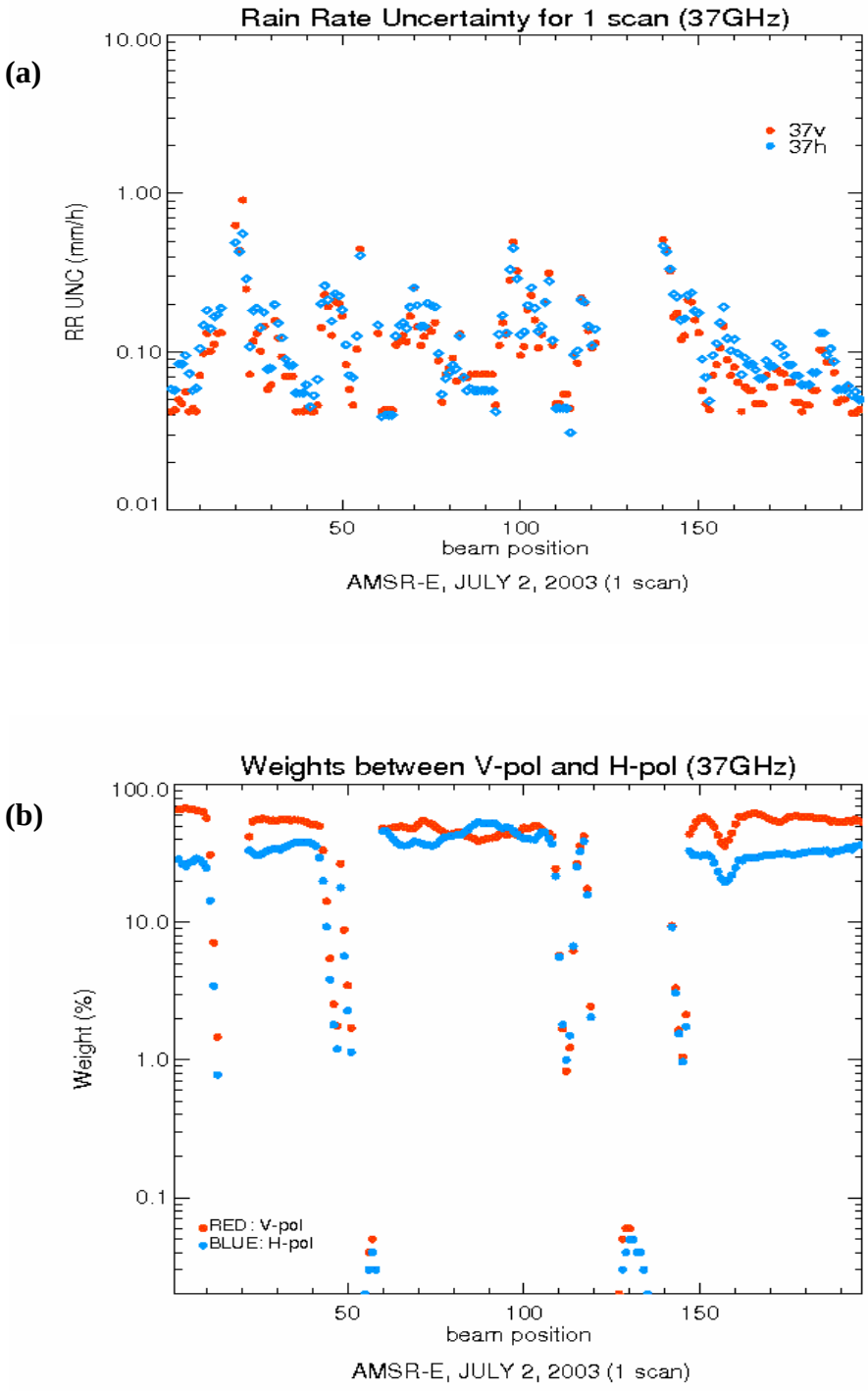

Figure 5.27 a) Computed rain rate uncertainties of the two polarizations for the selected scan of the 37GHz. Red circles indicate the vertically polarized channel and blue diamonds represent the horizontally polarized channel, b) Weights of the two polarizations for the selected scan of the 37GHz.

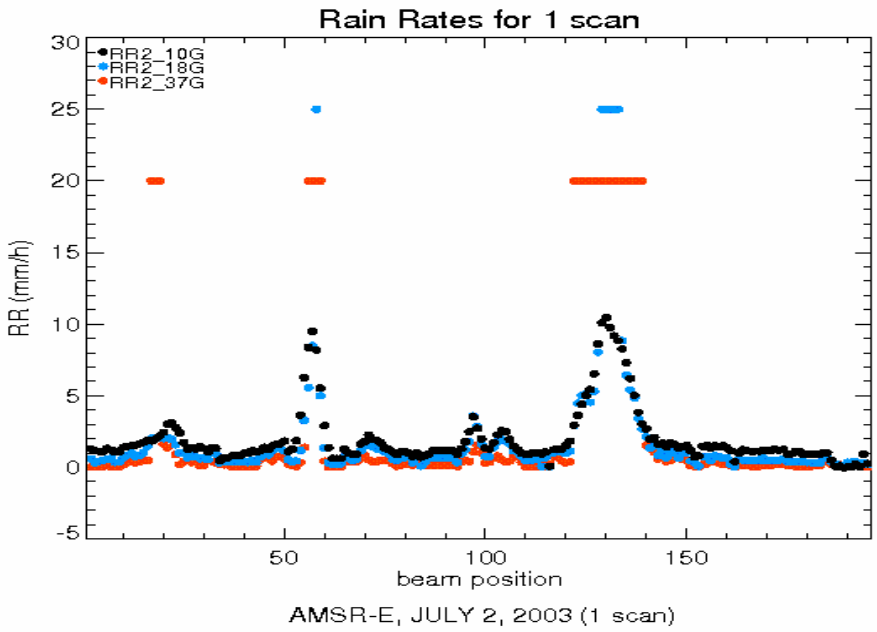

Figure 5.28 Polarization-combined rain rates for the selected scan data. The values of 20mm/h and 25mm/h were assigned to the 37 and 18GHz respectively to represent the saturated cases.

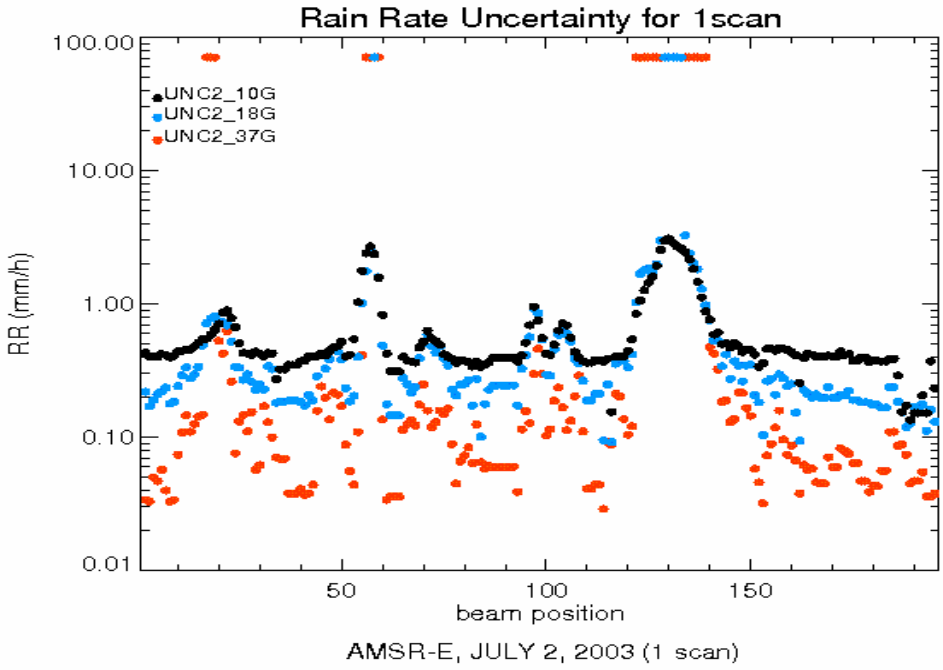

Figure 5.29 Computed rain rate uncertainties for the polarization- combined rain rates of the selected scan data.

Third, the 37 and 18GHz frequencies were smoothed to the resolution of the 10GHz to match locations. To obtain the smoothing function (or antenna gain function in terms of the 10GHz foot print size), the assumption of a Gaussian beam yields

$$Wi = \exp[-\frac{1}{2}(\frac{xi^2}{\Delta^2 x} + \frac{yi^2}{\Delta^2 y})]$$

where, Wi = smoothing function. $\Delta^2x=\sigma^2_{10(x)} - \sigma^2_{i\,(x)}$, $\Delta^2y=\sigma^2_{10(y)} - \sigma^2_{i\,(y)}$, i=each channel which is smoothed (18 or 37GHz), σ^2_{10} is the variance of the Gaussian of the 10GHz beam and σ^2_i is the variance of the Gaussian of the 18 or 37GHz beam (Computed numbers for each frequency are presented in Table 5.1). The rain rates and the uncertainties after the smoothing including combining the polarizations are shown in Figures 5.30 and 5.31.

Table 5.1. Resolution (IFOV) and the variances of the Gaussian of each channel.

	10GHz	18GHz	37GHz
IFOV (km x km)	51 x 30	27 x 16	14 x 8
σ^2_x	162	46	12
σ^2_y	469	131	35

Finally, the retrieved rain rates from each frequency (after the smoothing process and merging the two polarizations) were combined into one rain rate (weighted average rain rate) based upon the weights which were established from the rain rate uncertainties of each channel. The rain rate uncertainties which are associated with each error source

were computed based on the error models (Section 4.3) and these uncertainties were combined to compute a net error for each of the rain rates for each smoothed pixel and all the rain rates were merged (averaged) by the weights of the six channels which are simply the inverse of the net error variance. The frequency with the lowest uncertainty has the highest weight when the three frequencies are merged. The weighted average rain rates merged from all six rain rates along with the computed total uncertainties are shown in Figure 5.32.

To address explicitly the individual weights of each channel, the computed weights for all six channels were plotted as a function of the beam position (Figure 5.33). It is clearly shown that the contribution of 37GHz is highest at low rain rates and the 10GHz has maximum weight at very high rain rates. For medium rain rates, the contributions from the 19 and 10GHz are mixed.

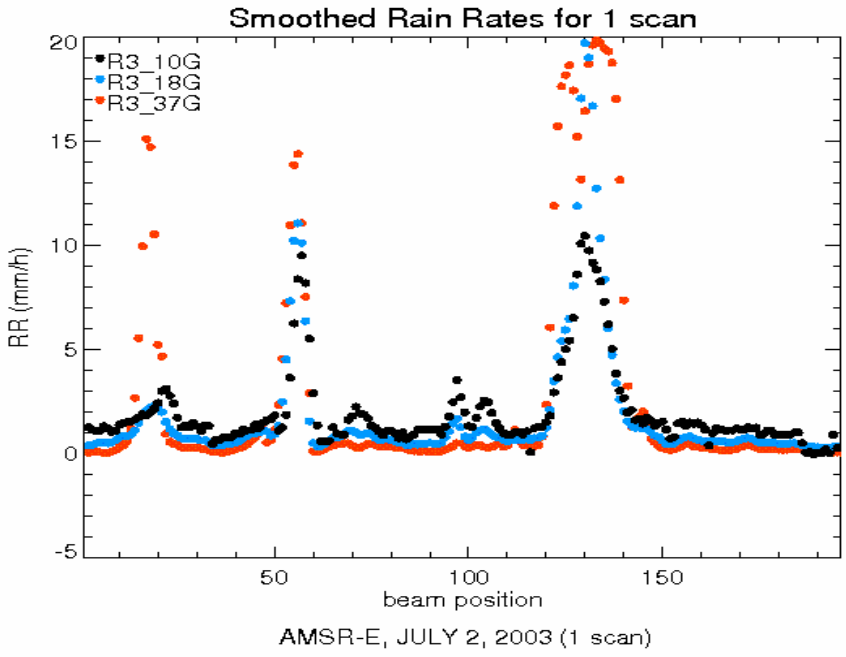

Figure 5.30 Smoothed rain rates variation for the selected scan data.

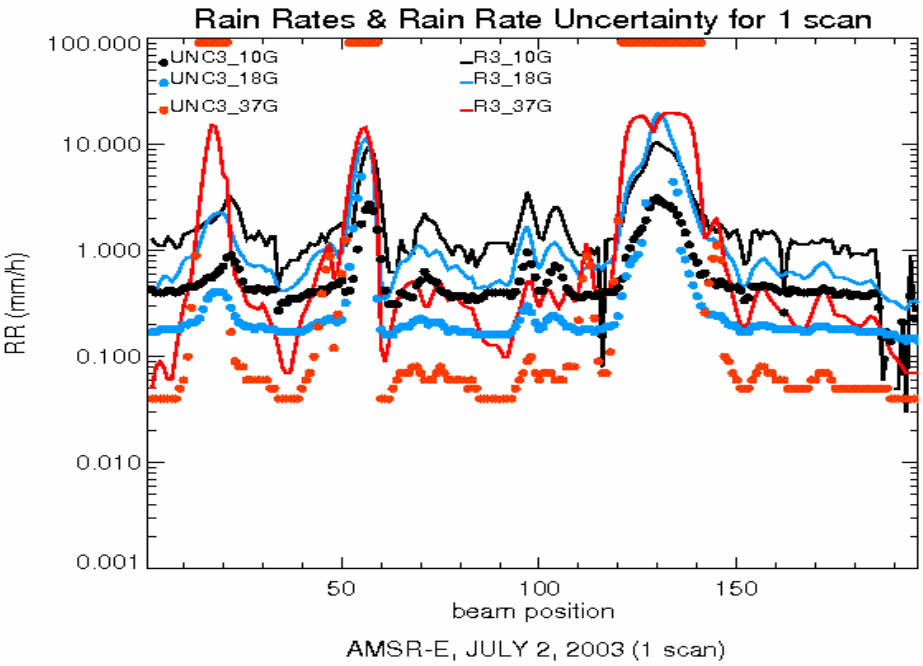

Figure 5.31 Computed rain rate uncertainties for the smoothed rain rates of the selected scan data.

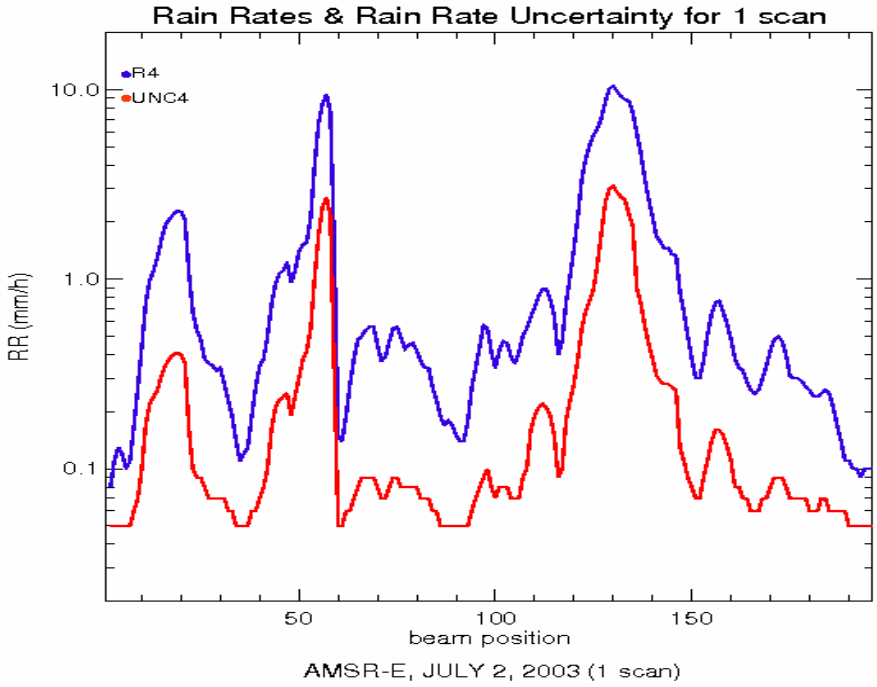

Figure 5.32 Weighted average rain rates with the computed rain rate uncertainties for the selected scan data

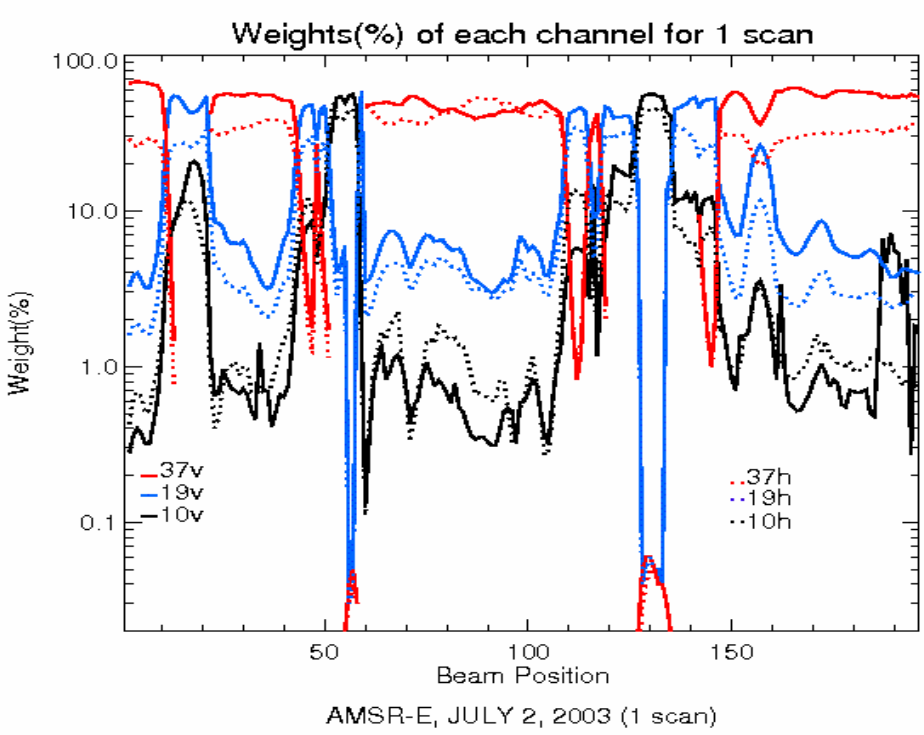

Figure 5.33 Computed weights for the each channel as a function of the beam position.

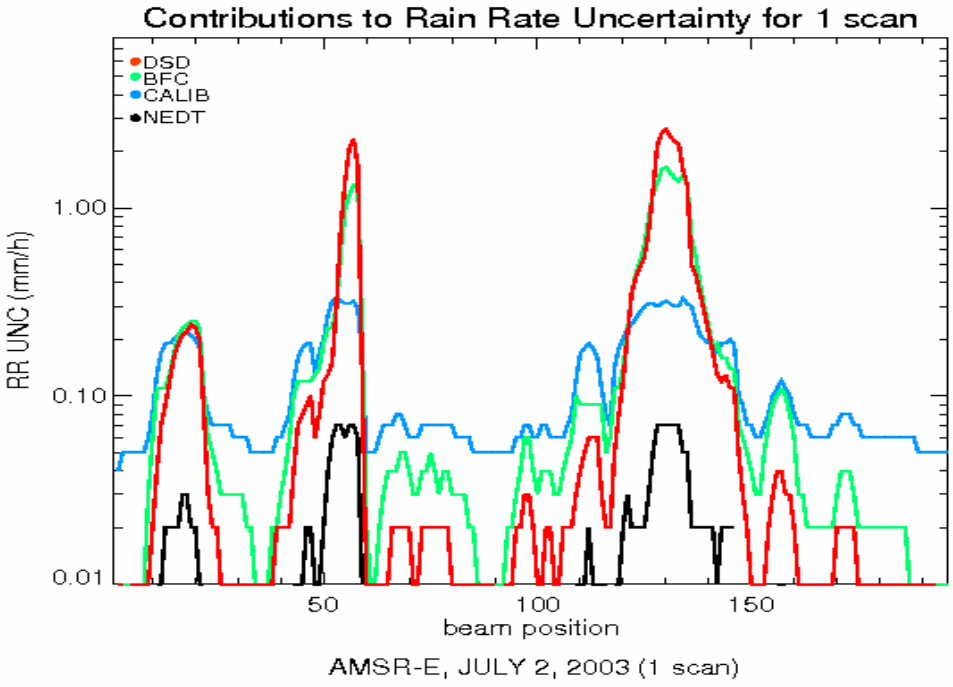

Figure 5.34 Rain rate uncertainty contributed by each source. Four sources (DSD, BFC, CALIB and NEDT) were considered as primary uncertainty sources.

The uncertainty contributions from the four principal error sources are examined as well (Figure 5.34). The calibration uncertainty dominates at low rain rates and the drop size distribution uncertainty has the largest impact on high rain rates. Calibration error has a very large percentage contribution at low rain rates (the 37GHz dominates) but decreases at high rain rates because the weights of lower frequencies become dominant as rain rate increases. For the drop size distribution uncertainty, sensitivity analyses (Section 4.3) suggests that 37GHz raining estimates are not very sensitive to the details of drop size distribution, but 18 and 10GHz are more sensitive. As a result, at the high rain rates (where 10GHz dominates) the contribution by the drop size distribution is highest. However, the beam filling errors are reduced with increasing rain rate since the relationship of the rain rate and the brightness temperature is less non-linear at the lower frequencies while they have lower resolutions.

b. One granule basis

As an extension from the one scan-basis (one dimensional) analysis, the analysis on a granule-basis (two dimensional) was also conducted. The same procedures which were addressed in the previous single scan analysis to compute weighted average rain rates were taken: merging polarizations of each frequency, smoothing of the 18 and 37GHz and then combining the three frequencies. For the analysis, a particular domain (0-15N, 95W-115W) from a granule of the July 2, 2003 AMSR-E data was selected. The brightness temperature ground tracks of the three channels (10, 18 and 37GHz, vertically polarized channels only) are plotted in Figures 5.35a-c.

First, using the 18 and 24GHz channels, the freezing levels were retrieved. A map of freezing levels over the every pixel is shown in Figure 5.36. Some freezing levels are spatially interpolated in case the 18GHz's brightness temperatures exceed about 260K. Based on these freezing levels, the rain rates at each native resolution were retrieved and are presented in Figures 5.37a-c. (vertically polarized channels only). Problematic cases for the freezing level retrieval over very dry region, the rain rates are assumed to be zero and these regions are indicated by orange.

(a)

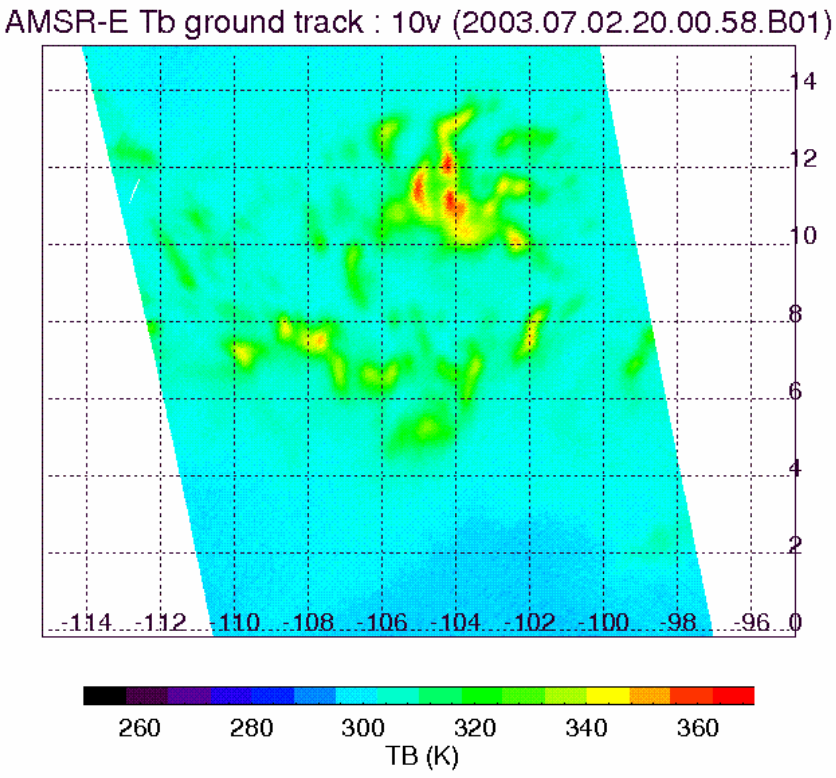

Figure 5.35 Brightness temperature ground track of one granule data over the selected area (0-15N, 95-115W) for the AMSR-E data (July 2, 2003: 20Z), a) 10v channel, b) 18v channel, c) 37v channel

(b)

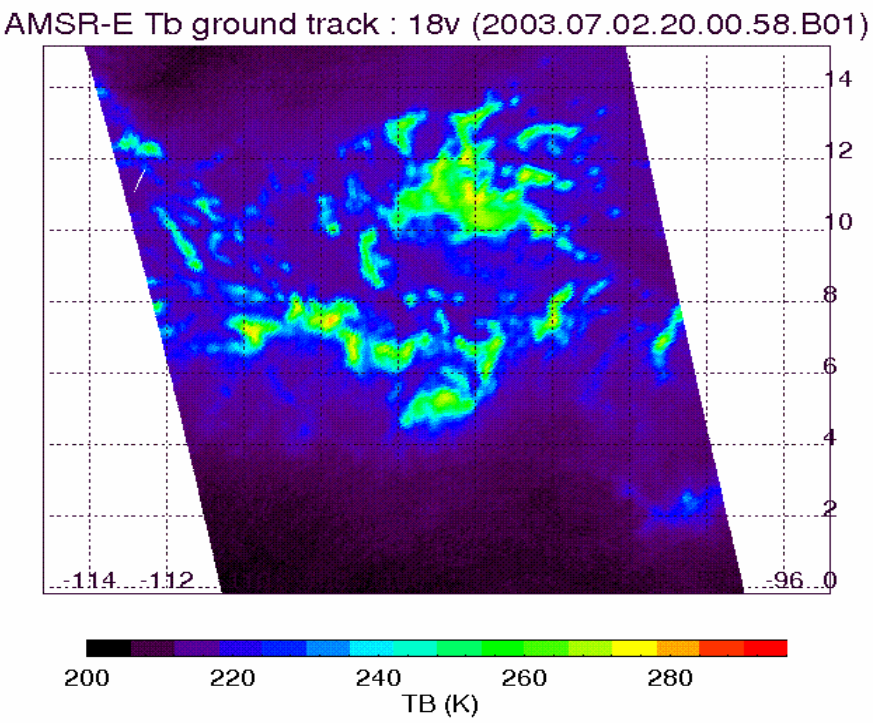

(c)

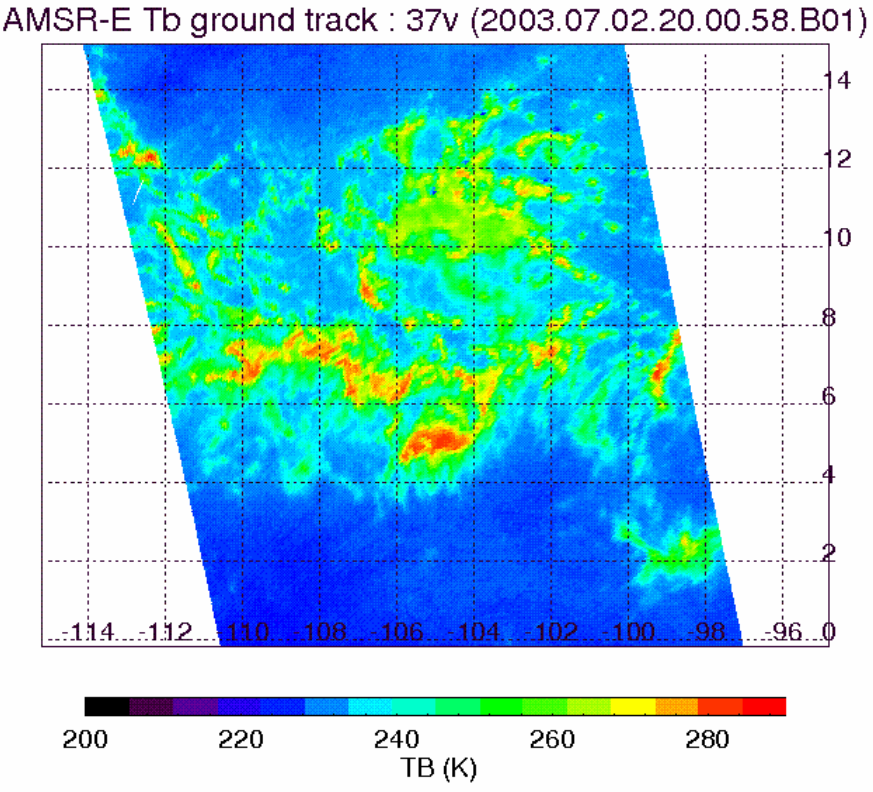

Figure 5.35, Continued.

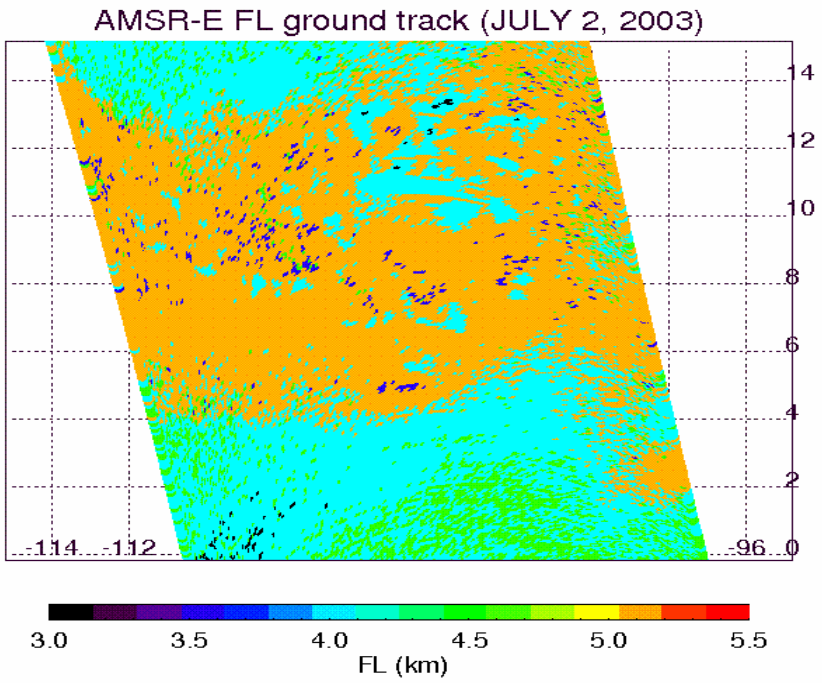

Figure 5.36 Map of the retrieved freezing levels from the selected granule over the selected area (0-15N, 95-115W) for (AMSR-E, July 2, 2003: 20Z).

(a)

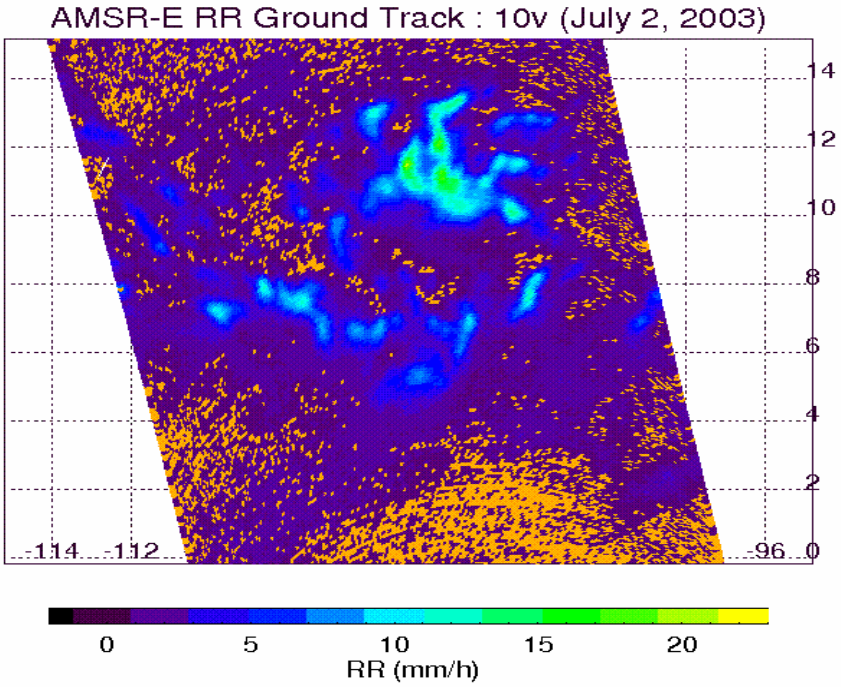

Figure 5.37 Retrieved rain rate of one granule data over the selected area (0-15N, 95-115W) for the AMSR-E data (July 2, 2003: 20Z), a) 10v channel, b) 18v channel, c) 37v channel.

(b)

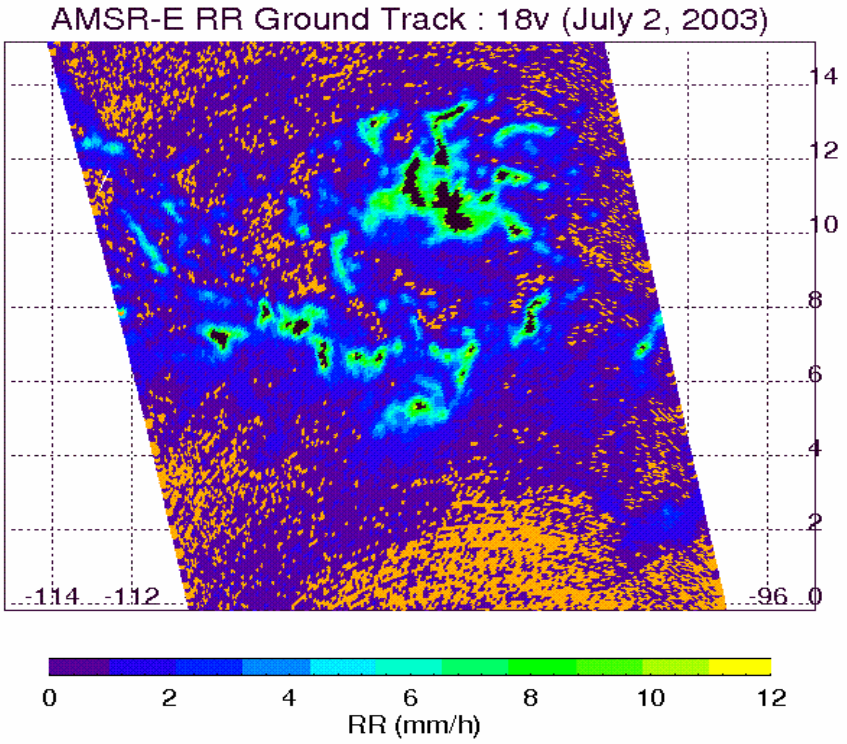

(c)

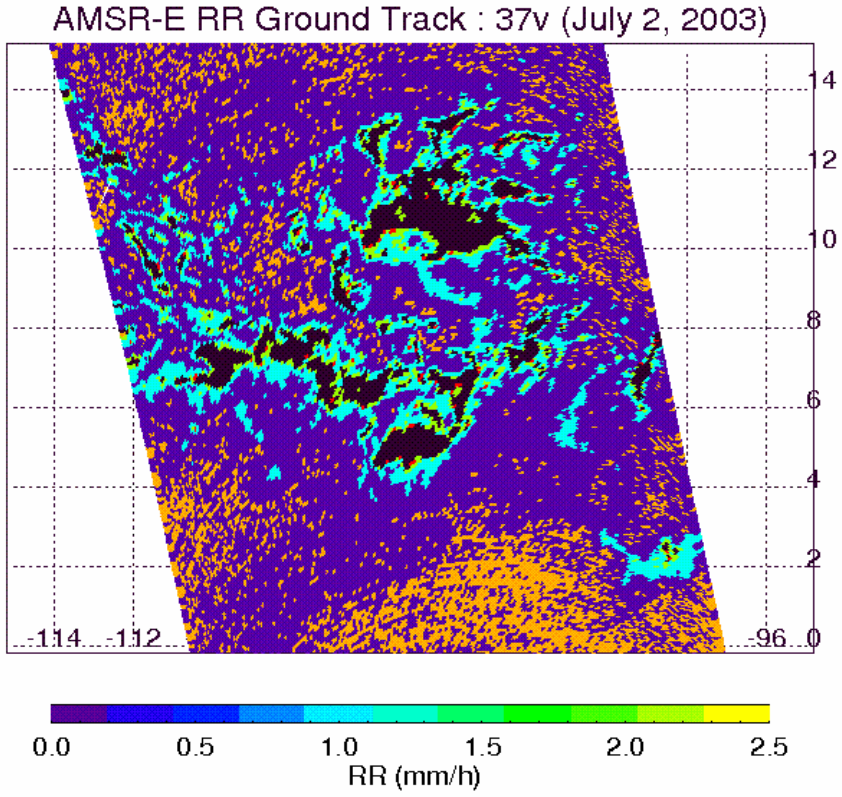

Figure 5.37, Continued.

Those six individual rain rates were merged into three rain rates by combining polarizations and then the rain rates of the 18 and 37GHz were smoothed to the 10GHz resolution. Those smoothed rain rates of the 18 and 37GHz are shown in Figures 5.38a and 5.38b. Note that the saturated regions over the deep convection are displayed as black. Compared with the native resolution rain rates of the 18 and 37GHz (Figures 5.37b and 5.37c), the smoothing effect, which is averaging rain rates with the Gaussian weighting function in terms of the 10GHz footprint size, is clearly shown in these Figures.

(a)

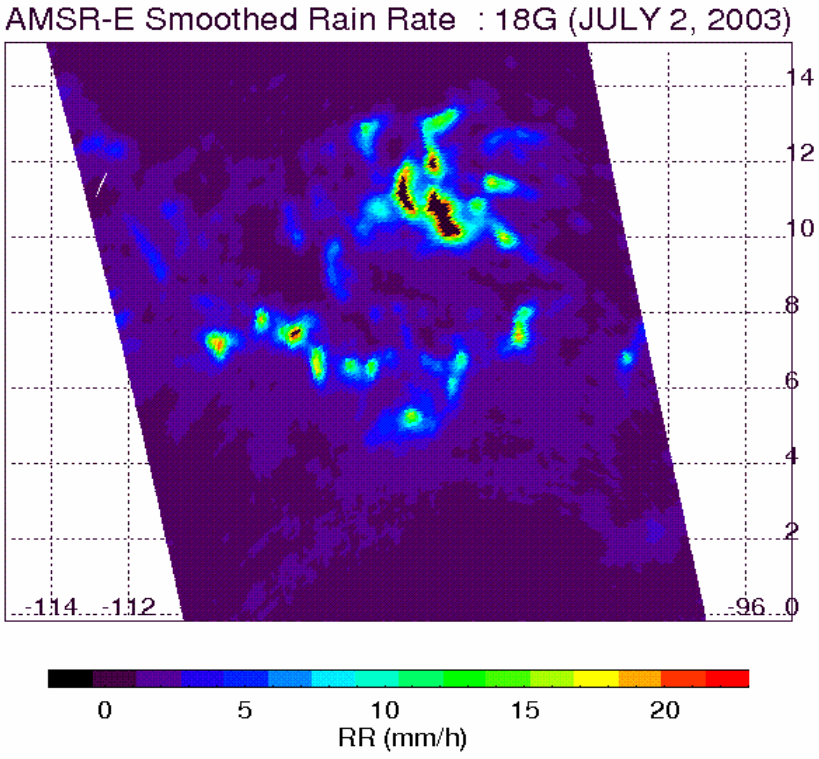

Figure 5.38 Rain rate smoothed to the 10GHz resolution over the selected area (0-15N, 95-115W) for the AMSR-E data (July 2, 2003: 20Z), a) 18GHz, b) 37GHz.

(b)

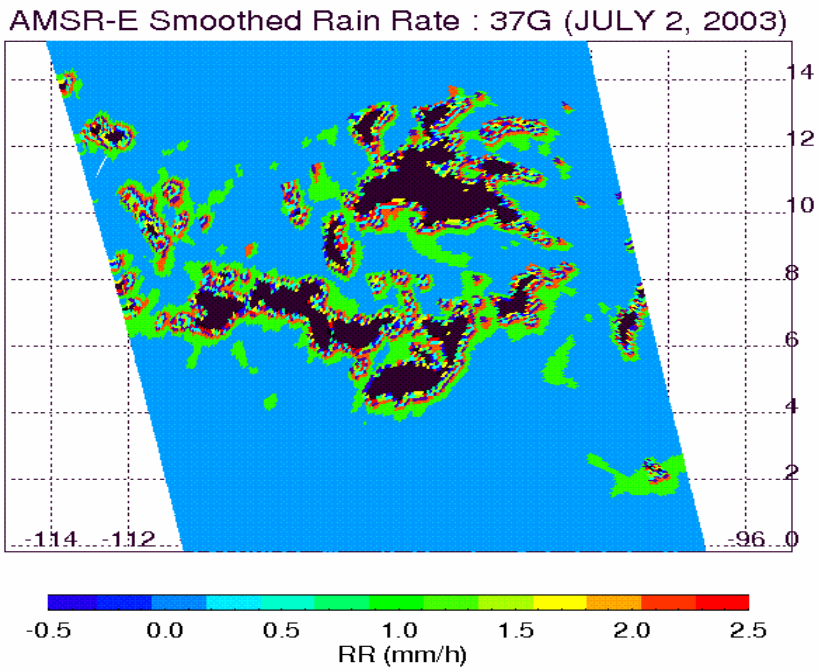

Figure 5.38, Continued.

Lastly, the weighted average rain rates from combining three frequencies are presented in Figure 5.39a. The computed rain rate uncertainties are also shown in Figure 5.39b. The locations of high uncertainty are closely linked to the high rain rate regions.

A scatter plot which relates the computed rain rates to their uncertainties was also generated in Figure 5.40. Low rain rates for which calibration uncertainty dominates mostly correspond to about 10% uncertainty and high rain rates at which the drop size distribution effect is most significant have much higher uncertainty (about 30% uncertainty).

To observe the relative weight of each frequency, the weights of the three frequencies were plotted on a pixel-by-pixel basis (Figures 5.41a-c). It is clearly shown that the 37GHz dominates over the light rain regions while the 10GHz gives significant

contributions (over 60%) in very heavy rainfall. In moderate rain (near deep convection), the contribution from the 18GHz is dominant.

To examine explicitly the relative weight contribution with respect to rain rate, the percentage weight of the each frequency as a function of rain rate was also generated. Figure 5.42 shows that the 37GHz dominates at very low rain rate and as rain rate increases, the 18GHz becomes the main contributor and then as rain rate further increases (over 5mm/h), the 10GHz's contribution becomes largest. At very high rain rates (over about 10mm/h), virtually the entire weight is primarily driven by the 10GHz.

The relative uncertainty contributions of the four sources, which are considered as primary error sources of the rainfall retrieval, were also investigated. The percentage uncertainties contributed by the each error source were shown in Figures 5.43a-c.

(a)

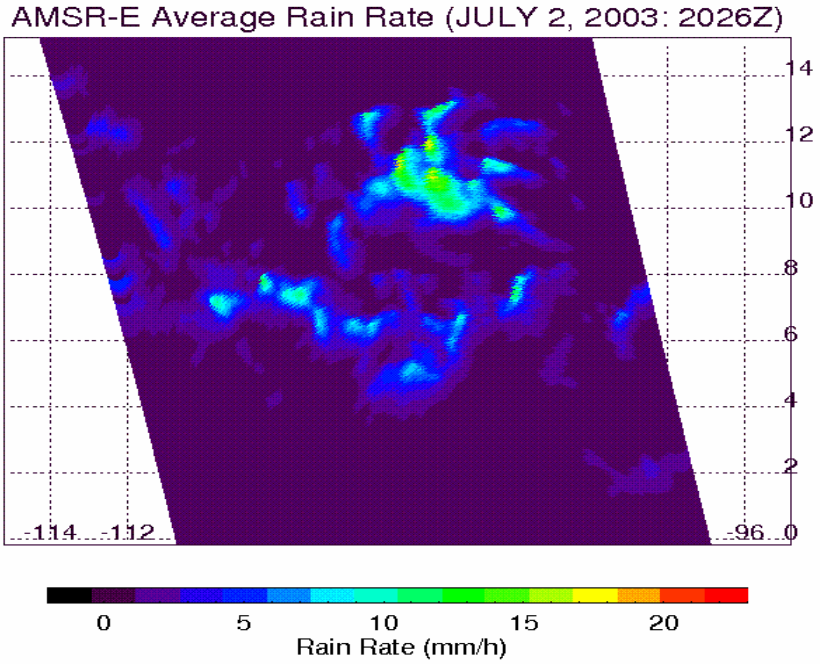

Figure 5.39 a) Weighted average rain rates, b) Rain rate uncertainties over the selected area (0-15N, 95-115W) for the AMSR-E data (July 2, 2003: 20Z).

(b)

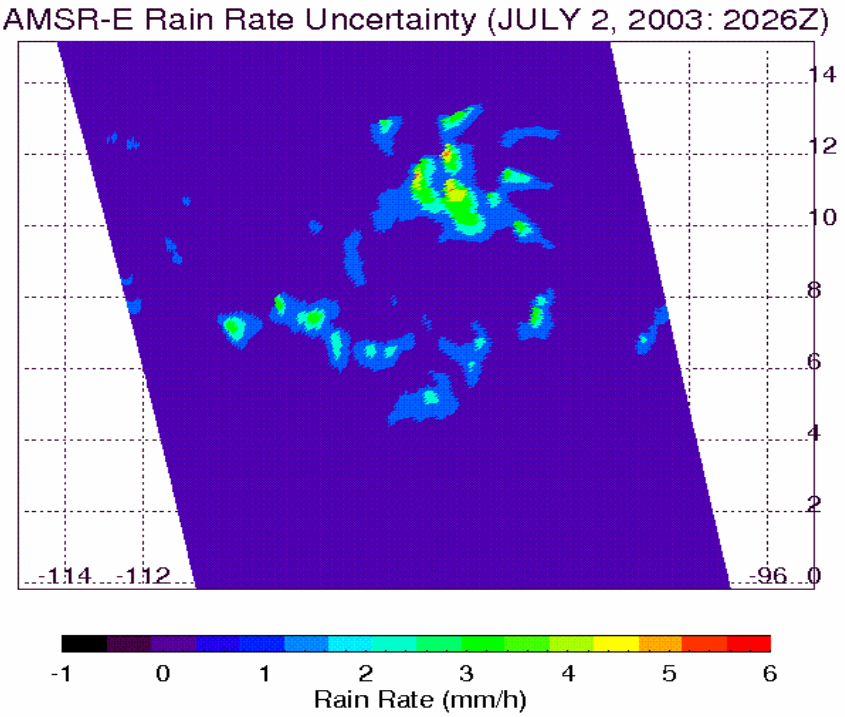

Figure 5.39, Continued.

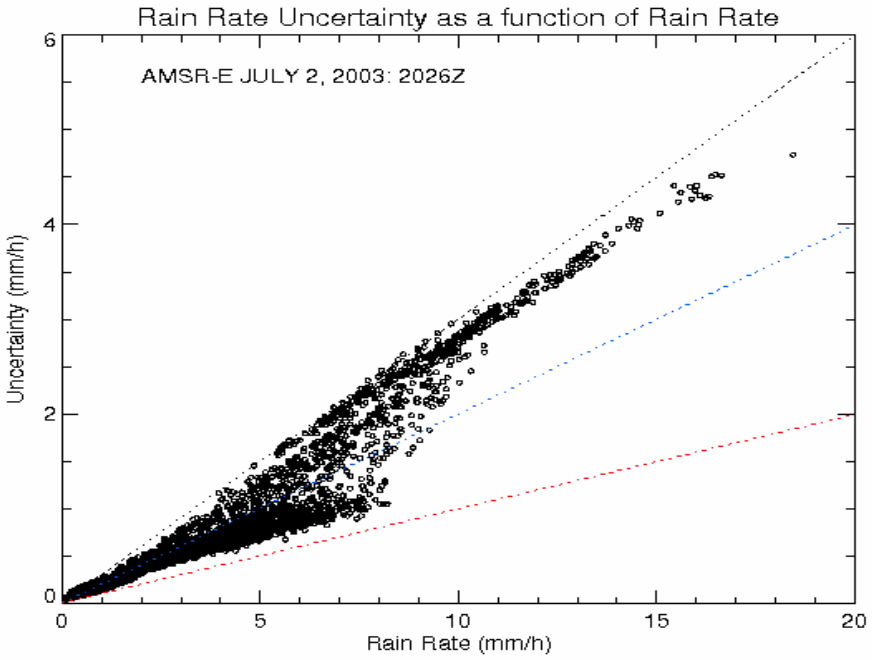

Figure 5.40 Scatter plot between the weighted average rain rates and the computed rain rate uncertainties. The 10%, 20% and 30% errors were indicated by the red, blue and black lines respectively.

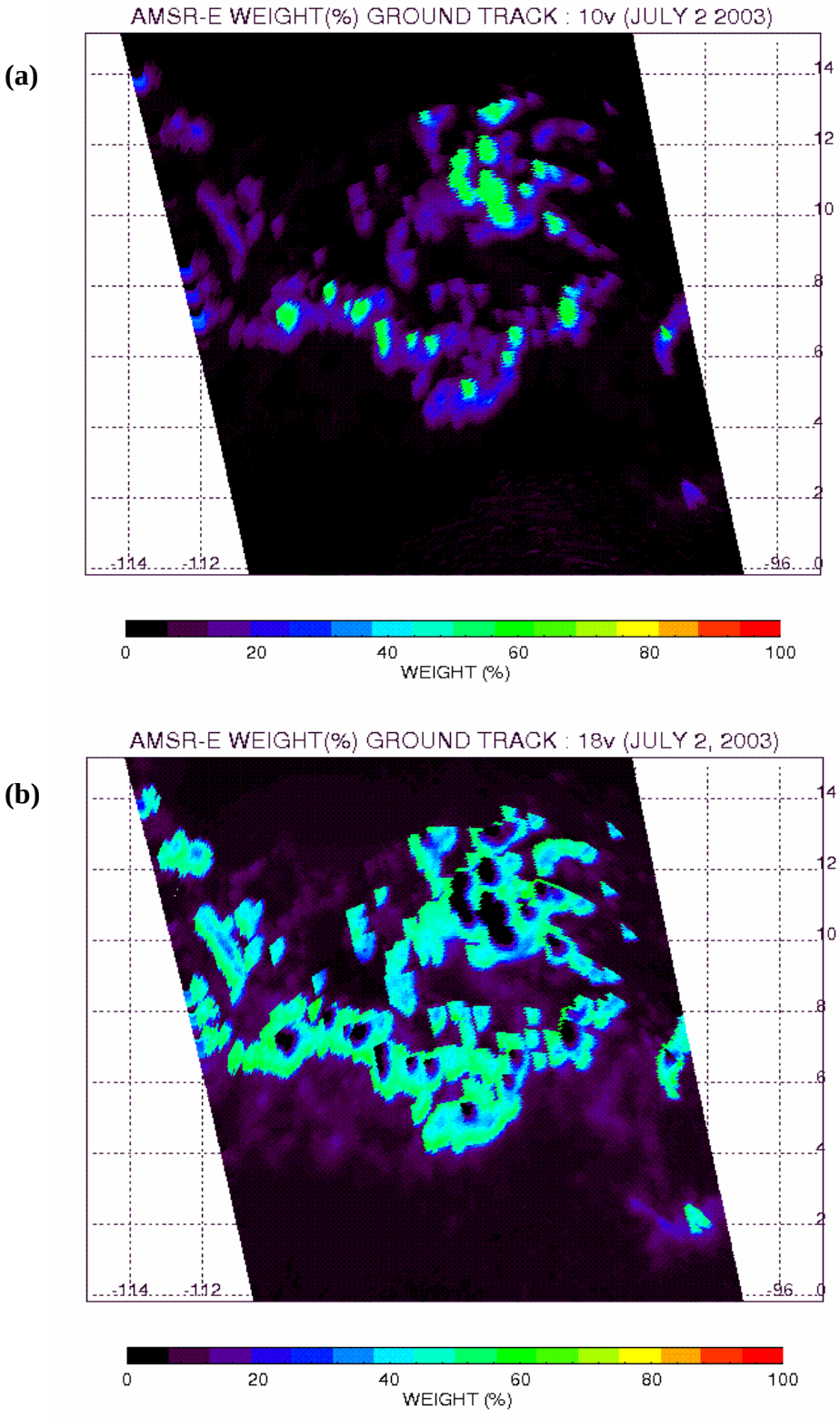

Figure 5.41 a) Weight of 10GHz frequency, b) Weight of 18GHz frequency, c) Weight of 37GHz frequency (0-15N, 95-115W, AMSR-E, July 2, 2003:20Z).

(c)

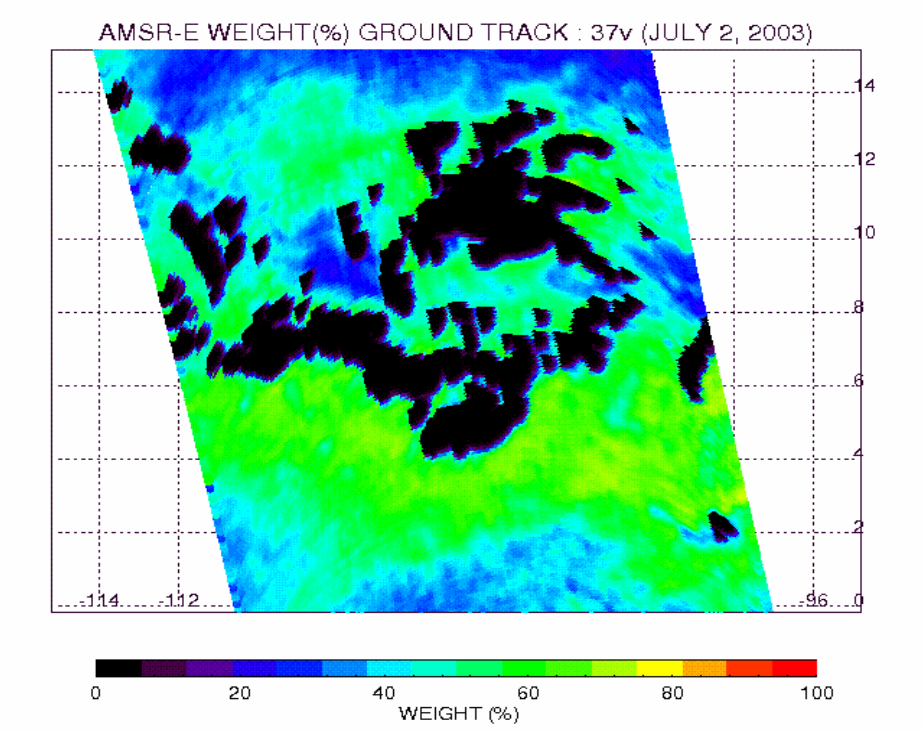

Figure 5.41, Continued.

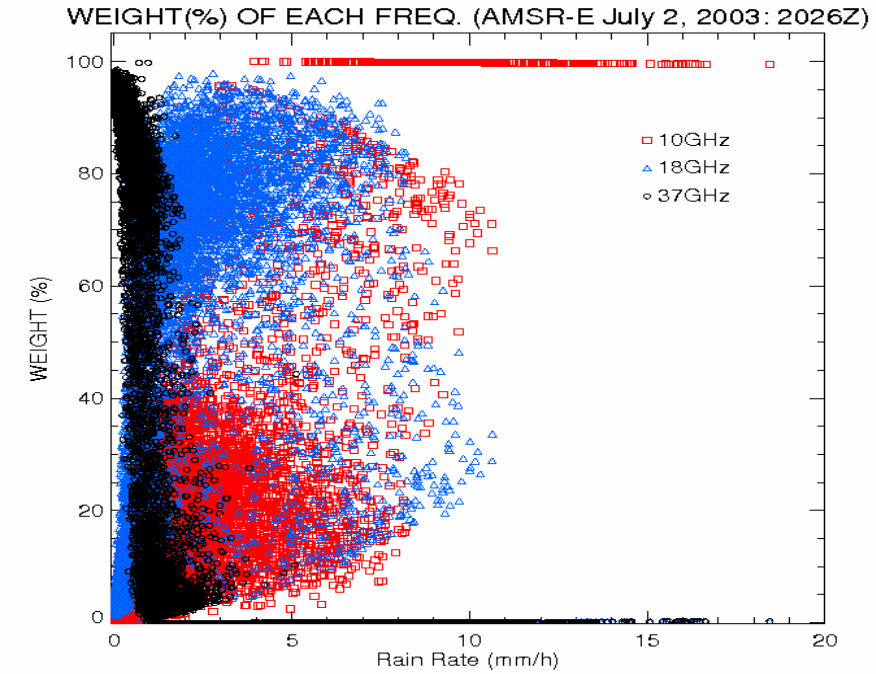

Figure 5.42 Weight of each frequency (0-15N, 95-115W, AMSR-E, July 2, 2003:20Z).

(a)

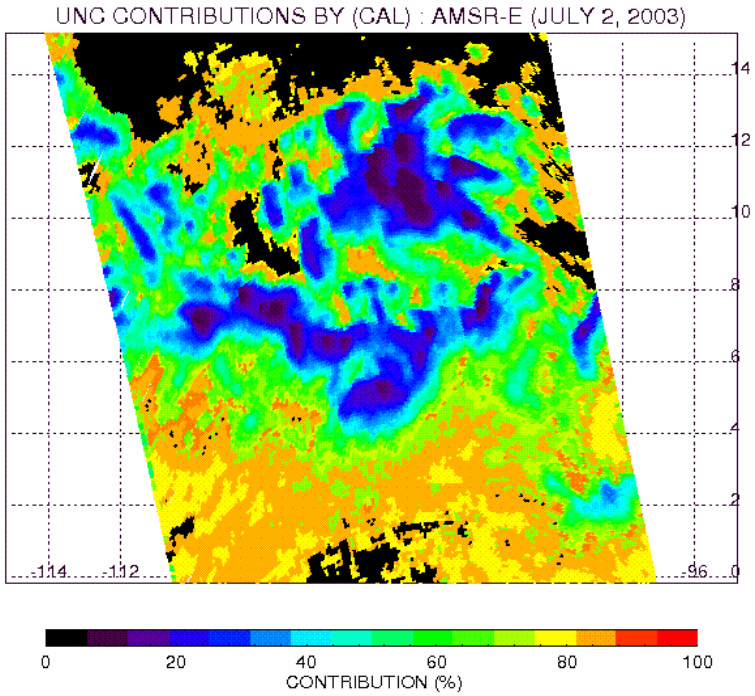

(b)

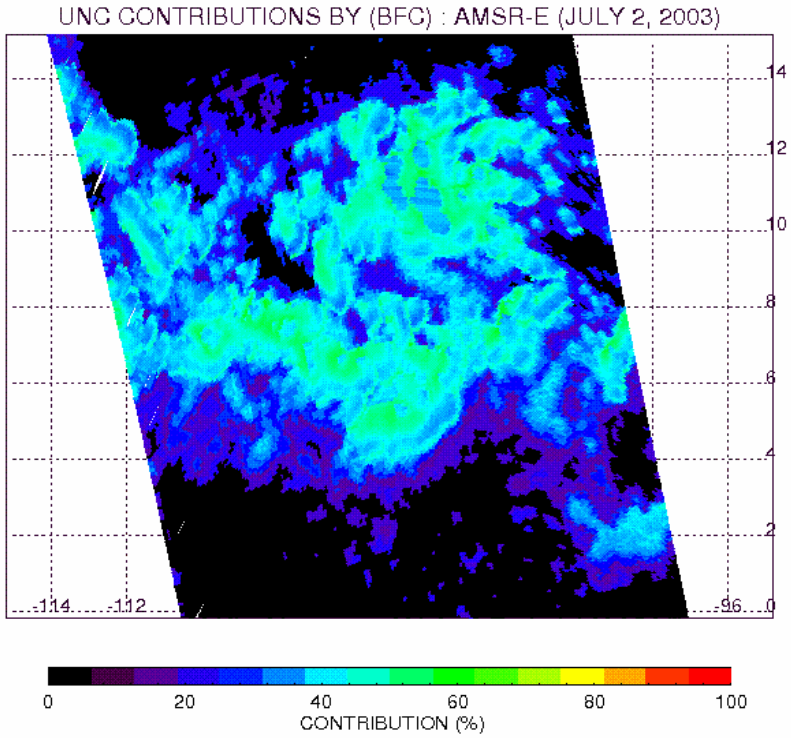

Figure 5.43 Percentage rain rate uncertainty contributed by a) CAL, b) BFC, c) DSD over the selected area (0-15N, 95-115W) of one granule data (AMSR-E, July 2, 2003:20Z).

(c)

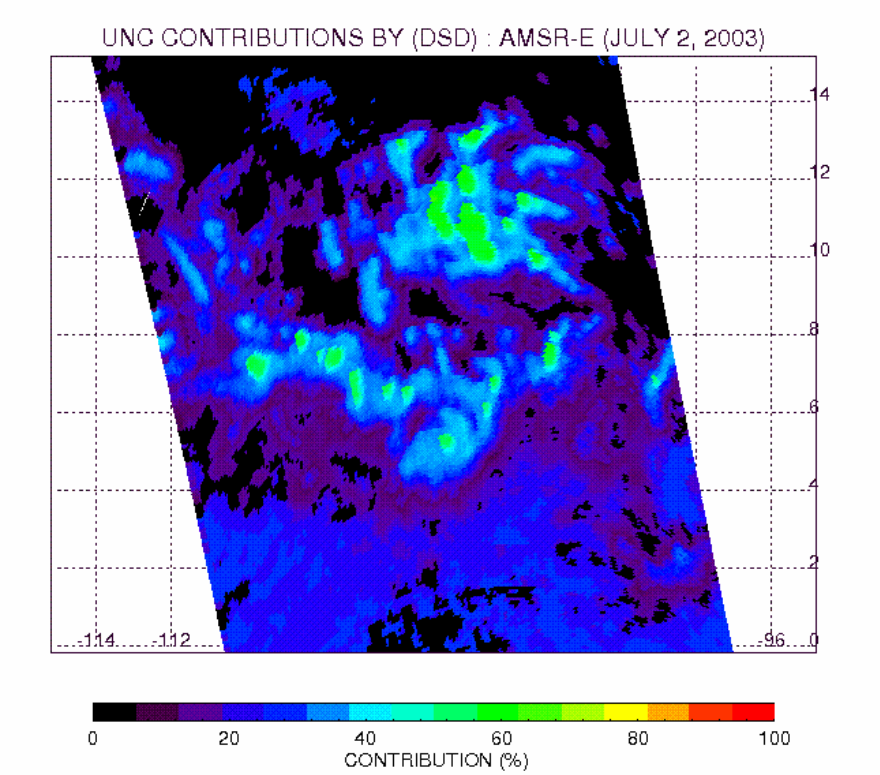

Figure 5.43, Continued.

The impact of the instrument noise is minimal among the four uncertainties sources (not shown here). The calibration uncertainty is dominant in the low rain rates and the beam filling error affects a wide range of rain rates. The contribution from the drop size distribution is the largest for high rain rates.

The percentage of uncertainty contributed by each source in terms of the rain rate was also investigated. Figure 5.44 shows that at the very low rain rates, the calibration uncertainty is largest and for the medium range of rain rates, the beam filling error and the drop size distribution uncertainty both give a major impact and for intense rainfall (over 10mm/h), the rain rate uncertainty is dominated by the drop size distribution uncertainty.

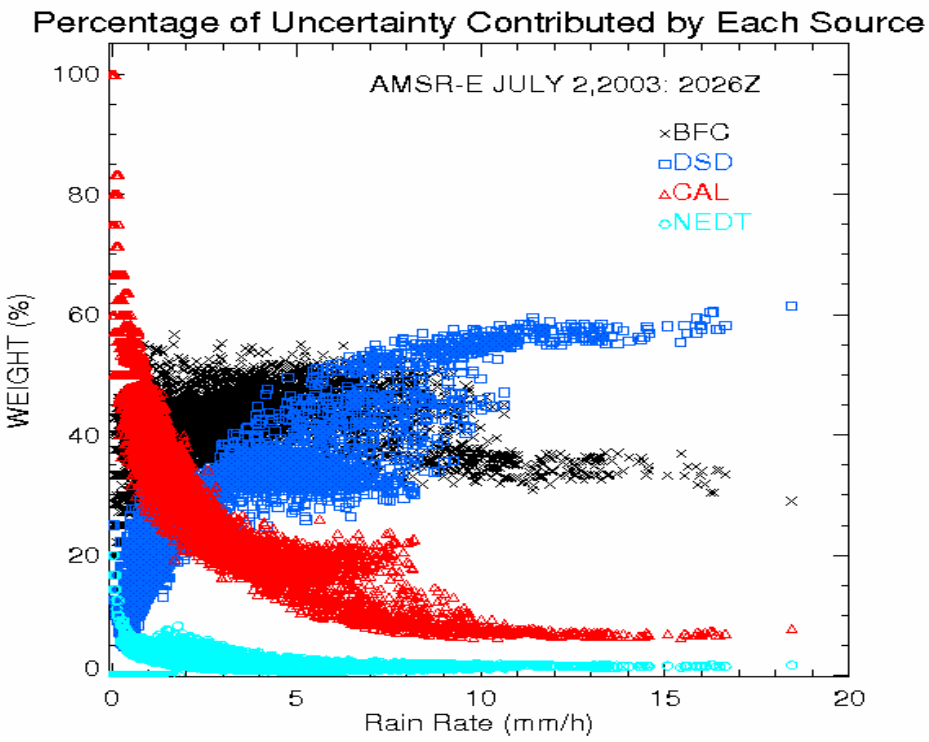

Figure 5.44 Percentage of uncertainty contributed by each source (0-15N, 95-115W, AMSR-E, July 2, 2003:20Z).

c. Monthly basis

Monthly (Level3) uncertainty in rain rate can be readily estimated by adding all of the pixel-by-pixel based net uncertainties (Level 2). For the Level 3 product, however, contribution by each uncertainty source becomes differ from the Level 2 case. For example, calibration uncertainty which dominate at very low rate is substantially diminished at near zero rain due to the offset correction. In addition, random component of each error was not taken into account in the Level 3 computation which can absorb random variability.

Computed monthly rain rate uncertainties based on 5° x5 ° grid boxes during one month period are shown in Figure 5.45 and the net uncertainty totals are presented as a function of monthly rain rate (Figure 5.46). The rain rate uncertainties correspond to about 10 to 20 percent of the monthly rain totals. In particular, higher uncertainties (about 20 percent) are mostly observed over the tropics (10N ~ 10S).

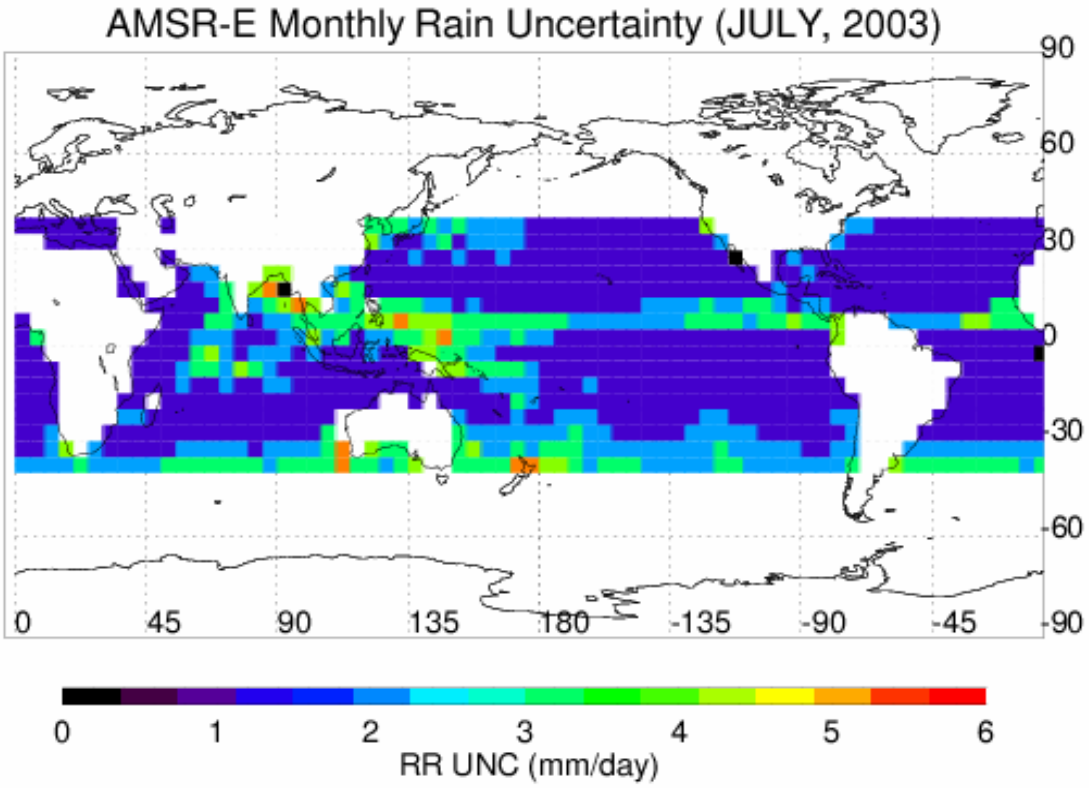

Figure 5.45 Monthly rain rate uncertainty map based on 5° x 5° grid boxes for the July 2003 AMSR-E data.

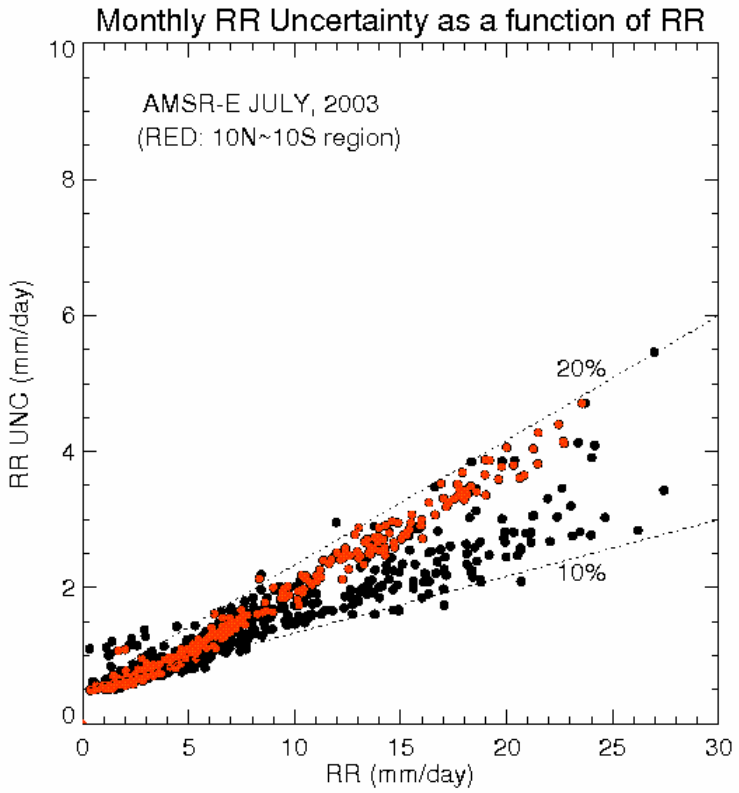

Figure 5.46 Scatter plot between the monthly rain rate uncertainties and monthly rain totals over 5x5 grid boxes for the July 2003 AMSR-E data. The 10% and 20% errors are indicated by dotted lines. Red circles denote the values over the tropics (10N ~10S).

CHAPTER VI

CONCLUSIONS

We have developed a physically-based rainfall algorithm (experimental algorithm) based on AMSR-E data that is robust with respect to the uncertainties of the rainfall retrieval. The algorithm uses six channels (37, 18.7 and 10.7GHz with dual polarizations) to maximize each channel's advantages. For example, at low rain rates, the best resolution channel, 37GHz, plays a major role to describe very light rain rates and is less sensitive to a detailed rain drop size distribution which is a primary source of rain rate uncertainties. On the other hand, the 10GHz is mainly used for heavy rain cases because of its large rain retrieval dynamic range (~up to 50mm/h). In addition, this frequency leads to lowest beam filling errors despite its larger foot print size because of the higher impact of weaker non-linearity on the R-T relationship.

In this study, we designed several improved schemes that reduce uncertainties of rainfall retrieval, resulting in more reasonable rainfall estimation. First, offset correction that adjusts biases driven by uncertainty near zero rain was developed so that it has a best resolution for the each channel, especially for the 37GHz channels to achieve very accurate offset correction. Second, for more reasonable freezing level retrieval we adjusted a radiative transfer model's thermodynamic assumption to use an average lapse rate of 5.3K/km below the freezing level while using the original assumption (6.5K/km) above the freezing level based on Ragno and Hobbs (2005). Third, we designed the weighted average retrieval scheme that merges six rain rates optimally based on the each channel's proper weighting to minimize rain rate uncertainties. To compute weight of each channel, error models that approximate quantitatively rain rate uncertainties were

used. We constructed error models using the drop size distribution uncertainty, beam filling correction error, instrumental calibration uncertainty and instrument noise as a principal error sources for rainfall retrieval.

Those uncertainties were combined to compute a net uncertainty for each of the six rain rates for each smoothed (10GHz resolution) pixel. The average rain rate for each smoothed pixel was computed by merging all rain rates based on the weight that is the inverse of the error variance of each channel. Monthly rain totals (Level 3 product) were estimated by simply adding those pixel-by-pixel basis average rain rates with a proper offset correction that were obtained by rain rate histograms over 5° x 5° grid boxes during one month period.

The results from the experimental algorithm were compared with those of the operational algorithm. Compared to the experimental algorithm, the operational algorithm overestimates the monthly freezing levels (10~30%), especially over winter hemisphere due to its inherent limitation that utilizes one representative freezing level for an entire month. On the other hand, the experimental algorithm yields more reasonable estimates by handling the variability of freezing levels effectively from its pixel-by-pixel retrieval scheme. The difference of retrieved freezing level between the two algorithms affects directly the estimates of rainfall because the rain rate is inversely related with the freezing level.

Monthly mean rain rates of the experimental algorithm are much higher than those of the operational algorithm. In particular, considerable difference was observed over winter hemisphere. Investigation of a particular granule which contains heavy rain events along with the examining cumulative rain rate histograms reveals that high

monthly rain totals over the winter hemispheres can be achieved while raining clouds' tops are relatively low in these regions. It was also found that there are some mean rain rates biases between TMI and AMSR-E data, especially over winter hemisphere. It is assumed that larger calibration uncertainty of AMSR-E is mainly responsible for these biases. But, further investigations are required.

As a by-product, embedded error models in the algorithm enable us to quantify uncertainties on the rainfall retrieval. The pixel-by-pixel basis estimates of the rain rate uncertainties associated with each rain rate were obtained and also the relative contribution of each of the error sources to the total net uncertainty for each pixel was measured.

REFERENCES

Beard, K.V., 1977: Terminal velocity adjustment for cloud and precipitation drops aloft. *J. Atmos. Sci.*, **34**, 1293-1298.

Chandrashekar, S., 1960: *Radiative Transfer*. Dover, 393pp.

Chandrasekar, V., K. Mubarak, and S. Lim, 2003: Estimation of raindrop size distribution form TRMM precipitation radar observations. *Proceedings of IGARSS 2003*, Toulouse, France, **3**, 1712-1714.

Chang, A.T.C., and L.S. Chiu, 2001: Non-systematic errors of monthly oceanic rainfall derived from passive microwave radiometry. *Geophysical Research Letters*, **28**, 1223-1226.

Chen, R., 2003: Beam filling correction study for retrieval of oceanic rain from passive microwave observations. M.S. Thesis, Texas A&M University, 49pp.

Cimini, C., E.R Westwater, S.J. Keihm, and Y. Han, 2003: Empirical evaluation of four microwave radiative forward models based on ground-based radiometer data near 20 and 30GHz. *Thirteenth ARM Science Team Meeting Proceedings,* Broomfield, CO. [Available online at http://www.arm.gov/publications/ proceedings/conf13/ extended_abs/cimini2-d.pdf]

Gunn, L. L. S., and T. U. R. East, 1954: The microwave properties of precipitation particles, *Quart. J. Roy. Meteor*. Soc., **80**, 522-544.

Huang, J., 2001: An algorithm for retrieval of monthly rainfall over the oceans from the TRMM Microwave Imager (TMI). Ph.D. Dissertation, Texas A&M University, 93pp.

Jin, K-W., 2001: Microwave radiative transfer in the mixed-phase regions of tropical rainfall. M.S. Thesis, Texas A&M University, 72pp.

Lane, J.A., and J.A. Saxton, 1952: Dielectric dispersion in pure polar liquids at very high radio frequencies. *Proc. Roy. Soc. London*, **A214**, 531-545.

Marshall, T. S., and W. McK. Palmer, 1948: The distribution of raindrops with size. *J. Meteor.,* **5**, 165-166.

Mattioli, V., E.R. Westwater, S.I. Gutman, and V.R. Morris, 2005: Forward model studies of water vapor using scanning microwave radiometers, global positioning system, and radiosondes during the Coudiness Inter-Comparison Experiment. *IEEE Transactions on Geoscience and Remote Sensing*, **43**, 1012-1021.

Mie, G.,1908: Beiträge zur optik trüber medien, speziell kolloidaler metallösungen. *Ann. Phys.*, **26**, 597-614

Rangno, A.L., and P.V. Hobbs, 2005: Microstructures and precipitation development in cumulus and small cumulonimbus clouds over the warm pool of the tropical Pacific Ocean. *Quart. J. Roy. Meteor*. Soc., **131**, 639-673.

Rosenkranz, P.W., 1993: Absorption of microwaves by atmospheric gases. *Atmospheric Remote Sensing by Microwave Radiometry*, M.A. Janssen, ed., John Wiley & Sons, Inc., 37-90.

Rosenkranz, P.W., 1998: Water vapor microwave continuum absorption: A comparison of measurements and models. *Radio Science*, **33**(4), 919-928.

Staelin, D.A., 1966: Measurements and interpretation of the microwave spectrum of the terrestrial atmosphere near 1 centimeter wavelength. *J. Geophys. Res*.,**71**, 2875-2881.

Tesmer, J.R., and T.T., Wilheit, 1998: An improved microwave radiative transfer model for tropical oceanic precipitation. *J. Atmos. Sci*., **55**, 1674-1688.

Thomas-Stahle, J.L., 2001: Remote sensing of marine atmospheric parameters using the TRMM Microwave Imager (TMI). M.S. Thesis, Texas A&M University, 52pp.

Wang, A., 1996: Modeling of the beam filling correction for microwave retrieval of oceanic rainfall. Ph.D. Dissertation, Texas A&M University, 100pp.

Wilheit, T.T., A.T.C. Chang, M.S.V. Rao, E.B. Rodgers, and J.S. Theon, 1977 : A satellite technique for quantitatively mapping rainfall rates over the oceans, *J. Applied Meteor.* **16**, 551-559.

Wilheit, T.T., A.T.C. Chang, and L.S.Chiu, 1991: Retrieval of monthly rainfall indices from microwave radiometric measurements using probability distribution functions. *J. Atmospheric and Oceanic Tech.*,**8**, 118-136.

Wilheit, T.T., C.D. Kummerow, and R. Ferraro, 2003: Rainfall algorithms for AMSR-E. *IEEE Transactions on Geoscience and Remote Sensing*, **41**, 204 -214.

APPENDIX A

OPTIMAL WEIGHTING

For simplicity only two rain rate measurements are first considered as Ra and Rb. Each measurement is assumed to have a mean true value, T, and random errors, Xi and Yi. Thus, each rain rate measurement can be expressed as

$$Ra=T + \sum Ci\cdot Xi,\ Rb=T + \sum Di\cdot Yi$$

where Ci and Di are constants. In addition, the weighted average rain rate of two is given by

$$<R> =W\cdot Ra+ (1-W)\cdot Rb$$

where W is an optimal weight. If we indicate each rain measurement's error variance as σ_a^2, $< (Ra-T)^2 >$ and σ_b^2 , $< (Rb-T)^2 >$ respectively, the error variance of weighted average, σ^2 can be written as

$$\sigma^2=W^2\cdot\sigma_a2+(1-W)^2\cdot\sigma_b^2+2W\cdot (1-W)\cdot \sigma_a\cdot \sigma_b$$

and also it can be reorganized as

$$(\sigma_a^2+\sigma_b^2-2\sigma_a\cdot \sigma_b)\cdot W^2+(2\sigma_a\cdot \sigma_b - 2\sigma_b^2)\cdot W+ \sigma_b^2$$

This equation can be minimized by differentiating with respect to W and setting the result to zero. That is,

$$2 (\sigma_a^2+\sigma_b^2-2\sigma_a\cdot \sigma_b)\cdot W=2 (\sigma_b^2-\sigma_a\cdot \sigma_b)$$

Assuming that σ_a and σ_b are independent and uncorrelated each other ($\sigma_a\cdot \sigma_b=0$), the optimal weight W is given by

$$\sigma_b^2/ (\sigma_a^2+\sigma_b^2) \text{ or } (1/ \sigma_a^2) / (1/ \sigma_a^2+ 1/ \sigma_b^2)$$

and the expected error variance, σ^2 is given by

$$1/ (1/ \sigma_a^2+ 1/ \sigma_b^2)$$

Thus, for three independent measurements (a, b and c), the expected error variance can be simply expanded as

$$1/ (1/ \sigma_a^2 + 1/ \sigma_b^2 + 1/\sigma_c^2)$$

and the optimal weight for first measurement is given by

$$(1/ \sigma_a^2) / (1/ \sigma_a^2 + 1/\sigma_b^2 + 1/\sigma_c^2)$$

Since the optimal weight is simply proportional to the inverse of error variance, individual weights can be expressed as $Wi = 1/ \sigma i^2$ and total weight is the sum of those weights, ΣWi. This computed total weight serves as a normalization factor. Therefore, the first measurement's optimal weight for three independent and uncorrelated measurements can be written simply as

$$W1/(W1 + W2 + W3)$$

where $W1=1/ \sigma_1^2$, $W2=1/ \sigma_2^2$ and $W3=1/ \sigma_3^2$ respectively.

VITA

Kyoung-Wook Jin was born in 1970 in Masan, Korea. He received a Bachelor of Science in Atmospheric Sciences from Seoul National University in 1994. He served in the military as a weather officer in Suwon Air-force Base from 1994 to 1997. He earned a Master of Science in December 2001 and a Doctor of Philosophy in December 2005, both in Atmospheric Sciences from Texas A&M University. He plans to study under a NRC postdoctoral fellowship in the Water and Carbon Cycle Group at JPL in Pasadena, California at the end of 2005.

He may be reached via email at *kwjin_atm@msn.com.* or U.S. mail, Water and Carbon Cycle Group, Jet Propulsion Laboratory, M/S 300-233, 4800 Oak Grove Drive, Pasadena, CA 91109.